



**LOW COST ANTENNA ARRAY BASED  
DRONE TRACKING DEVICE FOR  
OUTDOOR ENVIRONMENT**

**MARCOS TEIXEIRA DE OLIVEIRA**

**DISSERTAÇÃO DE MESTRADO EM SISTEMAS MECATRÔNICOS  
DEPARTAMENTO DE ENGENHARIA MECÂNICA**

**FACULDADE DE TECNOLOGIA**

**UNIVERSIDADE DE BRASÍLIA**

**UNIVERSIDADE DE BRASÍLIA  
FACULDADE DE TECNOLOGIA  
DEPARTAMENTO DE ENGENHARIA MECÂNICA**

**LOW COST ANTENNA ARRAY BASED  
DRONE TRACKING DEVICE FOR  
OUTDOOR ENVIRONMENT**

**MARCOS TEIXEIRA DE OLIVEIRA**

**Orientador: Prof. Dr.-Ing. João Paulo C. L. da Costa, PPMEC/UnB**

**Coorientador: Dr.-Ing Ricardo Kehrle Miranda, PPMEC/UnB**

**DISSERTAÇÃO DE MESTRADO EM SISTEMAS MECATRÔNICOS**

**PUBLICAÇÃO PPMEC.DM - XXX/XXXX  
BRASÍLIA-DF, 28 DE JANEIRO DE 2019.**

**UNIVERSIDADE DE BRASÍLIA  
FACULDADE DE TECNOLOGIA  
DEPARTAMENTO DE ENGENHARIA MECÂNICA**

**LOW COST ANTENNA ARRAY BASED  
DRONE TRACKING DEVICE FOR  
OUTDOOR ENVIRONMENT**

**MARCOS TEIXEIRA DE OLIVEIRA**

DISSERTAÇÃO DE Mestrado Acadêmico submetida ao Departamento de Engenharia Mecânica da Faculdade de Tecnologia da Universidade de Brasília, como parte dos requisitos necessários para a obtenção do grau de Mestre em Sistemas Mecatrônicos.

**APROVADA POR:**

Prof. Dr.-Ing. João Paulo C. L. da Costa, PPMEC/UnB  
Orientador

Prof. Dr. Sebastien Roland Marie Joseph Rondineau, PPMEC/UnB  
Examinador interno ao PPMEC

Prof. Dr. Ricardo Zelenovsky, ENE/UnB  
Examinador externo ao PPMEC

**BRASÍLIA, 28 DE JANEIRO DE 2019.**

## **FICHA CATALOGRÁFICA**

MARCOS TEIXEIRA DE OLIVEIRA

**Low cost antenna array based drone tracking device for outdoor environments**

**2019xv, 95p., 201x297 mm**

(ENM/FT/UnB, Mestre, Sistemas Mecatrônicos, 2019)

Dissertação de Mestrado - Universidade de Brasília

Faculdade de Tecnologia - Departamento de Engenharia Mecânica

## **REFERÊNCIA BIBLIOGRÁFICA**

MARCOS TEIXEIRA DE OLIVEIRA (2019) Low cost antenna array based drone tracking device for outdoor environments. Dissertação de Mestrado em Sistemas Mecatrônicos, Publicação XXX/XXXX, Departamento de Engenharia Mecânica, Universidade de Brasília, Brasília, DF, 95p.

## **CESSÃO DE DIREITOS**

AUTOR: MARCOS TEIXEIRA DE OLIVEIRA

TÍTULO: Low cost antenna array based drone tracking device for outdoor environments.

GRAU: Mestre ANO: 2019

É concedida à Universidade de Brasília permissão para reproduzir cópias desta dissertação de Mestrado e para emprestar ou vender tais cópias somente para propósitos acadêmicos e científicos. Ao autor se reserva outros direitos de publicação e nenhuma parte desta dissertação de Mestrado pode ser reproduzida sem a autorização por escrito do autor.

---

MARCOS TEIXEIRA DE OLIVEIRA

SHIGS 708 BL. E, Casa 26

# Agradecimentos

Gostaria de agradecer primeiramente à minha mãe, Gilda Valente Teixeira Oliveira e família que desde pequeno sempre me incentivou o caminho de uma boa educação e nunca mediu esforços para ajudar no que fosse preciso pra conseguir tê-la. Aos meus tios Gilvane V. T. e Silva e Ivan Silva, que sempre apoiaram e incentivaram a importância do mestrado, dando conselhos valiosos e o suporte para morar em Brasília que, sem ele, este título não seria possível. Ao meu padrinho Gilson Valente Teixeira que ao perceber um desinteresse por minha parte no meio acadêmico, sentou-se comigo colocando toda sua experiência pessoal e preocupação pedindo para que eu não desistisse.

Gostaria de agradecer também meu co-orientador de Mestrado, Dr.-Ing Ricardo Kehrlé Miranda, que desde o início dedicou seu tempo à acompanhar o desenvolvimento de toda a pesquisa me passando conceitos básicos por ser uma área nova pra mim, além dos incessantes falhos e bem sucedidos experimentos em dias de muito sol ou até mesmo chuva. Também ao meu orientador Prof. Dr.-Ing João Paulo Carvalho Lustosa da Costa que sempre com sua liderança e visão de um trabalho promissor, conseguiu me guiar em busca de uma pesquisa de excelência através da interdisciplinarização de áreas como foi o meu caso conciliando um mundo novo pra mim em Processamento de Sinais e Sistemas Embarcados. Ao Dr. Edison Pignation de Freitas da Universidade Federal do Rio Grande do Sul pela minha indicação ao grupo de pesquisa do Laboratory of Array Signal Processing (LASP) da UnB. E também não posso esquecer ainda de pessoas importantes como a Stephany Ribeiro Rodrigues, Arthur Carvalho dos Santos, Daniel Akira Ando e João Alvim que também colaboraram bastante na pesquisa de uma forma não dispensável, tanto através de troca de experiências, como em fazer os trabalhosos experimentos.

A todos, o meu muito obrigado!

# Dedicatória

Dedico este trabalho a todos engenheiros, técnicos, profissionais e/ou amadores na área de Telecomunicações. Que possam fazer bom uso e aproveitar os conhecimentos aqui compartilhados para desenvolver e aprimorar tecnologias voltadas para o bem e para a segurança pública em geral.

# Abstract

Applications of Direction of Arrival (DoA) techniques have dramatically increased in various areas ranging from the traditional wireless communication systems and rescue operations to GNSS systems and drone tracking. Particularly, police forces and security companies have drawn their attention to drone tracking devices, due to the number of accidents and incidents involving Unmanned Aerial Vehicles (UAVs). Now, new systems and devices that provide the safeness of citizens and clients, have grown and gained space on the market. In order to detect the presence of drones and to track them, there is a variety of highly expensive solutions in the market. In this way the estimation of a target's location can be obtained using off-the-shelf hardware with Direction of Arrival techniques. Consequently some actions can be taken by the responsible for the security in that place. Previous works in DoA estimation using antenna arrays have been proposed but with no practical approach.

In this dissertation, it is proposed a low cost antenna array based drone tracking device for outdoor environments. The proposed solution is divided into hardware and software parts. The hardware part of the proposed device is based on off-the-shelf components such as an omni-directional antenna array, a 4 channel Software Defined Radio (SDR) platform with carrier frequency ranging from 70 MHz to 6 GHz, a FPGA motherboard and a laptop. The software part includes algorithms for calibration, model order selection (MOS) and DoA estimation, including specific pre-processing steps to increase the DoA accuracy. The performance of our proposed low cost solution is evaluated in outdoor scenarios. According to our measurement campaigns, it is shown that, when the array is in the front fire position, i.e. with a DoA ranging from  $-60^\circ$  to  $60^\circ$ , the maximum and the average DoA errors are  $6^\circ$  and  $1,6^\circ$ , respectively.

# CONTENTS

<b>1</b>	<b>INTRODUCTION</b> .....	<b>1</b>
<b>2</b>	<b>PROBLEM FORMULATION AND DATA MODEL</b> .....	<b>6</b>
<b>3</b>	<b>LITERATURE REVIEW</b> .....	<b>8</b>
3.1	MODEL ORDER SELECTION METHODS .....	8
3.1.1	INFORMATION THEORETIC CRITERIA .....	8
3.1.2	STEIN'S UNBIASED RISK ESTIMATOR .....	10
3.1.3	RADOI .....	10
3.1.4	EXPONENTIAL FITTING TEST .....	11
3.1.5	SAMOS AND ESTER .....	12
3.2	PRE-PROCESSING OF DATA METHODS .....	13
3.2.1	SPATIAL SMOOTHING .....	13
3.2.2	FORWARD BACKWARD AVERAGING .....	13
3.2.3	VANDERMONDE INVARIANCE TRANSFORMATION .....	14
3.3	DIRECTION OF ARRIVAL METHODS .....	15
3.3.1	BEAMFORMINGS AND SUBSPACE BASED METHODS .....	15
3.3.1.1	DELAY AND SUM .....	15
3.3.1.2	CAPON .....	16
3.3.1.3	MULTIPLE SIGNAL CLASSIFICATION .....	16
3.3.1.4	ESPRIT .....	17
<b>4</b>	<b>LOW COST ANTENNA ARRAY BASED DRONE TRACKING DEVICE AND FRAME- WORK</b> .....	<b>18</b>
4.1	HARDWARE ASSEMBLING FOR THE CALIBRATION .....	19
4.2	HARDWARE ASSEMBLING FOR THE DRONE TRACKING MEASURE- MENT CAMPAIGN .....	21
4.3	SIGNAL PROCESSING FRAMEWORK STRUCTURE .....	21
4.3.1	PHASE DEVIATION CORRECTION .....	22
4.3.2	BAND-REJECTION FILTER .....	23
4.3.3	SELECTION OF SAMPLES AND MATRIX $\mathbf{X}$ .....	23
4.3.4	MOS, PRE-PROCESSING AND DOA ESTIMATION .....	25



<b>5</b>	<b>RESULTS</b> .....	<b>28</b>
5.1	EXPERIMENTAL SETUP.....	28
5.2	BAND-REJECT FILTER RESULTS.....	30
5.3	MOS RESULTS.....	31
5.4	DOA RESULTS.....	34
<b>6</b>	<b>CONCLUSION</b> .....	<b>39</b>
	<b>BIBLIOGRAPHY</b> .....	<b>41</b>
	<b>APPENDIX A PROPOSED EXTRAPOLATION ALGORITHM TO FIND THE EFT THRESHOLDS FOR EXTREMELY LOW PROBABILITY OF FALSE ALARM</b> .....	<b>50</b>
	<b>ATTACHMENT</b> .....	<b>53</b>
<b>A</b>	<b>PIXHAWK CONTROLLER SETUP</b> .....	<b>54</b>
A.1	ACCELEROMETER CALIBRATION.....	55
A.2	COMPASS CALIBRATION.....	56
A.3	BATTERY MONITOR.....	56
A.4	SONAR.....	56
A.5	RADIO CALIBRATION.....	57
A.6	FLY MODES.....	58
A.7	FAILSAFE.....	61
A.8	GEOFENCE SETTINGS.....	61
A.9	POSSIBLE ERRORS.....	61
	<b>REFERENCES</b> .....	<b>64</b>

# Resumo<sup>1</sup>

Aplicações para técnicas de Direção de Chegada (DoA) têm crescido drasticamente em várias áreas, desde os tradicionais sistemas de comunicação sem fio e operações de resgate até os sistemas GNSS e rastreamento de drones. Particularmente, as forças policiais e as empresas de segurança têm voltado sua atenção para os dispositivos de rastreamento de drones, devido ao número de acidentes e incidentes envolvendo estes Veículos Aéreos não Tripulados (VANTs). Agora, novos sistemas e dispositivos que fornecem segurança a cidadãos e clientes cresceram e ganharam espaço no mercado. Para detectar a presença de drones e rastreá-los existe uma variedade de soluções altamente caras no mercado. Porém, a estimativa da localização de um alvo pode ser obtida usando hardware barato, comprado facilmente no mercado, e com técnicas de Direção de Chegada. Data esta estimativa, algumas ações podem ser tomadas pelo responsável pela segurança no local. Trabalhos anteriores na estimativa de direção de chegada usando arranjo de antenas foram propostos, mas sem uma abordagem prática.

Nesta dissertação, propõe-se um dispositivo de rastreamento de drones baseado em arranjo de antenas de baixo custo para ambientes externos. A solução proposta é dividida em partes de hardware e software. A parte de hardware do dispositivo proposto é baseada em componentes fáceis de serem encontrados no mercado, como um arranjo de antena omnidirecional, uma plataforma SDR (Rádio Definido por Software) de 4 canais com frequência de portadora variando de 70 MHz a 6 GHz, uma placa-mãe FPGA e um laptop. A parte do software inclui algoritmos para calibração, seleção de ordem de modelo (MOS) e estimativa de DoA, incluindo etapas específicas de pré-processamento para aumentar a precisão dos cálculos para os métodos de DoA. Avaliamos o desempenho de nossa solução de baixo custo, proposta para ambientes externos, e de acordo com as medições de campo, mostra-se que, quando o transmissor está na posição frontal, ou seja, com um DoA variando de  $-60^\circ$  a  $60^\circ$ , o máximo e a média dos erros de DoA são  $6^\circ$  e  $1,6^\circ$ , respectivamente.

---

<sup>1</sup>EN: This abstract is intended to translate the dissertation into Portuguese language BR, as well as present a translated and summarized version of the contents of this document. In this chapter, we present a summary translation of the data model used, the state-of-the-art review, the proposed method and the results obtained with the experiments.

PT: Este capítulo visa criar um resumo estendido desta dissertação, bem como, apresentar o conteúdo deste documento em português BR. Apresenta-se uma versão traduzida e resumida do modelo de dados utilizado, da revisão do estado-da-arte, do método proposto e dos resultados obtidos com a realização dos experimentos.

## Formulação do problema e modelo de dados

Supõe-se  $d$  fontes de sinais de banda estreita e suficientemente distantes. Esses sinais possuem frente de onda planar e atingem um arranjo de antenas de recepção com  $M$  sensores omnidirecionais uniformemente e linearmente dispostos.

O espaço  $\Delta$  entre duas antenas adjacentes é igual a  $\frac{\lambda}{2}$ , onde  $\lambda$  é o comprimento de onda do sinal da portadora. Os sinais recebidos no arranjo de antenas podem ser escritos da seguinte maneira

$$\mathbf{X} = \mathbf{A}\mathbf{S} + \mathbf{N} \in \mathbb{C}^{M \times N}, \quad (1)$$

onde  $\mathbf{A} \in \mathbb{C}^{M \times d}$  é a matriz de direção e seu  $i$ -ésimo vetor de direção é dado por

$$\mathbf{a}(\mu_i) = \left[ 1 \quad e^{j\mu_i} \quad e^{2j\mu_i} \quad \dots \quad e^{j(M-1)\mu_i} \right]^T \in \mathbb{C}^{M \times 1}, \quad (2)$$

onde  $\mu_i$  é a frequência espacial que pode ser mapeada na direção da chegada  $\theta_i$  da  $i$ -ésima fonte, de acordo com a seguinte expressão:  $\mu_i = \frac{2\pi\Delta \sin \theta_i}{\lambda}$ .  $\mathbf{S} \in \mathbb{C}^{d \times N}$  é a matriz de símbolos com  $N$  sendo o número de amostras.  $\mathbf{N} \in \mathbb{C}^{M \times N}$  representa a matriz de ruído, cujos elementos são supostos como Gaussianos Complexos Circularmente Simétricos, idênticamente e independentemente distribuídos (i.i.d.).

Dado (1) e assumindo que o ruído e o sinal não estão correlacionados, a matriz de covariância pode ser calculada como

$$\mathbf{R}_{\mathbf{X}\mathbf{X}} = E\{\mathbf{X}\mathbf{X}^H\} = \mathbf{A}\mathbf{R}_{\mathbf{S}\mathbf{S}}\mathbf{A}^H + \mathbf{R}_{\mathbf{N}\mathbf{N}}, \quad (3)$$

onde  $(\cdot)^H$  é o operador Hermitiano  $E\{\cdot\}$  é o operador do valor esperado. Na prática, a matriz de covariância da amostra é calculada da seguinte forma

$$\hat{\mathbf{R}}_{\mathbf{X}\mathbf{X}} = \frac{\mathbf{X}\mathbf{X}^H}{N} \in \mathbb{C}^{M \times M}. \quad (4)$$

As técnicas de DoA usadas ao longo deste documento exploram a matriz de covariância de amostra em (4). A matriz  $\mathbf{X}$  é pré-processada antes de se calcular a matriz de covariância de amostra  $\hat{\mathbf{R}}_{\mathbf{X}\mathbf{X}}$ .

O objetivo do nosso dispositivo de rastreamento de drones é estimar a componente Direção de Chegada (DoA)  $\theta_1$  do sinal em linha de visão direta (LoS) de um drone em um ambiente externo. Supõe-se que não há obstrução na componente LoS. Portanto, presume-se que a componente LoS tenha a maior potência em comparação com os componentes não LoS. Matematicamente, pode-se expressá-la como

$$\|\mathbf{a}(\mu_1)\mathbf{s}(\mu_1)\|_F > \|\mathbf{a}(\mu_i)\mathbf{s}(\mu_i)\|_F, \quad (5)$$

para  $i = 2, \dots, d$ . O operador  $\|\cdot\|_F$  representa a norma Frobenius e  $d$  é a ordem do modelo,

ou seja,  $d$  significa o número de fontes ou VANTs presentes no espaço escaneado.

## **Estado da arte para métodos de estimação de MOS, pré-processamento e DoA**

Nesta Seção são apresentados todos os métodos utilizados para construir o dispositivo proposto para rastreamento de drones baseado em arranjo de antenas de baixo custo para ambientes externos. Os métodos de Seleção de Ordem Modelo (MOS) são importantes para definir o número de Veículos Aéreos Não Tripulados (VANTs) presentes no espaço aéreo escaneado, e é um pré requisito para alguns algoritmos de DoA. Em seguida, para aprimorar a precisão dos métodos DoA, os algoritmos de pré-processamento são apresentados. Por fim, os métodos mais comuns no estado da arte para cálculo da DoA são revisados.

### **Métodos de seleção da ordem do modelo**

Um dos pré-requisitos para a operação adequada do dispositivo proposto é uma boa seleção de amostras de dados do sinal obtido para serem processados. Uma das maneiras de realizar essa seleção é calcular a DoA apenas se estiver na presença de um sinal. Em outras palavras, deve-se calcular a DoA apenas se existir um VANT no espaço escaneado. Além disso, vários algoritmos de estimativa DoA dependem do conhecimento prévio da ordem do modelo. Na Tabela 1 as equações dos métodos usados são resumidamente descritos.

Tabela 1: Métodos MOS utilizados

AIC [1]	$\text{AIC}(P) = -\log \left\{ \frac{\prod_{i=P+1}^M \lambda_i^{\frac{1}{M-P}}}{\frac{1}{M-P} \sum_{i=P+1}^M \lambda_i} \right\}^{(M-P)N} + p(M, N) \quad (6)$
MDL [2]	$\text{EDC}(P) = -\log \left\{ \frac{\prod_{i=P+1}^M \lambda_i^{\frac{1}{M-P}}}{\frac{1}{M-P} \sum_{i=P+1}^M \lambda_i} \right\}^{(M-P)N} + p(M, N) \sqrt{N \log(\log(N))} \quad (7)$
EDC [3]	$\text{MDL}(P) = -\log \left\{ \frac{\prod_{i=P+1}^M \lambda_i^{\frac{1}{M-P}}}{\frac{1}{M-P} \sum_{i=P+1}^M \lambda_i} \right\}^{(M-P)N} + \frac{1}{2} p(M, N) \log N \quad (8)$
SURE [4]	$\hat{R}(P) = (M - P) \hat{\sigma}_P^2 + 2\sigma^2 P + (\hat{\sigma}_P^4 - 2\hat{\sigma}_P^2 \sigma^2 \frac{4\hat{\sigma}_P^2 \sigma^2}{N}) \sum_{i=1}^P \frac{1}{\lambda_i} + C$ $C = \frac{4\sigma^2}{N} \sum_{i=1}^P \sum_{j=P+1}^M \frac{\lambda_i - \hat{\sigma}_P^2}{\lambda_i - \lambda_j} + \frac{2\sigma^2}{N} P(P - 1) - \frac{2\sigma^2}{N} (M - 1) \sum_{i=1}^P \left( 1 - \frac{\hat{\sigma}_P^2}{\lambda_i} \right) \quad (9)$
	$g_1(P) = \frac{\lambda_{P+1}}{\sum_{i=2}^M \lambda_i}, \quad g_2(P) = \frac{\xi_P}{\sum_{i=1}^{M-1} \xi_i}, \quad P = 1, \dots, M - 1 \quad (10)$
RADOI [5]	$\xi_P = 1 - \frac{\alpha(\lambda_P - \mu_P)}{\mu_P}, \quad \mu_P = \frac{1}{M - P} \sum_{i=P+1}^M \lambda_i, \quad \alpha = \left[ \frac{\lambda_P - \mu_P}{\mu_P} \right]^{-1} \quad (11)$
	$\text{RADOI}(P) = g_1(P) - g_2(P) \quad (12)$
	$\hat{\lambda}_{M-P} = (P + 1) \cdot \left( \frac{1 - a(P + 1, N)}{1 - a(P + 1, N)^{P+1}} \right) \cdot \frac{1}{P + 1} \sum_{i=0}^N \lambda_{M-i} \quad (13)$
EFT [6]	$a(M, N) = \sqrt{\frac{1}{2} \left( \frac{15}{M^2 + 2} - \sqrt{\frac{225}{(M^2 + 2)^2} - \frac{180M}{N(M^2 - 1)(M^2 + 2)}} \right)} \quad (14)$
ESTER [7]	$\mathbf{E}_E(P) = \mathbf{W}(P)_\uparrow - \mathbf{W}(P)_\downarrow \Phi(P),$ $\Phi(P) = (\mathbf{W}(P)_\downarrow)^\dagger (\mathbf{W}(P)_\uparrow), \quad (15)$
	$\mathbf{U}(P) = [\mathbf{W}(P)_\uparrow   \mathbf{W}(P)_\downarrow] \in (M - 1) \times 2P \quad (16)$
SAMOS [8]	$E_S(P) = \frac{1}{P} \sum_{i=P+1}^{2P} \lambda_i^{tb} \quad (17)$

Em (6), (7) e (8)  $M$  denota o número de sensores,  $N$  é o número de amostras e  $\lambda_i$  é o  $i$ -ésimo autovalor de  $\hat{\mathbf{R}}_{\mathbf{X}\mathbf{X}}$ . Note que a única coisa que muda entre estes 3 métodos é a parte que acompanha função de penalidade  $p(M, N)$ . Já em (9) tem-se  $\hat{\sigma}_P^2$  sendo a variância de ruído e esta variância é estimada via Random Matrix Theory (RMT) definido em [4]. Enquanto que em RADOI [5], as funções  $g_1(P)$  e  $g_2(P)$  em (10) são definidas empiricamente e  $\lambda$  contém os autovalores da matriz de correlação. Passando para EFT [6],  $\hat{\lambda}_{M-P}$  em (13) é a predição do próximo autovalor de ruído. Em (15) e (16),  $\mathbf{W}(P)_\uparrow$  contém os  $P$  primeiros autovetores esquerdos em colunas,  $\mathbf{W}(P)_\downarrow$  contém os últimos  $P$  autovetores direitos como colunas,  $\{\cdot\}^\dagger$  denota o operador de pseudo-inversa e  $\lambda_i^{tb}$  contém os autovalores de  $\mathbf{U}(P)$ . Em todos,  $P$  denota o número candidato a ordem do modelo estimada.

## Métodos de pré-processamento de dados

Neste trabalho, os métodos de pré-processamento são aplicados à matriz  $\mathbf{X}$  transformando-a em uma matriz  $\mathbf{Z}$  que será usada pelos outros algoritmos desejados. Desta forma consegue-se uma precisão maior nos resultados dos métodos usados posteriormente, no nosso caso os métodos para estimação da DoA. A Tabela 2 expressa as equações utilizadas pelos métodos descritos.

Tabela 2: Métodos de pré-processamento de dados

SPS [9]	$\mathbf{J}_l^{(M)} = [\mathbf{0}_{M_{\text{sub}} \times (l-1)} \mathbf{I}_{M_{\text{sub}}} \mathbf{0}_{M_{\text{sub}} \times (L-l)}], \quad l \in 1 \leq l \leq L, \quad (18)$
	$\mathbf{X}_{SS} = [\mathbf{J}_1^{(M)} \mathbf{X} \quad \mathbf{J}_2^{(M)} \mathbf{X} \quad \dots \quad \mathbf{J}_L^{(M)} \mathbf{X}] \in \mathbb{C}^{M_{\text{sub}} \times LN}, \quad (19)$
FBA [10, 11]	$\mathbf{X}_{FB} = \frac{1}{\sqrt{2}} [\mathbf{X}, \mathbf{J}_1 \mathbf{X}^* \mathbf{J}_2], \quad (20)$
VIT [12]	$\check{\mathbf{v}}(\theta) = \mathbf{T}_{\text{vit}}(\mathbf{r}) \mathbf{v}(\theta) = \left( \frac{e^{j\mu(\theta)} - r}{1 - r} \right)^{M-1} \cdot \begin{pmatrix} 1 \\ e^{j\nu(\theta)} \\ \vdots \\ e^{(M-1)\nu(\theta)} \end{pmatrix} \quad (21)$
	$\nu = \arctan \left( \frac{2K \cdot \sin(\theta)}{1 - K^2 + (1 + K^2) \cdot \cos(\theta)} \right), \quad (22)$
	$\mathbf{T}_f(K, \theta) = \mathbf{T}_{\text{vit}}(\mathbf{r}) \mathbf{F}(\theta). \quad (23)$
	$\mathbf{Y} = \mathbf{T}_f(r, \theta) \mathbf{X} \in \mathbb{C}^{M \times N}. \quad (24)$

Na Tabela 2, as matrizes  $\mathbf{J}$  em (18), (19) e (20) são matrizes de seleção,  $M_{\text{sub}}$  é o número de sensores do sub-arranjo,  $M$  o número de sensores do arranjo original e  $L$  denota o número de sub-arranjos. Em (21) e (23),  $\mathbf{T}_{\text{vit}}(r) \in \mathbb{C}^{M \times M}$  é a matriz definida em [12],  $\mathbf{v}(\theta)$  contém a estrutura Vandermonde e  $\nu$  é a nova fase mapeada da fase original  $\mu$ . Em (23),  $\mathbf{F}(\theta) = \text{diag}\{\mathbf{v}(\theta)\}$  é uma matriz diagonal de foco, contendo a estrutura Vandermonde mapeada. Finalmente em (24),  $\mathbf{Y}$  é a matriz de sinal recebida já transformada, pela matriz de transformação  $\mathbf{T}_f(K, \theta)$ , e pronta para ser processada.

### Métodos de estimação da Ordem de Chegada

Por fim, a direção de chegada de um sinal é utilizada neste trabalho para a estimativa da localização e rastreamento de um VANT e alguma ação pode ser tomada pelo responsável local. Há uma variedade de algoritmos e suas derivações, no entanto, este trabalho se concentra nos métodos clássicos mais conhecidos de cálculo de DoA, apresentados na Tabela 3.

Tabela 3: Métodos de estimação DoA selecionados no Estado da Arte

Delay And Sum [13]	$P_{\text{DS}}(\theta) = \frac{\mathbf{w}(\theta)^{\text{H}} \mathbf{R}_{\text{xx}} \mathbf{w}(\theta)}{\mathbf{w}(\theta)^{\text{H}} \mathbf{w}(\theta)}. \quad (25)$
Capon [14]	$P_{\text{CAP}}(\theta) = \frac{1}{\mathbf{w}(\theta)^{\text{H}} \mathbf{R}_{\text{xx}}^{-1} \mathbf{w}(\theta)}. \quad (26)$
MUSIC [15]	$P_{\text{MUSIC}}(\theta) = \frac{1}{\mathbf{w}^{\text{H}}(\theta) \mathbf{V}_{\text{n}} \mathbf{V}_{\text{n}}^{\text{H}} \mathbf{w}(\theta)}, \quad (27)$
	$\mathbf{\Psi} = \mathbf{J}_1 \mathbf{U}_s^+ \mathbf{J}_2 \mathbf{U}_s \quad (28)$
ESPRIT [16]	$\mathbf{\Psi} \stackrel{\text{EVD}}{=} \mathbf{E} \mathbf{\Phi} \mathbf{E}^{\text{H}}, \text{ with } \mathbf{\Phi} = \text{diag}[\phi_1, \dots, \phi_d] \quad (29)$
	$\mu_i = \angle(\phi_i), i = 1, \dots, d \quad (30)$

Na Tabela 3, o vetor  $\mathbf{w}(\theta)$  em (25), (26) e (27) varia de acordo com os valores candidatos de  $\theta$ . O valor de  $\theta$  que maximiza a expressão em (25), (26) e (27) é o  $\hat{\theta}_1$ , sendo que o modelo de dados supõe uma componente LoS, ou seja, que não existem obstáculos entre o transmissor e receptor. Portanto, o componente correspondente à maior potência deve ser o mesmo componente com DoA  $\hat{\theta}_1$ .  $\mathbf{U}_s \in \mathbb{C}^{M \times d}$  é subespaço de sinal, que é igual aos  $d$  autovetores correspondentes aos  $d$  maiores autovalores, enquanto que  $\mathbf{V}_{\text{n}} \in \mathbb{C}^{M \times M-d}$  é o

subespaço ruído, que é igual aos  $M - d$  autovetores correspondentes aos  $M - d$  autovalores com menor potência. Em (29) and (30),  $\Phi$  é a matriz diagonal que contém os autovalores de  $\Psi$ . Todas as frequências espaciais são calculadas e a frequência espacial cujo componente tem maior potência é o  $\hat{\mu}_1$  que pode ser mapeado para  $\hat{\theta}_1$ .

## Dispositivo proposto

Nesta seção é detalhado o dispositivo de rastreamento de drone baseado em arranjo de antenas de baixo custo, descrevendo as etapas para a calibração de hardware, colocando todos os quatro canais do SDR em fase e permitindo a estimativa DoA. Posteriormente, é apresentada a montagem dos componentes de hardware para o dispositivo. Por fim, um framework do algoritmo de processamento de sinais para estimativa de DoA é proposto.

### Montagem do hardware para calibração

Um dos principais problemas em arranjo de antenas é o desequilíbrio de fase entre as entradas do SDR. Esse problema pode ser causado por imperfeições de hardware, como diferentes comprimentos de cabos e trilhas, multipercurso, diferentes instantes de partida nos osciladores ou até mesmo por simples imperfeições na fabricação. O fornecedor de hardware disponibiliza um software [17] para sincronização do clock do oscilador local. No entanto, este software não executa a calibração de fase. Este problema pode ser resolvido por um filtro que multiplica o sinal recebido por um exponencial contendo o erro de fase. Este erro de fase é obtido medindo a diferença de fase entre as entradas do SDR, através de um sinal recebido que foi gerado em uma saída TX do SDR. Este sinal passa por um divisor de potência com quatro canais de saída de mesma potência e chega em fase a todas as entradas do SDR.

### Montagem do hardware para as medições de campo

Após o hardware ter sido calibrado, o próximo passo é montá-lo para realizar as medições. O arranjo de antenas omnidirecionais contém quatro sensores e é conectado ao hardware calibrado composto pela placa-mãe FPGA e pela placa-filha SDR. Cada antena é dual band (de 2400 MHz a 2483,5 MHz e de 4900 MHz a 5875 MHz) [18] e possui polarização linear com ganho de 3,7 dBi. O espaço  $\Delta$  entre duas antenas consecutivas é igual a 59,9 mm, que dá meio comprimento de onda para a frequência utilizada como portadora.



## Estrutura do algoritmo proposto

### Correção do desvio de fase

Como citado anteriormente, vários problemas podem causar desequilíbrio de fase. Aqui é apresentada a abordagem matemática para determinar o vetor de compensação de tal forma que ele corrija o deslocamento de fase.

Primeiro, a fase dos elementos da matriz  $\mathbf{X}$  é extraída, da seguinte forma

$$\phi_{i,j} = \angle x(i,j) = \arctan \left( \frac{\text{Im}\{x(i,j)\}}{\text{Re}\{x(i,j)\}} \right), \quad (31)$$

onde  $x(i,j)$  é o elemento na posição  $i,j$  da matriz medida  $\mathbf{X}$ . Os operadores  $\angle$ ,  $\text{Im}\{\cdot\}$  e  $\text{Re}\{\cdot\}$  representam o operador de fase, a parte imaginária de um número complexo e a parte real de um número complexo, respectivamente.

Para calcular a diferença de fase entre dois canais, a seguinte expressão é aplicada

$$\omega(m, :) = \Phi(m, :) - \Phi(i, :) \in \mathbb{C}^{1 \times N}, \quad (32)$$

onde  $\Phi$  representa a matriz com as fases dadas por (31),  $i$  indica o canal de referência e  $m$  varia de 1 a  $M$ . Dado que o vetor  $\omega(m, :)$  é a  $m$ -ésima linha da matriz  $\Omega$ , no caso  $m = i$ , a  $i$ -ésima linha de  $\Omega$  é preenchida com zeros. Finalmente, como a diferença de fase pode variar levemente para diferentes amostras na mesma linha de  $\Omega$  devido ao ruído térmico, a média aritmética dos elementos de cada linha de  $\Omega$  é calculada, obtendo o vetor  $\bar{\omega} \in \mathbb{C}^{M \times 1}$  e seu  $m$ -ésimo elemento é dado por

$$\bar{\omega}(m) = \frac{1}{N} \sum_{n=1}^N \Omega(m, n). \quad (33)$$

Assim, para compensar a mudança de fase entre dois canais diferentes, o vetor  $\mathbf{c} \in \mathbb{C}^{M \times 1}$  é calculado, cujo  $m$ -ésimo elemento é dado por

$$c(m) = e^{-j\bar{\omega}(m)}. \quad (34)$$

Observe que o vetor de compensação  $\mathbf{c}$  é calculado apenas uma vez durante a inicialização do sistema. As saídas calibradas do arranjo de antenas são dadas pela seguinte expressão

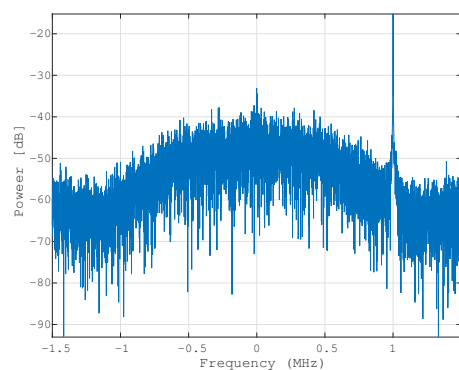
$$\mathbf{X}_c = \text{diag}\{\mathbf{c}\}\mathbf{X}, \quad (35)$$

onde o operador  $\text{diag}\{\cdot\}$  transforma seu vetor argumento na diagonal principal de uma matriz diagonal.

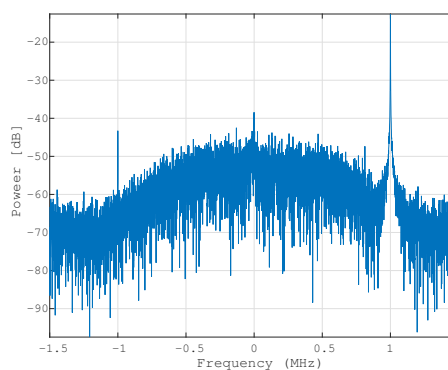
## Filtro rejeita-faixa

No modelo de dados, o ruído é suposto como Gaussiano Circularmente Simétrico de Valor Complexo e i.i.d. O EFT depende dessas propriedades do ruído. Devido aos valores extremamente baixos da Probabilidade de Falso Alarme  $P_{fa}$  o comportamento do ruído teve e ser analisado.

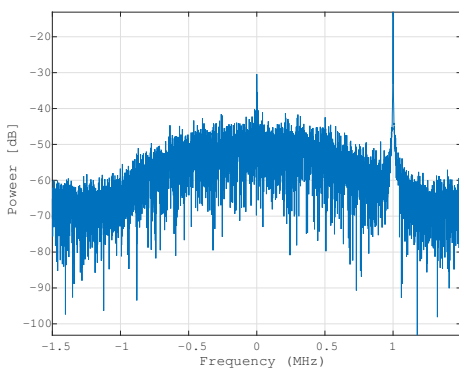
Como a Densidade Espectral de Potência (PSD) mostrada na Fig. 1 não é plana, isto implica em um ruído correlacionado temporalmente. Além disso percebe-se que o hardware insere um ruído específico em 1 MHz. Portanto, para remover esse ruído específico de hardware, um filtro rejeita-faixa deve ser aplicado nessa frequência.



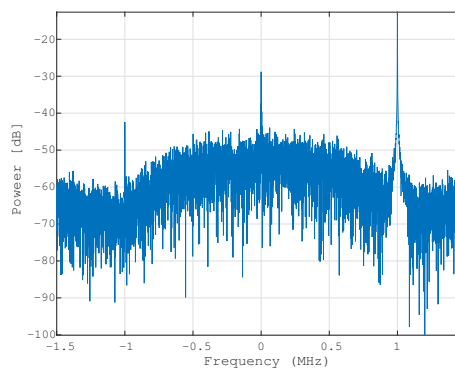
(a) 1ª Antena.



(b) 2ª Antena.



(c) 3ª Antena.



(d) 4ª Antena.

Figure 1: Densidade Espectral de Potência no caso de apenas ruído para cada antena.

## Seleção de amostras

Antes de iniciar o processamento com os algoritmos de pré-processamento e estimadores de DoA, a autenticidade dos dados deve ser verificada. Portanto, se houver um sinal presente, a matriz  $X$  capturada é passado para a seleção de amostragem explicada nesta subseção.

As fases calculadas de cada entrada do SDR é exemplificada na Fig. 2, e foi empiricamente observado que o hardware causa desvios nas fases das amostras em instantes de tempo

aleatórios. Portanto, foi proposta uma abordagem para excluir as amostras com esses desvios de fase para a estimativa DoA.

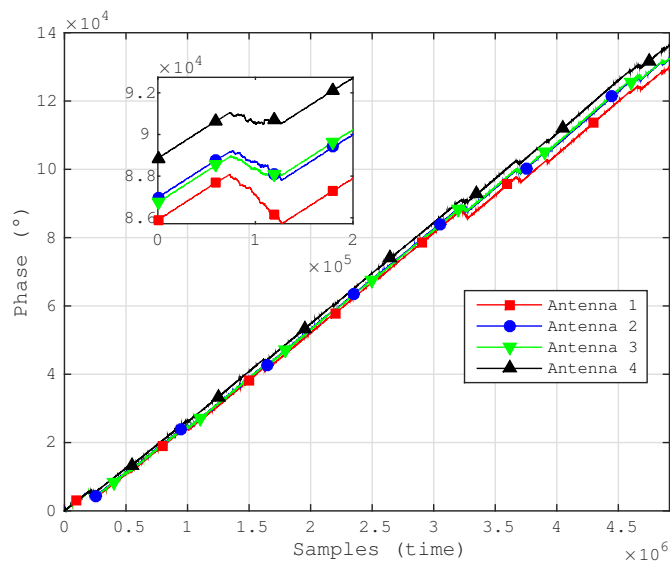


Figure 2: Fase dos dados recebidos em cada antena. Um exemplo de região de desvio de fase é apresentado em destaque.

Observe que há desvios significativos que podem degradar o processo de estimativa DoA. Como mostrado na Fig. 3, tais desvios podem ser melhor visualizados calculando a diferença de fase na dimensão do tempo de acordo com a seguinte expressão

$$\gamma(m, i) = (\phi(m, i + 1) - \phi(m, i))^2, \quad (36)$$

onde  $\gamma(m, i)$  é o valor que contém a diferença quadrática de duas amostras de tempo consecutivas  $i$  e  $i + 1$  do  $m$ -ésimo canal e  $\phi(m, i)$  é o elemento na posição  $m, i$  da matriz  $\Phi$  da Equação (31).

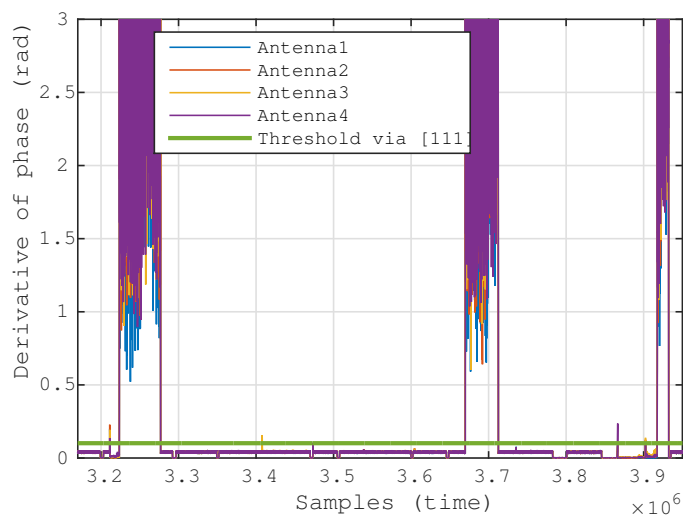


Figure 3: Diferença entre amostras consecutivas da Fig. 2.

Ao detectar os picos na Fig. 3, é possível identificar quais amostras devem ser removidas. Para esta tarefa, a abordagem proposta em [19] é aplicada. A abordagem em [19] retorna a linha verde com o valor do limite. Portanto, as amostras cuja diferença de fase é maior que o limite são removidas.

O resultado após as amostras removidas é apresentado na seguinte equação

$$\mathbf{X}_{\text{cfs}} = [\mathbf{X}_{\text{cf}}(:, 1 : N_1) | \mathbf{X}_{\text{cf}}(:, N_2 : N_3) | \dots | \mathbf{X}_{\text{cf}}(:, N_{T-1} : N_T)], \quad (37)$$

onde  $\mathbf{X}_{\text{cfs}}$  é a matriz com as amostras selecionadas. Note que  $N_T = N$  e os valores de  $N_t$ , para  $t = 1, \dots, T$ , são encontrados comparando os valores de diferença de fase com o limite (linha verde) da Fig. 3.

## MOS, Pre-processamento and Estimação DoA

O EFT [20, 6] foi adotado como o método de seleção de ordem de modelo. O EFT tem as propriedades de deflação que permitem encontrar limites adequados em função da probabilidade de falso alarme ( $P_{\text{fa}}$ ). Explorando a propriedade de deflação e encontrando limiares adequados, o EFT foi o único esquema na literatura analisada a estimar  $d = 1$  na presença de um forte sinal de LOS e  $d = 0$  nas medições com somente de ruído. Vários outros esquemas foram comparados como o Akaike Information Criterion (AIC) [1], Efficient Detection Criterion (EDC) [3], Minimum Description Length (MDL) [2], Stein's Unbiased Risk Estimate (SURE) [4], RADOI [5], ESTimation ERror (ESTER) [7] e Subspace-based Automatic Model Order Selection (SAMOS) [8]. O M-EFT [20, 6, 21] também foi adequado, mas um  $P_{\text{fa}}$  ainda menor foi necessário para encontrar os limites. O cálculo dos limites da EFT requer um  $P_{\text{fa}}$  extremamente baixo. Tal cálculo demanda um alto poder computacional. Portanto, no Apêndice A, é proposto um algoritmo de extrapolação para calcular tais limiares. Observe que nosso algoritmo de extrapolação proposto foi aplicado em [22, 23, 24], embora nenhum detalhe seja fornecido nestes trabalhos. Observe que o motivo de um  $P_{\text{fa}}$  extremamente baixo pode estar relacionado ao comportamento de ruído colorido.

A fim de melhorar ainda mais a precisão dos métodos de estimativa DoA, os esquemas de pré-processamento podem ser aplicados antecipadamente. Neste trabalho foram utilizados como esquemas de pré-processamento o Spatial Smoothing (SPS) [9, 25], Forward Backward Averaging (FBA) [10, 11] e Vandermode Invariance Technique (VIT) [12].

## Resultados

Nesta seção, o dispositivo de detecção e rastreamento de drones é validado nas medições de campo em ambientes externos.

## Configuração para Experimento

Na Fig. 4, descrevemos o ambiente externo usado para as medições de campo. No lado direito, colocamos nosso dispositivo de rastreamento de drone proposto como o receptor, enquanto que do lado esquerdo, o transmissor é colocado. O transmissor é uma plataforma MIMO SDR 2x2 ASPR4 [26], com 50 MHz a 6,0 GHz, largura de banda de canal de 200 kHz a 56 MHz e potência máxima de 10 dBm em cada porta de saída. A frequência central do transmissor e do receptor baseado em arranjo de antenas foi definida em 2,48 GHz.

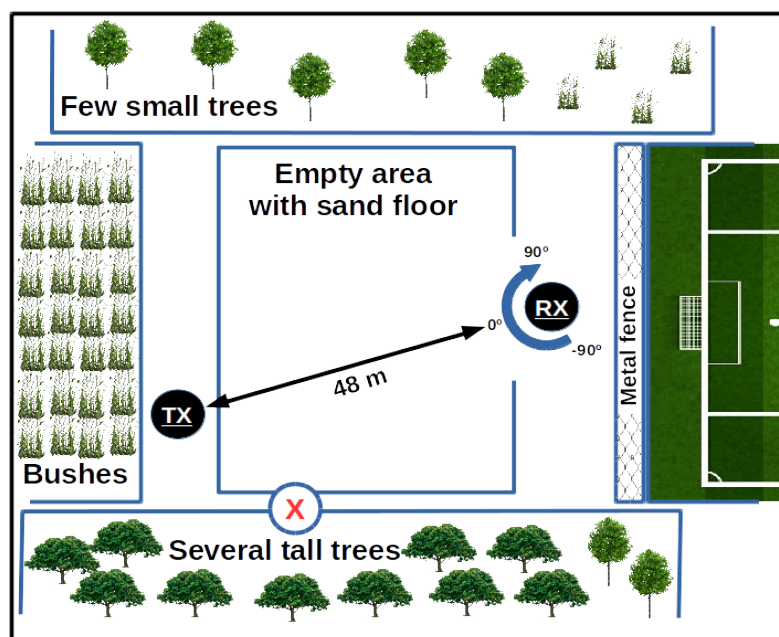


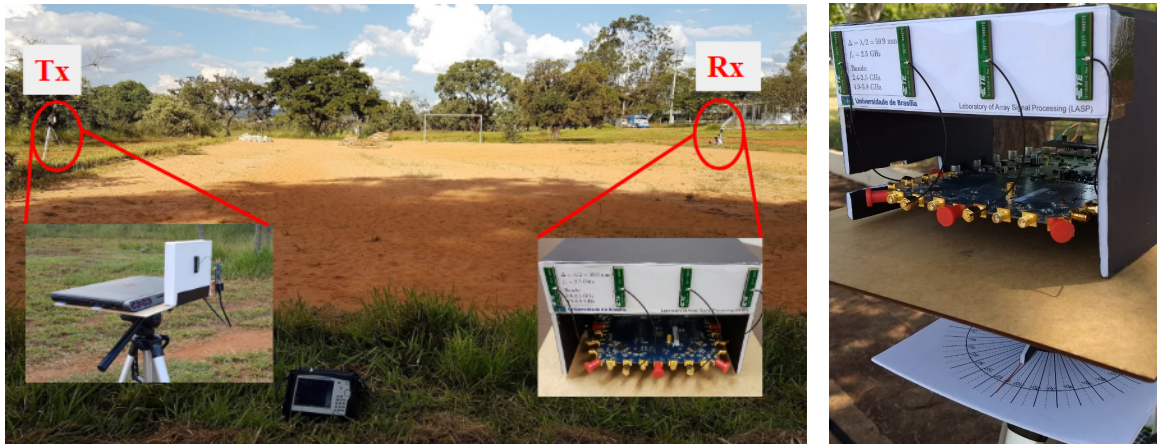
Figure 4: Vista de topo do ambiente externo usado para as campanhas de medição, incluindo as posições do transmissor e do receptor baseado em arranjo de antenas.

O transmissor foi configurado para gerar um sinal de mensagem com modulação MSK para verificar se o dispositivo está funcionando corretamente. Os símbolos transmitidos são sequências pseudo-aleatórias com 1024 bits, um cabeçalho 0xFFFF e um rodapé 0x0000. O dispositivo de rastreamento de drone proposto foi configurado para uma largura de banda de 1 MHz, frequência de amostragem de 3 MHz, frequência portadora de 2,48 GHz, taxa de dados de 500 kbps e 5120 amostras.

O transmissor é fixado e o receptor gira de  $+90^\circ$  até  $-90^\circ$  em passos de  $10^\circ$ . Estes passos são feitos manualmente, portanto o DoA estimado pode ter uma variação devido ao manuseio do operador que controla a rotação, ou até mesmo erro de impressão no transferidor de papel apresentado na Fig. 5(b).

## Resultado do filtro rejeita-faixa

É importante filtrar o sinal recebido para dar um comportamento gaussiano. Nas Figs. 6 e 7, mostramos o histograma para as antenas 1, 2, 3 e 4, com e sem a filtragem. A melhoria



(a) Posições do transmissor e o receptor baseado em arranjo de antenas. (b) Arranjo de antenas montado mostrando o transferidor de papel.

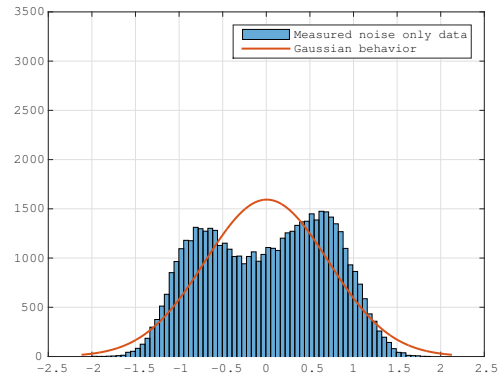
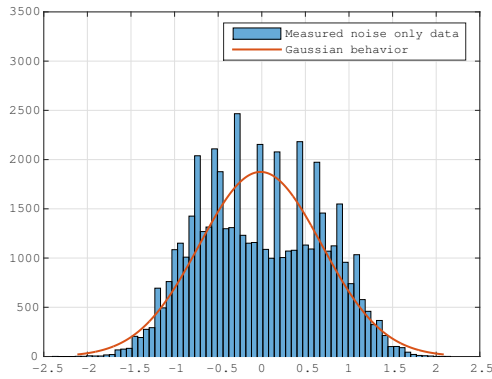
Figure 5: Fotos tiradas durante a campanha de medição no ambiente externo.

com o filtro é notada com o comportamento Gaussiano apresentado na Fig. 7 com os dados após a filtragem.

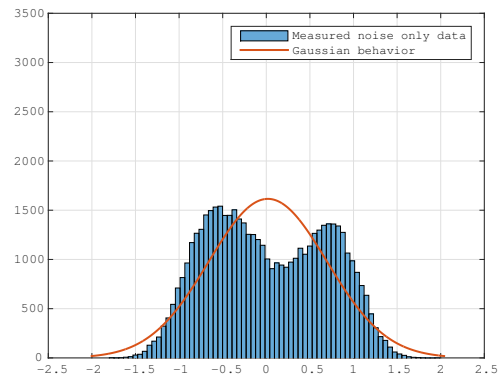
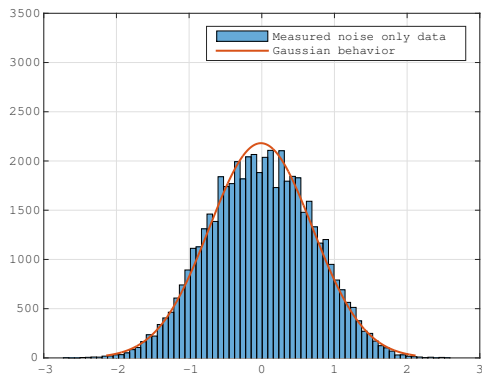
## Resultados para MOS

Foram feitos dois experimentos para testar os métodos MOS. O primeiro experimento usou um transmissor 2x2 MIMO SDR plataforma ASPR4 [26] com potência máxima de 10 dBm. Já o segundo experimento tenta ser mais realista simulando com um roteador [27] um sinal WiFi usado para o VANT se comunicar com o controlador. Outra vantagem do segundo experimento é o caso de apenas ruído, já que o sinal não é transmitido de forma contínua, como ocorre usando o SDR do primeiro experimento.

Para facilitar a visualização, dividimos os resultados de cada experimento em duas imagens, o primeiro experimento é apresentada na Fig. 8 e o segundo experimento é apresentado na Fig. 9, com o comportamento dos métodos MOS. Observe que colocamos duas figuras contendo a potência e os autovalores, além das figuras com os resultados do MOS. Com essas duas imagens, podemos ver o comportamento ao longo do tempo e comparar quando, de fato, um frame contendo sinal foi recebido e quando há apenas ruído.

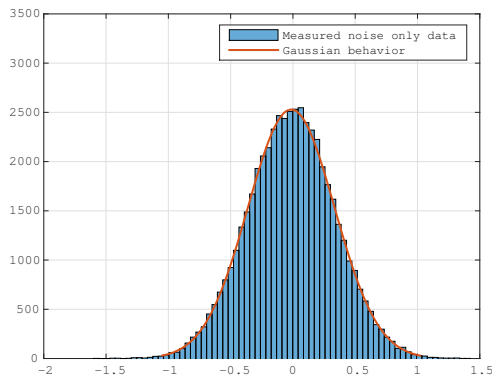


(a) 1ª Antena com 70 caixas, média =  $-0.1035$  e desvio padrão =  $0.7018$ . (b) 2ª Antena com 70 caixas, média =  $-0.0494$  e desvio padrão =  $0.6322$ .

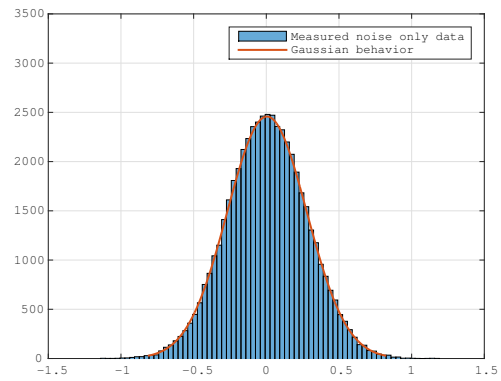


(c) 3ª Antena com 70 caixas, média =  $0.1162$  e desvio padrão =  $0.7377$ . (d) 4ª Antena com 70 caixas, média =  $0.0845$  e desvio padrão =  $0.6836$ .

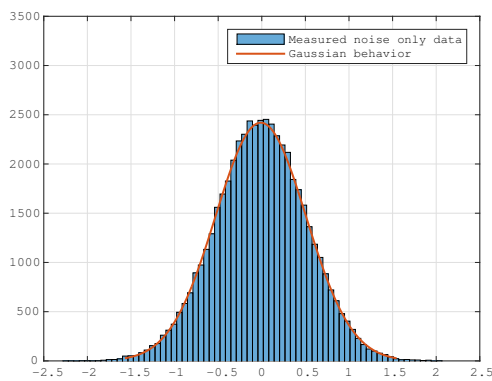
Figure 6: Histograma do caso de ruído apenas para cada antena.



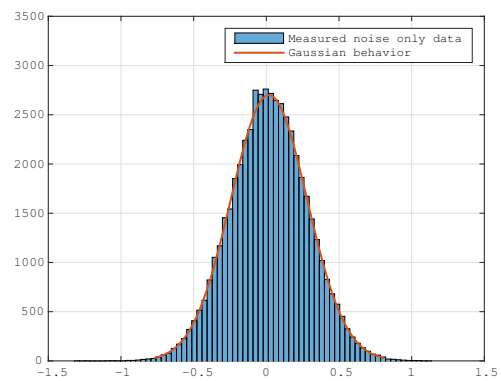
(a) 1ª Antena com 70 caixas, média =  $-0.1035$  e desvio padrão =  $0.7018$ .



(b) 2ª Antena com 70 caixas, média =  $-0.0494$  e desvio padrão =  $0.6322$ .



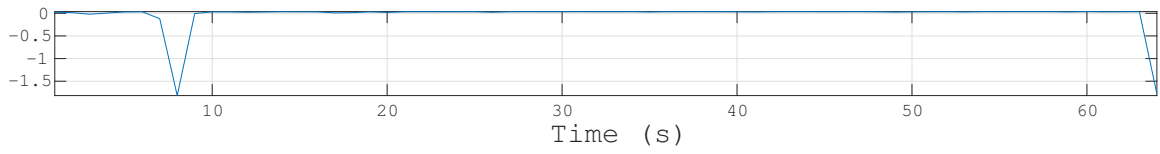
(c) 3ª Antena com 70 caixas, média =  $0.1162$  e desvio padrão =  $0.7377$ .



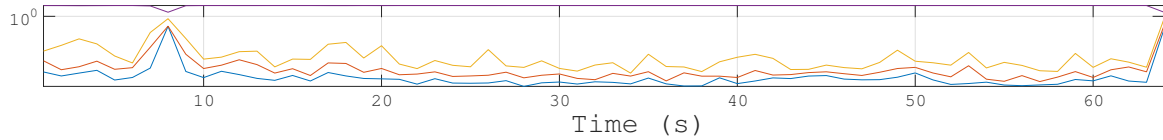
(d) 4ª Antena com 70 caixas, média =  $0.0845$  e desvio padrão =  $0.6836$ .

Figure 7: Histograma do caso de ruído filtrado apenas para cada antena.

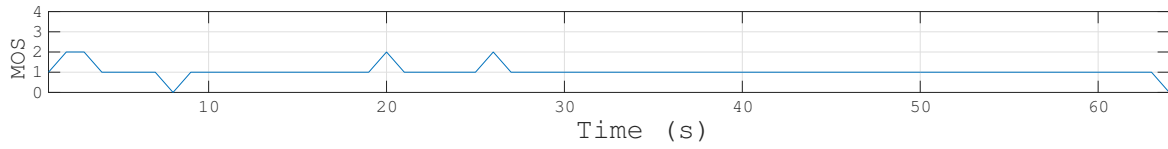




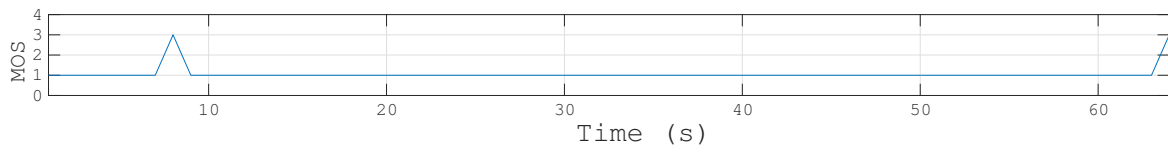
(a) Potência normalizada média (dB) das 4 antenas de dados capturados em ambiente externo



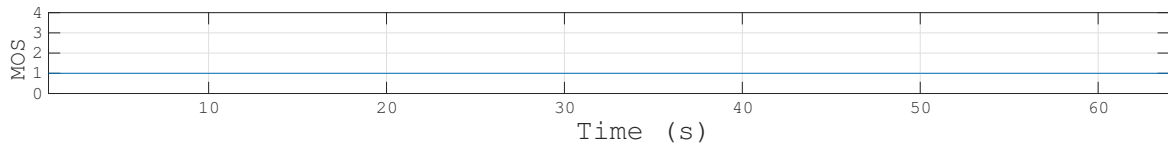
(b) Quatro autovalores (dB) de dados capturados em ambiente externo



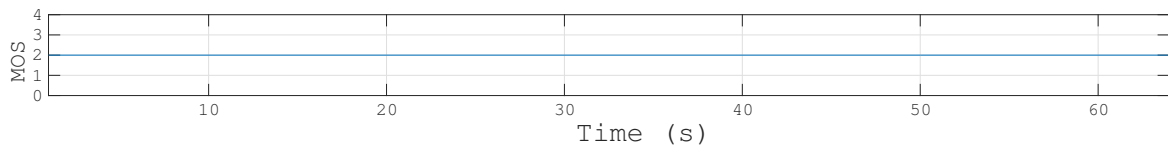
(c) EFT [6] usando os limites dados pelo Appendix A



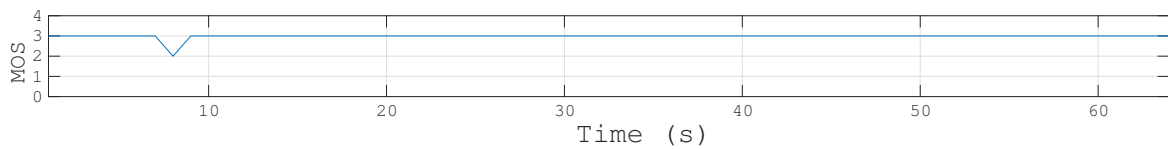
(d) Radoi com abordagem discriminante



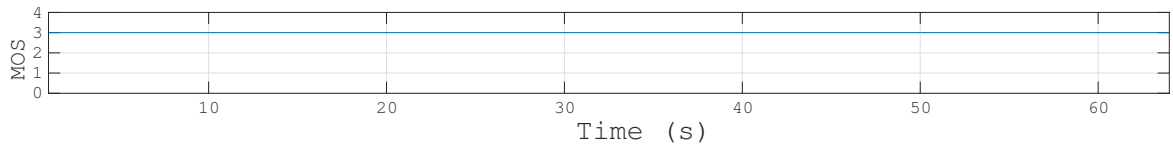
(e) SAMOS [8]



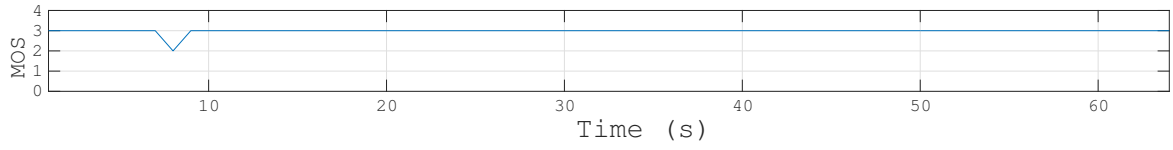
(f) Radoi [5]



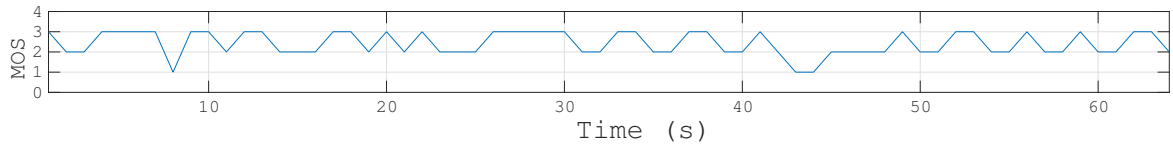
(g) EDC [3]



(h) Akaike [1]

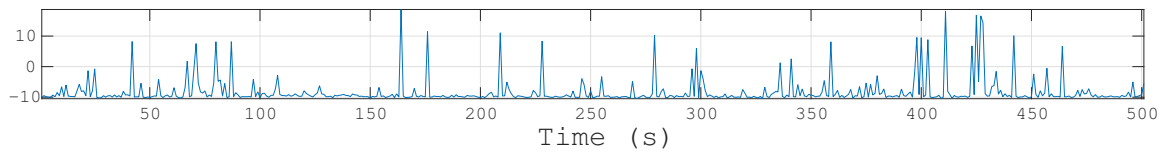


(i) MDL [2]

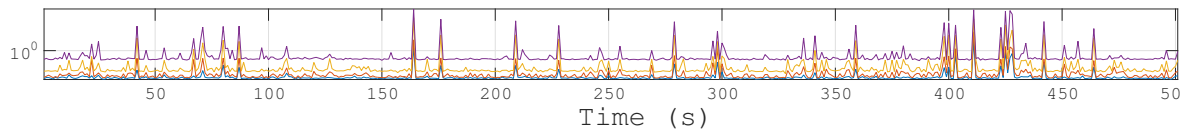


(j) Modified EFT [21]

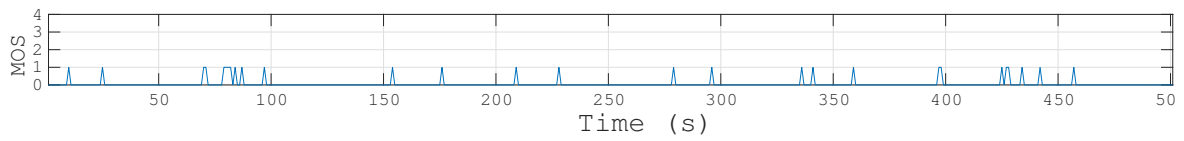
Figure 8: Primeiro experimento para calcular MOS usando um ASRP4 [26] como transmissor.



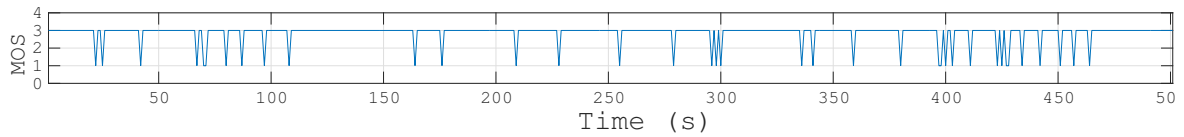
(a) Potência normalizada média (dB) das 4 antenas de dados capturados em ambiente externo.



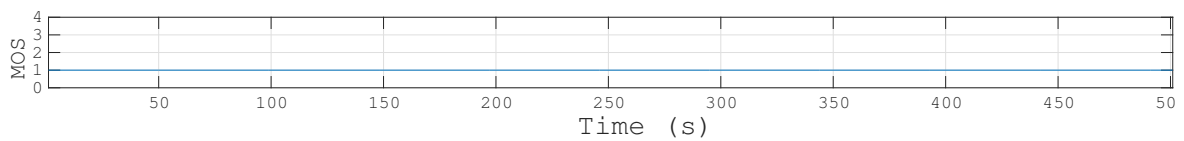
(b) Quatro autovalores de dados capturados em ambiente externo.



(c) EFT [6] usando os limites dados pelo Appendix A.



(d) Radoi with discriminant approach



(e) SAMOS [8]

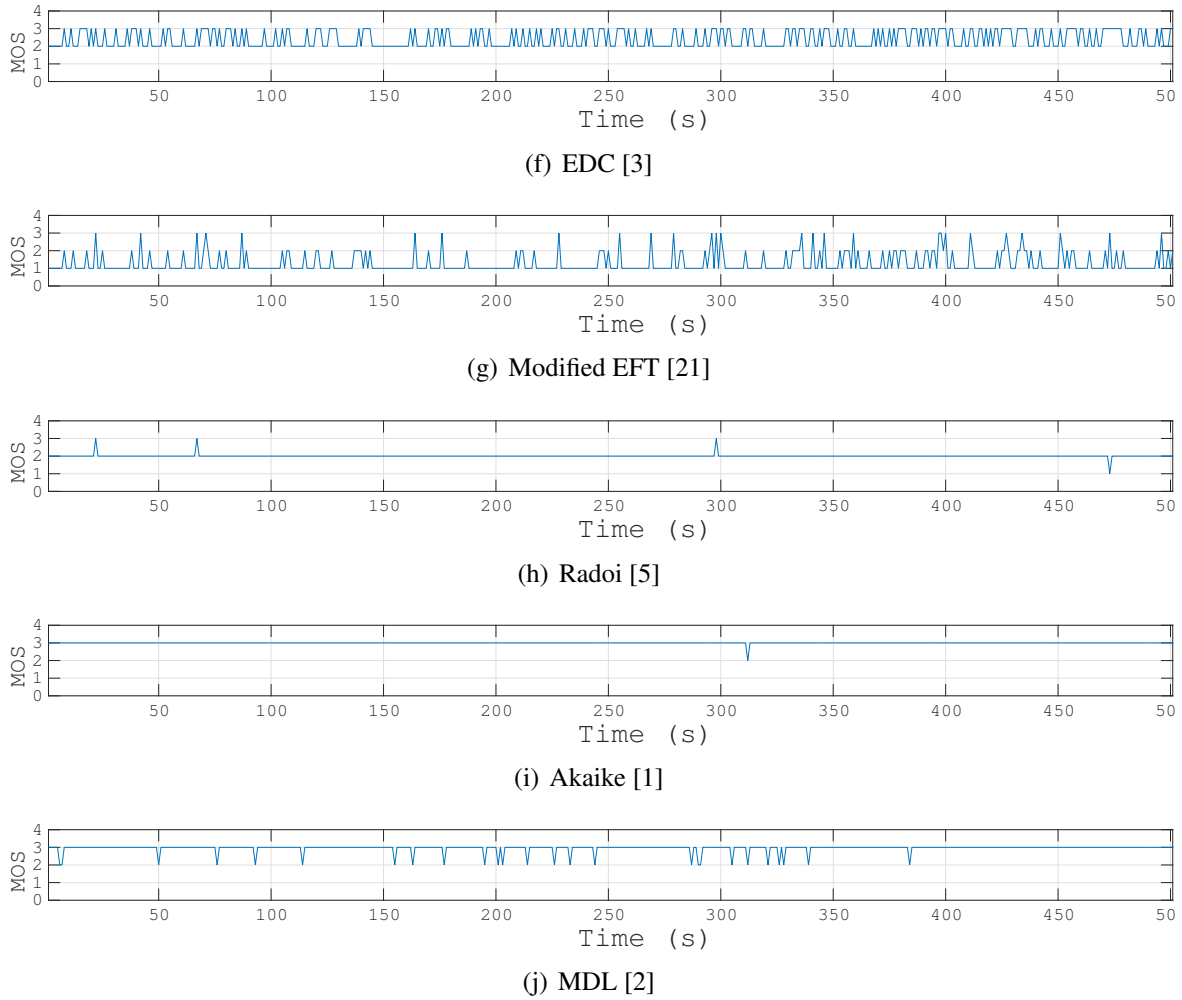


Figure 9: Segundo experimento para calcular MOS usando um roteador [27] como transmissor.

Exceto para o SAMOS [8] e ESTER [7], a matriz  $\mathbf{X}_{cf}$  possui 5120 samples. O processamento computacional para Decomposição em Valores Singulares (SVD) é muito alto para grandes matrizes, portanto foi usado uma matriz  $\mathbf{X}_{cf} \in \mathbb{C}^{4 \times 1000}$  para SAMOS and ESTER.

Apesar de alguns pequenos erros, o EFT usando os limites propostos do Apêndice A tem o melhor desempenho baseado na quantidade de fontes. O Radoi com a abordagem discriminante também se destaca no ponto em que na presença de um sinal reconheceu a melhor quantidade de quadros. No entanto, como apresentado na Fig. 10(d) do segundo experimento, no caso de apenas ruído, ele detecta um número errado de fontes.

## Resultados para Direção de Chegada

Esta seção mostra o desempenho dos esquemas DoA usando o ASRP4 [26] como transmissor. Durante a campanha de medição, a taxa de erro de bit (BER) alcançada foi de  $10^{-4}$ .

A Fig. 5.7 mostra o DoA calculado ao girar a base do arranjo de de antennas ao longo do tempo. Observe que nosso dispositivo proposto funciona corretamente para um DoA que

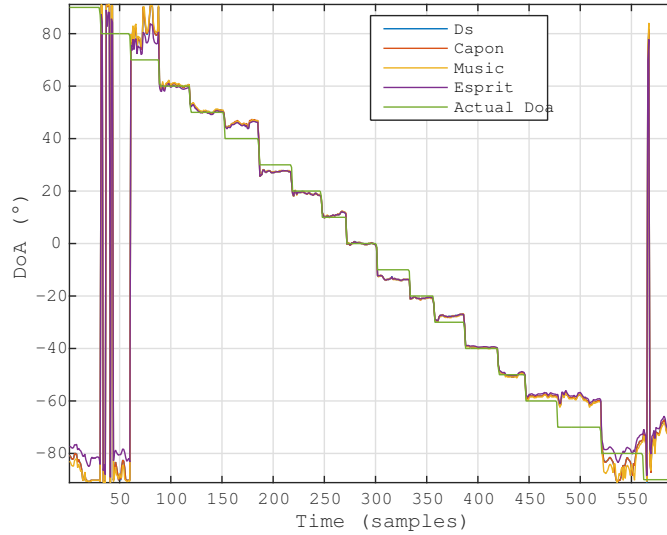


Figure 10: Comparação entre os métodos de estimativa DoA variando de  $+90^\circ$  até  $-90^\circ$  com passos de  $10^\circ$ .

varia de  $-60^\circ$  a  $60^\circ$ . O RMSE, dos métodos DoA já com melhorias de pré-processamento, é dado por (38) e mostrado na Fig. 11. O pior erro DoA do sistema proposto foi de cerca de  $6^\circ$  neste intervalo de  $-60^\circ$  a  $60^\circ$ . A equação do RMSE é dada por

$$\text{RMSE}(\theta_1) = \sqrt{\frac{1}{Q} \sum_{q=1}^Q (\theta_1^{(q)} - \hat{\theta}_1^{(q)})^2} \quad (38)$$

onde  $q$  significa o total de  $Q$  realizações para cada  $10^\circ$  de passo das medições em campo. Em cada  $10^\circ$ , muitos quadros de  $N = 5120$  amostras são adquiridos para cada canal, nos dando a matriz  $\mathbf{X} \in \mathbb{C}^{4 \times 5120}$ .

A evolução dos resultados é apresentada nas Tabelas 4, 5, 6, 7, 8 e 9, as quais apresentam os resultados melhorando com o uso dos esquemas de pré-processamento.

Tabela 4: RMSE para os métodos DoA sem pré-processamento, usando as medidas da Fig. 10

Algoritmo	DS	CAPON	MUSIC	ESPRIT
RMSE	2.3388°	1.6696°	3.9923°	2.8080°
Variância do RMSE	4.2826°	1.0706°	11.5493°	4.0692°

Tabela 5: RMSE para os métodos DoA com pré-processamento VIT [12], usando as medições da Fig. 10

Algoritmo	DS	CAPON	MUSIC	ESPRIT
RMSE	2.3388°	2.0242°	2.8352°	2.9575°
Variância do RMSE	4.2861°	1.8770°	4.8320°	5.2364°

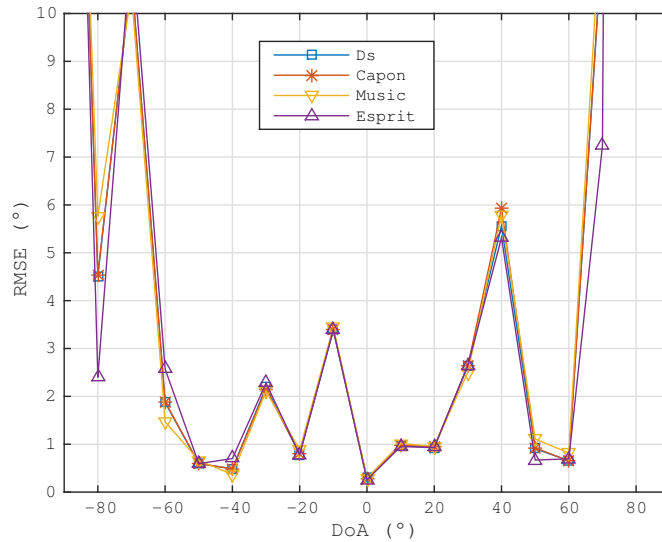


Figure 11: Comparação do RMSE entre o DoA esperado e o DoA estimado já com pré-processamento, variando o ângulo entre  $+90^\circ$  até  $-90^\circ$  with steps of  $10^\circ$ .

Tabela 6: RMSE para os métodos DoA com pré-processamento FBA [10, 11], usando as medições da Fig. 10

Algoritmo	DS	CAPON	MUSIC	ESPRIT
RMSE	$2.1205^\circ$	$1.6833^\circ$	$4.0570^\circ$	$2.4022^\circ$
Variância do RMSE	$3.7932^\circ$	$1.0795^\circ$	$16.7736^\circ$	$3.6046^\circ$

Tabela 7: RMSE para os métodos DoA com pré-processamento SPS [9, 25], usando as medições da Fig. 10

Algoritmo	DS	CAPON	MUSIC	ESPRIT
RMSE	$1.6484^\circ$	$2.4197^\circ$	$1.9689^\circ$	$1.8716^\circ$
Variância do RMSE	$2.3307^\circ$	$2.4003^\circ$	$3.6663^\circ$	$1.8416^\circ$

Tabela 8: RMSE para os métodos DoA com pré-processamento FBA e SPS, usando as medições da Fig. 10

Algoritmo	DS	CAPON	MUSIC	ESPRIT
RMSE	$1.6548^\circ$	$1.6745^\circ$	$1.6813^\circ$	$1.8776^\circ$
Variância do RMSE	$2.3628^\circ$	$2.5452^\circ$	$2.4180^\circ$	$1.8904^\circ$

Tabela 9: RMSE para os métodos DoA com pré-processamento FBA, SPS e VIT, usando as medições da Fig. 10

Algoritmo	DS	CAPON	MUSIC	ESPRIT
RMSE	$1.6361^\circ$	$1.6676^\circ$	$1.6475^\circ$	$1.6757^\circ$
Variância do RMSE	$2.2671^\circ$	$2.5168^\circ$	$2.3600^\circ$	$2.1913^\circ$

Por fim, a evolução do desempenho em médias do RMSE apresentadas nas tabelas 4, 5, 6, 7, 8 e 9 e desenhada na Fig. 12.

Como mostrado na Tabela 10, o custo total da solução proposta para rastreamento de

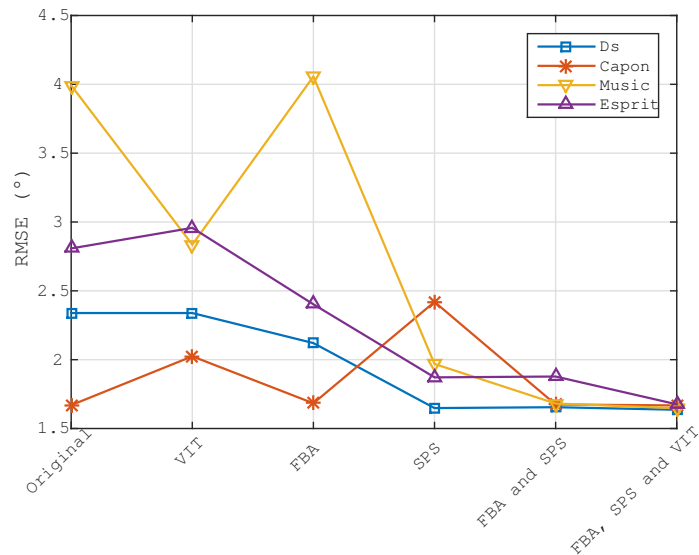


Figure 12: Comparação de desempenho entre os resultados do RMSE apresentados nas Tabelas 4, 5, 6, 7, 8, 9

drones é US\$ 2,222, enquanto as soluções [28] e [29] custam US\$ 226.000 e US\$ 120.000, respectivamente. Portanto, nossa solução, já pronta para uso, custa menos de 2 % das soluções comerciais em [28] e [29].

Tabela 10: Tabela de preços do hardware usado na construção do dispositivo proposto de baixo custo para rastreamento de Drones

Hardware	Cost (US\$)
AD-FMCOMMS5-EBZ-ND [30]	1080
4 × Dual-Band Antenna 2.4 & 5GHz [18]	11
ZYNQ 7000 Zc702 [31]	999
Power Divider 2.4-6GHz 30Watts RoHS IP67 [32]	109
5 × cable 305mm HPP100 SMA [33]	23
<b>Total</b>	<b>2222</b>

# Sumário

<b>1</b>	<b>INTRODUÇÃO</b> .....	<b>1</b>
<b>2</b>	<b>FORMULAÇÃO DO PROBLEMA E MODELO DE DADOS</b> .....	<b>6</b>
<b>3</b>	<b>REVISÃO BIBLIOGRÁFICA</b> .....	<b>8</b>
3.1	MÉTODOS DE SELEÇÃO DA ORDEM DO MODELO .....	8
3.1	CRITÉRIO TEÓRICO DE INFORMAÇÃO.....	8
3.1.2	STEIN’S UNBIASED RISK ESTIMATOR .....	10
3.1.3	RADOI.....	10
3.1.4	EXPONENTIAL FITTING TEST .....	11
3.1.5	SAMOS E ESTER .....	12
3.2	MÉTODOS DE PRÉ-PROCESSAMENTO DE DADOS .....	13
3.2.1	SPATIAL SMOOTHING.....	13
3.2.2	FORWARD BACKWARD AVERAGE .....	13
3.2.3	TRANSFORMAÇÃO DE INVARIÂNCIA DE VANDERMONDE .....	14
3.3	MÉTODOS DE ESTIMAÇÃO DA ORDEM DE CHEGADA .....	15
3.3.1	BEAMFORMING.....	15
3.3.1.1	ATRASO E SOMA .....	15
3.3.1.2	CAPON.....	16
3.3.1.3	MULTIPLE SIGNAL CLASSIFICATION .....	16
<b>4</b>	<b>FRAMEWORK E DISPOSITIVO DE BAIXO CUSTO BASEADO EM ARRAY DE ANTENAS PARA RASTREAMENTO DE DRONES</b> .....	<b>18</b>
4.1	MONTAGEM DO HARDWARE PARA A CALIBRAÇÃO .....	19
4.2	MONTAGEM DO HARDWARE PARA CAMPANHA DE RASTREAMENTO DE DRONE .....	21
4.3	ESTRUTURA DO FRAMEWORK .....	21
4.3.1	CORREÇÃO DE DESVIO DE FASE.....	22
4.3.2	FILTRO REJEITA BANDA .....	23
4.3.3	SELEÇÃO DE AMOSTRAS E DA MATRIZ X .....	23
4.3.4	MOS, PRÉ-PROCESSAMENTO E ESTIMAÇÃO DE DOA.....	25
<b>5</b>	<b>RESULTADOS</b> .....	<b>28</b>

5.1	CONFIGURAÇÕES PARA OS EXPERIMENTOS .....	28
5.2	RESULTADOS DO FILTRO REJEITA BANDA .....	30
5.3	RESULTADOS PARA MOS .....	31
5.4	RESULTADOS PARA DOA .....	34
<b>6</b>	<b>REFERÊNCIAS BIBLIOGRÁFICAS.....</b>	<b>41</b>



# LIST OF FIGURES

1	Densidade Espectral de Potência no caso de apenas ruído para cada antena.....	xiv
2	Fase dos dados recebidos em cada antena. Um exemplo de região de desvio de fase é apresentado em destaque. ....	xv
3	Diferença entre amostras consecutivas da Fig. 2.....	xv
4	Vista de topo do ambiente externo usado para as campanhas de medição, incluindo as posições do transmissor e do receptor baseado em arranjo de antenas. ....	xvii
5	Fotos tiradas durante a campanha de medição no ambiente externo. ....	xviii
6	Histograma do caso de ruído apenas para cada antena. ....	xix
7	Histograma do caso de ruído filtrado apenas para cada antena. ....	xx
8	Primeiro experimento para calcular MOS usando um ASRP4 [26] como transmissor. ....	xxii
9	Segundo experimento para calcular MOS usando um roteador [27] como transmissor. ....	xxiii
10	Comparação entre os métodos de estimativa DoA variando de $+90^\circ$ até $-90^\circ$ com passos de $10^\circ$ . ....	xxiv
11	Comparação do RMSE entre o DoA esperado e o DoA estimado já com pré-processamento, variando o ângulo entre $+90^\circ$ até $-90^\circ$ with steps of $10^\circ$ . ....	xxv
12	Comparação de desempenho entre os resultados do RMSE apresentados nas Tabelas 4, 5, 6, 7, 8, 9 .....	xxvi
2.1	Formulation problem presenting the Uniform Linear Array with with M antennas and drawing impinging signals from an Unmanned Aerial Vehicle.....	6
4.1	Hardware components for building the low cost drone tracking device.....	19
4.2	Radiation pattern for the antenna from Fig. 4.1(d). Image taken from [118]....	19
4.3	Assembled components for the hardware calibration of four receive channels. The components are a microprocessor (uProc) and FPGA motherboard, a SDR, a power divider and cables. ....	20
4.4	Proposed low cost antenna array based drone tracking device with 4 element ULA and a 4 x 4 MIMO SDR.....	21
4.5	Flowchart of proposed framework solution for DoA estimation.....	22
4.6	Power Density Spectrum of the noise only case for each antenna. ....	24

4.7	Phase of the received data in each antenna. An example of phase deviation region is highlighted in the zoom area.....	25
4.8	Phase difference between consecutive samples from Fig. 4.7. ....	26
4.9	Expanded version of box 6 presented in Fig. 4.5 .....	27
5.1	Photos taken during the measurement campaigns of the outdoor scenario. ....	29
5.2	Top view of the outdoor scenario for the measurement campaigns including the positions of the transmitter and of the antenna array based receiver .....	29
5.3	Histogram of the noise only case for each antenna.....	30
5.4	Histogram of the filtered noise only case for each antenna.....	31
5.5	First experiment to calculate the MOS by schemes from 3.1 using an ASRP4 [26] as transmitter. ....	33
5.6	Second experiment to calculate the MOS by schemes from 3.1 using a router [27] as transmitter. ....	34
5.7	Comparison between the DoA estimation schemes by varying the DoA from +90° to -90° with steps of 10°. ....	35
5.8	RMSE comparison between the Expected DoA and the DoA estimation combined with pre-processing schemes by varying the angle from +90° to -90° with steps of 10°. ....	36
5.9	Comparison of performance between the RMSE results presented in tables 5.1, 5.2, 5.3, 5.4, 5.5, 5.6 .....	37
A.1	Log linear extrapolation based on two points given by $P_{fas}$ and Thresholds $\eta_P$ . ....	51
A.2	Thresholds for extrapolated data using computation with $M=4$ and $N=41$ . ....	52
A.1	Selection of the port on Mission Planner software. ....	54
A.2	Selection of the frame layout on Mission Planner software.....	55
A.3	Accelerometer Calibration on Mission Planner software.....	55
A.4	Compass Calibration on Mission Planner software. ....	56
A.5	Battery selection on Mission Planner software.....	57
A.6	Sonar selection on Mission Planner software.....	57
A.7	Radio calibration on Mission Planner software. ....	58
A.8	Flight modes configuration on Mission Planner software. ....	61
A.9	Failsafe configuration on Mission Planner software. ....	62
A.10	GeoFence configuration on Mission Planner software. ....	62

# Chapter 1

## Introduction

Applications of direction of arrival (DoA) techniques have dramatically increased in various areas ranging from the traditional wireless communication systems [34, 35] and rescue operations [36] to GNSS systems [37, 38, 39, 40] and drone tracking in public and private events. Over the last years, Unmanned Aerial Vehicles (UAVs) have been a major concern of airspace control bodies and military due to possible terrorist attacks and illegal activities. In 2015, there were more than nine hundred incidents involving drones and aircrafts in the United States [41], whereas, in April 2016, an UAV reached an aircraft landing at the Heathrow airport in London [42]. In Dubai 2016, four drones invaded the airport, one of the busiest in the world, interrupting the landings and take-offs, causing an estimated loss of one million dollars [43]. In October 2017 in Canada, the first reported collision of a drone and a commercial airplane has occurred [44] and, still in 2017, an UAV invaded the Congonhas airport in São Paulo, Brazil, causing an estimated loss of approximately 1 million Reais due to the interruption of its services [45]. Most recently, in December 2018 a total of 155 flights have been canceled and about 10 thousand passengers have been disrupted by drones flying over one of the UK's busiest airports, the Gatwick Airport [46]. In addition, [47] and [48] show cases of drones in football stadiums, threatening the fans safety.

As shown before, these vehicles can, by carelessness, cause millions in losses. Therefore, recently police forces and security companies have drawn their attention to drone tracking devices in order to provide the safeness of citizens and clients. In this sense, the development of low cost devices for drone tracking is fundamental to fit such demands.

In order to detect the presence of drones and to track them, there is a variety of mechanical, optical or antenna array based solutions in the market. For instance, the mechanical solution in [28] detects a drone within 3 km for targets up to 55 cm in diameter, and classifies the model of the drone within 1.1 km. The position accuracy (azimuth) in [28] is  $1^\circ$ . In [49], a rechargeable portable drone tracking device can detect and indicate the direction of a drone in a  $360^\circ$  azimuth even with weak Line of Sight (LoS) component. The device in [49] allows the communication with other devices by using an Application Programming Interface (API) framework. No technical information and patent about the principles behind

the device in [49] and its DoA accuracy are provided. In [29], an antenna array based system is shown to detect with a 1 km range and with  $1^\circ$  accuracy or with a 7 km range and with  $3^\circ$  accuracy.

In [50], an application has been proposed for drone detection. According to the developers, the app has an average range of 106 meters. The system allows the detection of almost 95 % of all types of drones. However, the solution in [50] does not indicate the position or the direction of the drone.

In [51], a square shaped 16 element antenna array is connected to switches so that a four channel SDR can select four antennas at each side of the square, allowing a  $360^\circ$  DoA estimation in outdoor environments. Each side of the square performs a  $\pm 45^\circ$  azimuth estimation. According to the authors, three Yagi antennas were used as sources at specific points, and maximum DoA error of  $5^\circ$  is achieved. No information is provided about the real distance between the sources and the receive array.

In [52], DoA estimation using an electronically steerable parasitic array radiator (ESPAR) with 12 parasitic elements and one active monopole is performed for wireless sensor network (WSN) applications. The authors calibrated the ESPAR array using an anechoic chamber. Since the main subject of [52] is the calibration, no measurement outdoor or indoor campaigns are performed by the authors.

In [53], a four element of quasi-Yagi antenna array system is applied for DoA estimation using the MUSIC algorithm, whereas the Minimum Description Length (MDL) criterion is used to estimate the amount of multipath components. Only two measurements are performed for two specific positions showing an error of  $1^\circ$ . No information is provided about the experimental scenario.

In [54], several DoA estimation techniques are compared considering a horizontal uniform linear array (ULA) with 12 elements inside an anechoic chamber. The measurements were conducted varying the DoA from  $-20^\circ$  to  $20^\circ$  in steps of  $4^\circ$ . The DoA estimation errors were smaller than  $2^\circ$ . The Min-Norm approach [55] MUSIC [15] although it has a higher standard deviation.

Finally, in [56], the authors developed system using a five-port reflectometers, that allows to simultaneously measure the DoA and Time of Arrival (ToA) of coherent and incoherent signals, connected to seven quasi-Yagi antennas, with one reflectometer for each antenna. The MUSIC algorithm is applied for the DoA estimation, providing an error of  $2^\circ$  for one source and  $0,5^\circ$  for two sources. The measurements were performed in a non-reflective environment.

In this dissertation, it is proposed a low cost antenna array based drone tracking device for outdoor environments. To the best of our knowledge, there is no state-of-the-art low cost off-the-shelf antenna array based device applied to drone tracking. The drone tracking is a challenging task due to the several possible modulation schemes for the data transmission, propagation phenomena, such as multipath components, and the possible long operational

distances. In the next chapter, the simplified state-of-the-art antenna array based solutions for DoA estimation in the literature is detailed.

The device proposed is divided into hardware and software parts. The hardware part of the proposed device is based on off-the-shelf components such as an omni-directional antenna array, a 4 channel Software Defined Radio (SDR) platform, a FPGA motherboard and a laptop. The software part includes state-of-the-art algorithms for model order selection (MOS), pre-processing and DoA estimation, including others specific pre-processing and calibration steps in order to remove random errors and increase the DoA accuracy. The state-of-the-art algorithm Exponential Fitting Test (EFT) [6] is used for MOS. For pre-processing schemes, Spatial smoothing (SPS) [9], Forward Backward Averaging (FBA) [10, 11] and Vandermonde Invariance Transformation (VIT) [12] are used. And finally, the DoA estimation used the Delay and Sum [13], Minimum Variance Distortion-less Response (MVDR) or Capon's beamformer [14], MULTiple SInal Classification (MUSIC) [15] and Estimation of Signal Parameters via Rotation Invariance Techniques (ESPRIT) [16] algorithms.

This work also makes a comparative approach between several MOS algorithms in order to choose the winner, which is used in the proposed device. Additionally presents individual results of improvement brought by each preprocessing algorithm and its influence on the accuracy of the DoA estimation.

To build a product, it is necessary to prove the feasibility of it. The frequencies used for communications by the UAVs in the market are very important in order to select the frequency range or the array to be used. A survey research, presented in Table 1.1 selected a variety of popular companies and manufactures of UAVs and its three most highlighted models for amateur or professional civilian use. Some companies have '-' as model name, that means the company have only one or two models. Note that the most used frequencies are 2.4 GHz followed by 5 GHz. Therefore the experiments of this dissertation, and the previous one [57], are focused on 2.4 GHz and 5.8 GHz, respectively.

An additional contribution of this work is to provide the complete configuration of the PixHawk [58, 59] controller for beginners. This configuration is important for future researchers to be able to continue work using UAVs and can be found in Attachment A.

Building the array of antennas with low-cost hardware is a challenging proposition, since it deals with difficulties such as mutual coupling, phase calibration and hardware problems. In the remainder of this work is described each of this problems and the proposed solutions.

This thesis is divided as follows: Chapter 2, the formulation problem and data model is presented. Next, in Chapter 3, is presented the review of State of the Art for Model Order Selections Schemes and Direction of Arrival methods that are used in the proposed device. Then, in Chapter 4, it is proposed a low cost antenna array based drone tracking device for outdoor environments, including a complete description of the hardware and software, and the steps involved for assembling, calibration and signal processing. In Section 5, the proposed solution is validated by means of measurement campaigns in an outdoor scenario

presenting the results and methods accuracy. In Section 6, conclusions are drawn.

Table 1.1: Table of frequencies (in MHz) used on popular UAVs

<b>Company</b>	<b>Model<sub>1</sub> (M1)</b>	<b>Model<sub>2</sub> (M2)</b>	<b>Model<sub>3</sub> (M3)</b>	<b>433</b>	<b>902-928</b>	<b>2400-2483.5</b>	<b>5150-5850</b>
3D Robotics	Solo [60]	X8+ [61]	IRIS [62]	M2 e M3	M2 and M3	M1	
AeroEnvironment	Quantix [63]	-	-		M1		
Autel Robotics	EVO [64]	X-Star Premium [65]	X-Star [65]		M2	M1 and M3	M2 and M3
Blade	C. 220 BNF Basic [66]	Theory XL [67]	Torrent 110 [68]				M1, M2 and M3
DJI	Mavic 2 Pro [69]	Phantom 4 Pro [70]	Matrice 200 [71]			M1, M2 and M3	M1, M2 and M3
EHang	GhostDrone [72]	Falcon [73]	-			M1 and M2	M2
Flyability	Elios [74]	-	-			M1	
GoPro	Karma [75, 76]	-	-			M1	
Hubsan	X4 Air Pro [77]	X4 Plus [78]	X4 Pro [79]			M1, M2 and M3	M1 and M3
Ideafly	Storm - 800 [80]	Grasshopper F210 [81]	Poseidon-480 [82]			M1,M2 and M3	M2 and M3
Parrot SA	Anafi [83]	Bebop 2 [84]	Disco [85]			M1, M2 and M3	M1, M2 and M3
Powervision	PowerEgg [86]	PowerEye [87]	-			M1 and M2	
Redcat racing	Carbon 210 [88]	-	-			M1	M1
SkyDrones	Zangão [89, 90]	Pelicano [91, 90]	Strix-AG [92, 90]			M1 and M2	M3
Syma	X5SW [93]	X8 pro [94]	Z1 [95]			M1, M2 and M3	
traxxas	Aton [96]	QR-1 [97]	Latrax Alias [98]			M1, M2 and M3	
Udi RC	Discovery 2 plus [99]	Peregrine [100]	Predator [101]			M1, M2 and M3	
Walkera	Furious 215 [102]	Voyager 4 [103]	VITUS [104]			M1, M2 and M3	M1, M2 and M3
WL toys	Q696-A [105]	V383 Stunt drone [106]	Q696-D [107]			M2 and M3	M1
Yuneec	Typhoon 4K [108]	Tornado H920 [109]	H520 [110]			M1,M2 and M3	M1, M2 and M3

# Chapter 2

## Problem formulation and data model

We assume  $d$  far field sources transmitting narrow-band signals. These planar wavefront signals impinge over a receive antenna array with  $M$  omni-directional elements uniformly and linearly disposed.

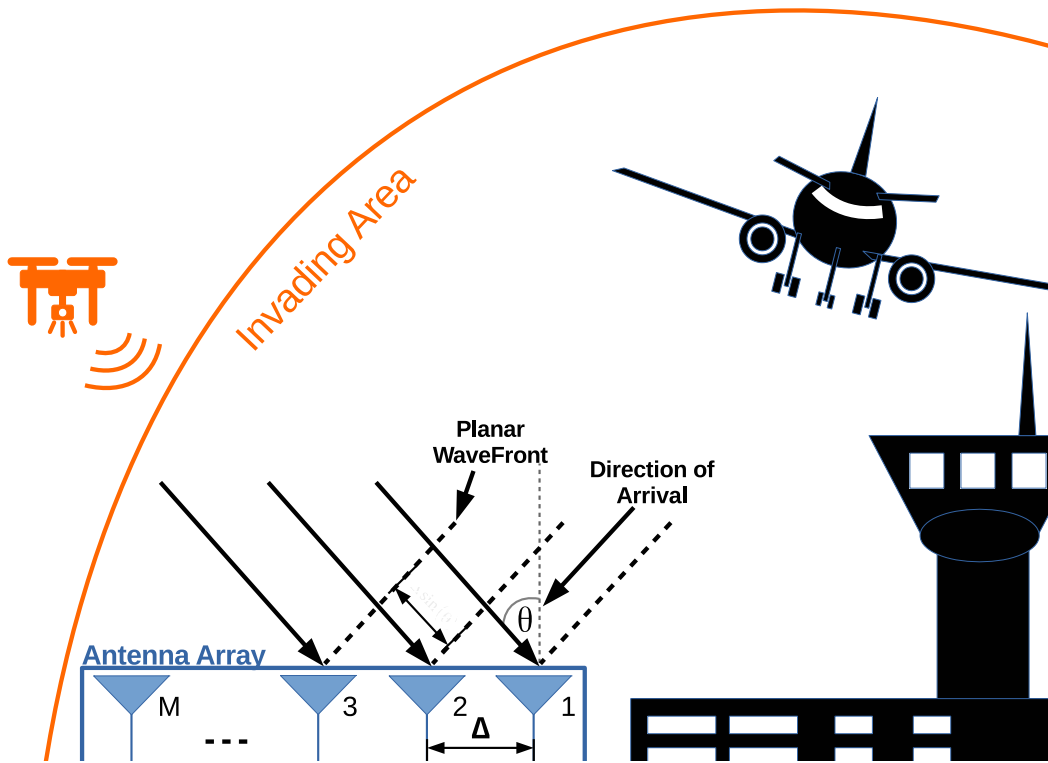


Figure 2.1: Formulation problem presenting the Uniform Linear Array with with  $M$  antennas and drawing impinging signals from an Unmanned Aerial Vehicle

The space  $\Delta$  between two adjacent antennas is equal to  $\frac{\lambda}{2}$ , where  $\lambda$  is the wavelength of the carrier signal as presented in Fig. 2.1. The received signals at the antenna array can be



written in a matrix fashion as follows

$$\mathbf{X} = \mathbf{A}\mathbf{S} + \mathbf{N} \in \mathbb{C}^{M \times N}, \quad (2.1)$$

where  $\mathbf{A} \in \mathbb{C}^{M \times d}$  is the steering matrix and its  $i$ -th steering vector is given by

$$\mathbf{a}(\mu_i) = \left[ 1 \quad e^{j\mu_i} \quad e^{2j\mu_i} \quad \dots \quad e^{j(M-1)\mu_i} \right]^T \in \mathbb{C}^{M \times 1}, \quad (2.2)$$

where  $\mu_i$  is the spatial frequency that can be mapped into the direction of arrival of the  $i$ -th source,  $\theta_i$ , by the following expression:  $\mu_i = \frac{2\pi\Delta \sin \theta_i}{\lambda}$ .  $\mathbf{S} \in \mathbb{C}^{d \times N}$  is the symbol matrix with  $N$  being the number of snapshots.  $\mathbf{N} \in \mathbb{C}^{M \times N}$  stands for the noise matrix, whose elements are assumed as Complex-Valued Circularly Symmetric Gaussian and identically and independently distributed (i.i.d.).

Given (2.1) and assuming that the noise and the signal are uncorrelated, the covariance matrix can be computed by

$$\mathbf{R}_{\mathbf{X}\mathbf{X}} = E\{\mathbf{X}\mathbf{X}^H\} = \mathbf{A}\mathbf{R}_{\mathbf{S}\mathbf{S}}\mathbf{A}^H + \mathbf{R}_{\mathbf{N}\mathbf{N}}, \quad (2.3)$$

where  $\mathbf{x}$  is one column vector from  $\mathbf{X}$ ,  $(\cdot)^H$  is the Hermitian operator and  $E\{\cdot\}$  is the expected value operator. In practice, the sample covariance matrix is calculated as follows:

$$\hat{\mathbf{R}}_{\mathbf{X}\mathbf{X}} = \frac{\mathbf{X}\mathbf{X}^H}{N} \in \mathbb{C}^{M \times M}. \quad (2.4)$$

The DoA techniques used along this paper exploit the sample covariance matrix in (2.4). As shown in Chapter 4, the matrix  $\mathbf{X}$  is pre-processed before the computing of the covariance matrix  $\hat{\mathbf{R}}_{\mathbf{X}\mathbf{X}}$ .

The goal of our proposed drone tracking device is to estimate the Direction of Arrival (DoA)  $\theta_1$  of the line of sight (LoS) signal component from a drone in an outdoor scenario. It is assumed that there is no obstruction of the LoS component. Therefore, the LoS component is assumed to have the greatest power in comparison with the Non-LoS components. Mathematically, it is expressed as

$$\|\mathbf{a}(\mu_1)\mathbf{s}(\mu_1)\|_F > \|\mathbf{a}(\mu_i)\mathbf{s}(\mu_i)\|_F, \quad (2.5)$$

for  $i = 2, \dots, d$ . The operator  $\|\cdot\|_F$  stands for the Frobenius norm and  $d$  is the model order, in other words  $d$  means the number of sources.

# Chapter 3

## Literature Review

In this chapter are presented all the methods used to construct the proposed low cost antenna array based drones tracking device for outdoor environments. First of all, in Section 3.1 the Model Order Selection (MOS) schemes, which define the number of UAVs present in the scanned airspace and are a requirement for some DoA schemes, are described. Next, to provide improved accuracy in DoA schemes, preprocessing algorithms are presented in Section 3.2. Finally, in Section 3.3 the best-known DoA literature schemes are reviewed.

### 3.1 Model Order selection methods

One of the prerequisites for proper operation of the proposed device lies in a good selection of the matrix  $\mathbf{X}$  obtained from the array. In other words, the noise only case needs to be avoided. One of the ways of this selection is by estimating the order of the model. Concluding, the device only calculates the Direct of Arrival (DoA) if it is in the presence of a signal. In addition, several DoA estimation algorithms depend on the knowledge of the model order.

In the real world we do not know how many signals are arriving in our receiver array, so several techniques were proposed in the literature in order to estimate this number of sources. It can be classified as eigenvalues or subspace based, and are usually called model order selection (MOS) techniques. In this chapter, the used methods are described and the results of this techniques are drawn in Chapter 5.

#### 3.1.1 Information Theoretic Criteria

Akaike's Information Criterion (AIC) [1], Minimum Description Length (MDL) [2] and Efficient Detection Criterion (EDC) [3] have similar expressions with different penalty functions. Therefore they are classified as Information Theoretic Criteria (ITC). Due to the contribution in [111], that give a good performance with the expression for AIC and MDL, they

are referred and used as benchmarks. A general expression is used in ITC methods and is given by

$$J(P) = -N(M - P)\log\left(\frac{g(P)}{a(P)}\right) + p(P, M), \quad (3.1)$$

where  $P$  is the candidate value to the estimated model order  $\hat{d}$ , which is obtained minimizing the  $J(P)$ .  $g(P)$  and  $a(P)$  are the geometric and arithmetic mean of  $P$  smallest eigenvalues  $\lambda_i$  of the ascending sorted main diagonal of a covariance matrix  $\hat{\mathbf{R}}_{\mathbf{X}\mathbf{X}}$  defined in (2.4). The  $p(P, M)$  is a function of the number of independent parameters called penalty function and each method defines its own.

The MDL log-likelihood criterion is defined by

$$\text{MDL}(P) = -\log\left\{\frac{\prod_{i=P+1}^M \lambda_i^{\frac{1}{M-P}}}{\frac{1}{M-P} \sum_{i=P+1}^M \lambda_i}\right\}^{(M-P)N} + \frac{1}{2}p(M, N)\log N, \quad (3.2)$$

where  $M$  denotes number of sensors,  $N$  is the number of snapshots and  $\lambda_i$  is the  $i$ -th eigenvalue of the  $\hat{\mathbf{R}}_{\mathbf{X}\mathbf{X}}$ .  $p(\kappa)$  is the penalty function that change with the proprieties of the matrix and the preprocessing applied. It is defined as follows

$$p(M, N) = \left\{ \begin{array}{l} P(2M - P + 1) \text{ For real matrices} \\ P(M + P + 1) \text{ For real FB - averaging} \\ P(2M - P) \text{ For complex matrices} \\ 0.5P(2M - P + 1) \text{ For complex FB - averaging} \end{array} \right\}. \quad (3.3)$$

For the AIC, the log-likelihood criterion is given by

$$\text{AIC}(P) = -\log\left\{\frac{\prod_{i=P+1}^M \lambda_i^{\frac{1}{M-P}}}{\frac{1}{M-P} \sum_{i=P+1}^M \lambda_i}\right\}^{(M-P)N} + p(M, N). \quad (3.4)$$

Finally, for the EDC, the log-likelihood criterion is given by

$$\text{EDC}(P) = -\log\left\{\frac{\prod_{i=P+1}^M \lambda_i^{\frac{1}{M-P}}}{\frac{1}{M-P} \sum_{i=P+1}^M \lambda_i}\right\}^{(M-P)N} + p(M, N)C_N. \quad (3.5)$$

where  $C_N$  can be any function of  $N$  such that obey this two proprieties

$$\lim_{N \rightarrow \infty} \frac{C_N}{N} = 0, \quad \lim_{N \rightarrow \infty} \frac{C_N}{\ln(\ln(N))} = \infty. \quad (3.6)$$

We use  $C_N = \sqrt{N \log(\log(N))}$  as presented on [7, 112] for which they obtained the best results.

Note that AIC, MDL and EDC are divided in two parts. In the first part, the log-likelihood criterion function does not change, whilst the second part the penalty function (3.3) changes with the method. The result of the influence on eigenvalues made by increasing  $P$  causes the first part of the criterion to decrease but at the same time the second part to increase. Therefore we vary  $P$ , in order to find the value that minimizes the AIC( $P$ ) and MDL( $P$ ). Then, the estimated number of sources is defined by  $\hat{d} = \arg \min_P [\text{MDL}(P), \text{AIC}(P) \text{ or } \text{EDC}(P)]$ .

### 3.1.2 Stein's Unbiased Risk Estimator

In the more recent Stein's Unbiased Risk Estimator (SURE) approach [4],  $P$  is found in order to minimize the risk  $\hat{R}(P)$  as follows

$$\begin{aligned} \hat{R}(P) &= (M - P)\hat{\sigma}_P^2 + 2\sigma^2 P + (\hat{\sigma}_P^4 - 2\hat{\sigma}_P^2\sigma^2 \frac{4\hat{\sigma}_P^2\sigma^2}{N}) \sum_{i=1}^P \frac{1}{\lambda_i} + C \\ C &= \frac{4\sigma^2}{N} \sum_{i=1}^P \sum_{j=P+1}^M \frac{\lambda_i - \hat{\sigma}_P^2}{\lambda_i - \lambda_j} + \frac{2\sigma^2}{N} P(P - 1) - \frac{2\sigma^2}{N} (M - 1) \sum_{i=1}^P \left(1 - \frac{\hat{\sigma}_P^2}{\lambda_i}\right), \end{aligned} \quad (3.7)$$

where  $\hat{\sigma}_P^2 = \frac{1}{M-P} \sum_{i=P+1}^M \lambda_i$  and the noise variance  $\sigma^2$  is estimated via Random Matrix Theory (RMT) algorithm defined in [4]. In the RMT, to estimate the noise variance, one of the steps uses a crude estimate of  $\sigma^2$  with a certain percentile, about 25 and 30-th of smallest noise corrected eigenvalues, or even the median. Then, the estimated number of sources is defined by  $\hat{d} = \arg \min_P \hat{R}(P)$ .

### 3.1.3 RADOI

According to [5], in the eigenvalue based methods, the method called RADOI performs better for signals contaminated with colored noise. The main idea is that estimating  $\hat{d}$  is equivalent to finding how many eigenvalues are associated to each signal and noise subspaces. The empirical functions  $g_1$  and  $g_2$  are the discriminant functions related to the noise and signal subspaces respectively, and are given by

$$g_1(P) = \frac{\lambda_{P+1}}{\sum_{i=2}^M \lambda_i}, \quad g_2(P) = \frac{\xi_P}{\sum_{i=1}^{M-1} \xi_i}, \quad P = 1, \dots, M - 1 \quad (3.8)$$

where  $\xi_P = 1 - \frac{\alpha(\lambda_P - \mu_P)}{\mu_P}$ ,  $\mu_P = \frac{1}{M-P} \sum_{i=P+1}^M \lambda_i$  and  $\alpha = \left[ \frac{\lambda_P - \mu_P}{\mu_P} \right]^{-1}$  e  $\lambda$  contains the autocorrelation matrix eigenvalues.

Then, the estimated number of sources  $\hat{d}$  is defined as the first positive value from the following expression

$$\text{RADOI}(P) = g_1(P) - g_2(P). \quad (3.9)$$

### 3.1.4 Exponential Fitting Test

The EFT [6] is based on the approximation that the profile of the ordered noise eigenvalues have an exponential behavior. The profile  $a(M, N)$  can be expressed as

$$a(M, N) = \sqrt{\frac{1}{2} \left( \frac{15}{M^2 + 2} - \sqrt{\frac{225}{(M^2 + 2)^2} - \frac{180M}{N(M^2 - 1)(M^2 + 2)}} \right)}. \quad (3.10)$$

Given that  $\hat{d} = M - P^*$ , the goal is to vary  $P$  such that we find  $P^*$  that  $\hat{\lambda}_{M-P} \ll \lambda_{M-P}$ , where  $\hat{\lambda}_{M-P}$  and  $\lambda_{M-P}$  stands for predicted  $(M - P)^{\text{th}}$  noise eigenvalue and  $M - P$  actual eigenvalue, respectively. Note that the EFT assumes the smallest eigenvalue as a noise eigenvalue. Therefore,  $P$  varies from 1 to  $M - 1$ . Using (3.10), the authors in [6] derived the following expression

$$\hat{\lambda}_{M-P} = (P + 1) \cdot \left( \frac{1 - a(P + 1, N)}{1 - a(P + 1, N)^{P+1}} \right) \cdot \hat{\sigma}^2, \quad (3.11)$$

$$\hat{\sigma}^2 = \frac{1}{P + 1} \sum_{i=0}^N \lambda_{M-i}, \quad (3.12)$$

where  $\hat{\sigma}^2$  is the estimated noise power.

In order to improve further the performance of the EFT approach, thresholds coefficients  $\eta_P$  are computed using noise-only simulated data following Complex-Valued Circularly Symmetric Gaussian and identically and independently distributed (i.i.d.) as indicated in Chapter 2. Depending on the  $\eta_P$ , there are two hypothesis.

$$H_P : \left| \frac{\lambda_{M-P} - \hat{\lambda}_{M-P}}{\hat{\lambda}_{M-P}} \right| \leq \eta_P \quad (3.13)$$

$$\bar{H}_P : \left| \frac{\lambda_{M-P} - \hat{\lambda}_{M-P}}{\hat{\lambda}_{M-P}} \right| > \eta_P \quad (3.14)$$

where  $H_P : \lambda_{M-P}$  is a noise eigenvalue and  $\bar{H}_P : \lambda_{M-P}$  is a signal eigenvalue. In order to have all  $\eta_P$  depending on the  $P_{\text{fa}}$ , it is possible define the  $P_{\text{fa}}$  as

$$P_{\text{fa}} = \Pr[\hat{d} \neq 0 | d = 0] \quad (3.15)$$

where  $\Pr[\cdot]$  is the probability operator. Note that the  $\eta_P$  thresholds are obtained by Monte Carlo simulations carried out in the only-noise scenario following the steps in [6] and by

choosing the following amount of realizations

$$I = \frac{10}{P_{fa}}. \quad (3.16)$$

Depending on the noise behaviour and the parameters of the scenario [112, 23], the  $P_{fa}$  can be extremely low. Therefore, the computational complexity of (3.16) can be prohibitive. In order to overcome such limitation, it is proposed in Appendix A an extrapolation approach to compute the thresholds for extremely low values of  $P_{fa}$ .

### 3.1.5 SAMOS and ESTER

Different from the eigenvalue based, this Subsection presents the subspace based methods. Subspace based Automatic Model Order Selection (SAMOS) [8] and ESTimation ERror (ESTER) [7] use the shift invariance propriety and the steering matrix  $\mathbf{A}$  having the Vandermonde structure.

ESTER is based on the DoA Estimating algorithm ESPRIT [16], which needs a prior value of model order  $d$ . According to [7], varying the candidate of model order  $P \in \{1, \dots, \min(M, N)\}$  on algorithm, an erroneous  $P$  disturbs the estimation of sinusoids. In other words, for  $P \neq d$  the shift invariance propriety is not valid. Based on this fact, the authors derive error bounds  $\mathbf{E}_E(P)$  as follows

$$\begin{aligned} \mathbf{E}_E(P) &= \mathbf{W}(P)_\uparrow - \mathbf{W}(P)_\downarrow \Phi(P), \\ \Phi(P) &= (\mathbf{W}(P)_\downarrow)^\dagger (\mathbf{W}(P)_\uparrow), \end{aligned} \quad (3.17)$$

where  $\mathbf{W}(P)_\uparrow$  contains the first left  $P$  eigenvectors as columns,  $\mathbf{W}(P)_\downarrow$  contains the last right  $P$  eigenvectors as columns and  $\{\cdot\}^\dagger$  denotes the pseudo-inverse operator.

Then the estimated number of sources  $\hat{d}$  from ESTER [7], is defined as the value of  $P$  that maximizes the expression  $\frac{1}{(\|\mathbf{E}_E(P)\|_2)^2}$ , where  $\|\cdot\|_2$  stands for the Euclidean vector norm (or 2-norm).

SAMOS [8] defines a matrix joining the  $\mathbf{W}(P)_\uparrow$  and  $\mathbf{W}(P)_\downarrow$  matrices, given expression  $\mathbf{U}(P) = [\mathbf{W}(P)_\uparrow | \mathbf{W}(P)_\downarrow] \in (M - 1) \times 2P$ . According to the Authors, there are three hypothesis to be analyzed:

- $P > d$ , the rank of  $\mathbf{U}(P)$  is increased by 2;
- $P < d$ , the rank of  $\mathbf{U}(P)$  is equal to  $\min(2P, d)$ ;
- $P = d$ , the  $\lambda_{d+1}, \dots, \lambda_{2d}$  singular values of  $\mathbf{U}(P)$  are equal to zero.

Based on previous hypothesis the estimated number of order  $\hat{d}$  is the value of  $P$  that

maximizes the expression  $\frac{1}{E_S(P)}$ , where  $E_S(P)$  is defined as follows

$$E_S(P) = \frac{1}{P} \sum_{i=P+1}^{2P} \lambda_i^{tb}. \quad (3.18)$$

## 3.2 Pre-processing of data methods

In general, the preprocessing methods are used on the matrix  $\mathbf{X}$  transforming it into a matrix  $\mathbf{Z}$  that will be used by the other desired algorithms. Thus, with several concepts reviewed in this chapter, the preprocessing algorithms allow a better accuracy in the results of the DoA methods.

### 3.2.1 Spatial Smoothing

Spatial smoothing (SPS), proposed in [9] and discussed further in [25], has been used in coherent signals. The spatial smoothing technique introduced by [9] makes it possible to use DoAs algorithms in presence of arbitrary signal correlation under certain conditions. The most restrictive aspect of the SPS technique is that it requires a uniform spaced array.

As our linear antenna array is a 4-element ULA, as well as respecting the above condition, it can be divided into two sub-arrays with  $M_{\text{sub}} = 3$  elements each,  $\{1, \dots, M_{\text{sub}}\}$  forming the first sub-array and  $\{2, \dots, M_{\text{sub}} + 1\}$ . It is called  $M_{\text{sub}}$  the number of sub-array sensors and  $M$  the array number of sensors. Is applied SPS in  $\mathbf{X}$  to get a measurement matrix  $\mathbf{X}_{SS}$  that has a rank greater than or equal to  $d$ . A selection matrix  $\mathbf{J}$  which selects the elements to be concatenated, is defined. This approach and  $\mathbf{X}_{SS}$  is drawn as follows,

$$\mathbf{J}_l^{(M)} = [\mathbf{0}_{M_{\text{sub}} \times (l-1)} \mathbf{I}_{M_{\text{sub}}} \mathbf{0}_{M_{\text{sub}} \times (L-l)}], \quad l \in 1 \leq l \leq L, \quad (3.19)$$

$$\mathbf{X}_{SS} = [\mathbf{J}_1^{(M)} \mathbf{X} \quad \mathbf{J}_2^{(M)} \mathbf{X} \quad \dots \quad \mathbf{J}_L^{(M)} \mathbf{X}] \in \mathbb{C}^{M_{\text{sub}} \times LN}, \quad (3.20)$$

where  $L$  denotes the number of sub-arrays. Note that the number of sensors is reduced from  $M$  to  $M_{\text{sub}}$  after the spatial smoothing.

### 3.2.2 Forward Backward Averaging

One of the most commonly used preprocessing schemes, the Forward Backward Averaging (FBA) [10, 11] is used in a wide range of DoA methods. It effectively doubles the data consequently improving the variances of the estimators. As other methods, FBA has requirements to be valid, such as samples be taken in a geometry that is also reversible, arrays must be centro-symmetric and the properties of the process under consideration be approximately

the same independent of the orientation of the time or space axis [10]. With this characteristics, FBA presents the desirable effect of reducing correlation between signals, as occurs in a multipath environment.

The basic operation of FBA relies on the fact that the matrix  $\mathbf{A}$  remains the same even if its elements are reversed and complex conjugated [113]. It is possible to apply the FBA with this simple equations,

$$\mathbf{X}_{FB} = \frac{1}{\sqrt{2}}[\mathbf{X}, \mathbf{J}_1 \mathbf{X}^* \mathbf{J}_2], \quad (3.21)$$

where  $\mathbf{J}_1 \in \mathbb{C}^{M \times M}$  and  $\mathbf{J}_2 \in \mathbb{C}^{N \times N}$  are selection matrices with 1's on the antidiagonal and 0's elsewhere.

### 3.2.3 Vandermonde Invariance Transformation

Different from interpolation methods [114, 115], the Vandermonde Invariance Transformation (VIT) [12] does not solve the physical array imperfections, it keeps the Vandermonde structure in a desired direction changing the others, making the uniform Vandermonde response of the array into one with a non uniform phase response. It also acts as beamformer conserving power at a direction of interest and reduces the power from the others.

VIT defines a  $\mathbf{T}_{\text{vit}}(\mathbf{r}) \in \mathbb{C}^{M \times M}$  and multiplies it by  $\mathbf{v}(\theta) = [1, e^{j\mu_i}, e^{2j\mu_i}, \dots, e^{j(M-1)\mu_i}]^T$  containing a Vandermonde structure. It gives us the following result

$$\tilde{\mathbf{v}}(\theta) = \mathbf{T}_{\text{vit}}(\mathbf{r})\mathbf{v}(\theta) = \left( \frac{e^{j\mu(\theta)} - r}{1 - r} \right)^{M-1} \cdot \begin{pmatrix} 1 \\ e^{j\nu(\theta)} \\ \vdots \\ e^{(M-1)\nu(\theta)} \end{pmatrix} \quad (3.22)$$

where  $r \in \mathbb{C}$  are the complex roots of the polynomials, and can be chosen considering the noise suppression and the linearity of the output. Note that the original phase  $\mu$  is mapped into a new phase  $\nu$ , that can be expressed as follows

$$\nu = \arctan \left( \frac{2K \cdot \sin(\theta)}{1 - K^2 + (1 + K^2) \cdot \cos(\theta)} \right), \quad (3.23)$$

where  $K = \frac{r+1}{r-1}$  is a phase amplification.

To apply VIT on the received signal, it is built a transformation matrix  $\mathbf{T}_f(K, \theta)$  in order to transform the received matrix  $\mathbf{X}$  into a new matrix  $\mathbf{Y}$  that has the proprieties described before. This transformation is drawn as follows

$$\mathbf{Y} = \mathbf{T}_f(r, \theta)\mathbf{X} \in \mathbb{C}^{M \times N}. \quad (3.24)$$



To find  $\mathbf{T}_f$ , the matrix  $\mathbf{T}_{\text{vit}}$  is multiplied by a diagonal focusing matrix  $\mathbf{F}(\theta) = \text{diag}\{\mathbf{v}(\theta)\}$ , where  $\mathbf{v}(\theta) = [1, e^{j\mu_i}, e^{2j\mu_i}, \dots, e^{j(M-1)\mu_i}]$  containing a Vandermonde structure and  $\text{diag}\{\cdot\}$  transforms its argument vector into the main diagonal of a diagonal matrix. Then, the  $\mathbf{T}_f$  is given by

$$\mathbf{T}_f(K, \theta) = \mathbf{T}_{\text{vit}}(\mathbf{r})\mathbf{F}(\theta). \quad (3.25)$$

Finally, the new data matrix  $\mathbf{Y}$  is now used by the DoA algorithms obtaining a more precise DoA estimation with a cost of additional computational load.

### 3.3 Direction of Arrival methods

The Direction of Arrival of a signal has application in various areas such as radars and telecommunications. This is further boosted by the recent rise of Unmanned Aerial Vehicles (UAVs), thereby increasing the concern of airspace control bodies and even governments for illegal actions and even terrorist attacks. In this way the estimation of a target's location can be obtained using the Arrival Direction and some action could be taken. There are a variety of algorithms and their derivations, however in this work it is focused on the best-known classical methods of DoA detection, presented in this Section.

#### 3.3.1 Beamformings and subspace based methods

The conventional beamforming methods have the basic idea of "scanning" the array in a specific direction and measure the output power. When the "scanned" direction is the same as a DoA of any signal, the output power will reach the maximum. The following equation addresses this concept

$$P(\theta) = \mathbf{w}^H \mathbf{R}_{XX} \mathbf{w} \quad (3.26)$$

where  $\{\cdot\}^H$  is the Hermitian operator and  $\mathbf{R}_{XX}$  is the covariance matrix. Most recent beamforming methods have been developed by measuring the output power (3.26) with different forms of the  $\mathbf{w}$  called spatial filter as it is discussed in this Section.

##### 3.3.1.1 Delay and Sum

For the most simple algorithm Delay and Sum [13] when the scanned direction  $\theta$  matches with the real DoA from the source the output power  $P(\theta)$  will reach a peak or maximum point.

$$\mathbf{w}_{DS} = \frac{\mathbf{a}(\theta)}{\sqrt{\mathbf{a}^H(\theta) \mathbf{a}(\theta)}}. \quad (3.27)$$

where  $\mathbf{a}(\theta)$  is the steering vector in direction of  $\theta$  with Vandermonde structure.

By inserting the weight vector (3.27) into (3.26), the output power as a function of angle of arrival is obtained as follows

$$P_{\text{DS}}(\theta) = \frac{\mathbf{a}(\theta)^H \mathbf{R}_{\text{XX}} \mathbf{a}(\theta)}{\mathbf{a}(\theta)^H \mathbf{a}(\theta)}. \quad (3.28)$$

This method has a poor resolution. However, to increase its accuracy, it is possible to add more sensors increasing the amount of storage data. In our case this is not possible since there is hardware limitations.

### 3.3.1.2 Capon

The Minimum Variance Distortion-less Response (MVDR) or Capon's beamformer [14] achieve the maximum power when the beam with  $\theta$  matches the direction of a signal. The weight vector described from Capon is given by,

$$\mathbf{w}_{\text{CAP}} = \frac{\mathbf{R}_{\text{XX}}^{-1} \mathbf{a}(\theta)}{\mathbf{a}(\theta)^H \mathbf{R}_{\text{XX}}^{-1} \mathbf{a}(\theta)}. \quad (3.29)$$

Substituting (3.29) into (refeq:principalBeam), the spatial Capon power is given by

$$P_{\text{CAP}}(\theta) = \frac{1}{\mathbf{a}(\theta)^H \mathbf{R}_{\text{XX}}^{-1} \mathbf{a}(\theta)}. \quad (3.30)$$

According to [113] CAPON works well when there is only one incoming signal present. However when there is more than one, the array output power contains signal contributions from the desired and undesired angles. In the particular desired direction, Capon minimizes the variance of the array output and allows the signal to pass from this direction with no distortion.

### 3.3.1.3 Multiple Signal Classification

The last beamformer present in this work is the MULTIPLE Signal Classification (MUSIC) [15]. It is based on noise subspace, which requires a prior knowledge of number of sources. The number of sources is used to select the first ordered largest  $d$  eigenvalues. Then, the noise subspace  $\mathbf{V}_n$  is defined as a matrix formed by the eigenvectors related to the small ordered eigenvalues  $\lambda_i \in \{d + 1, \dots, M\}$ .

$$P_{\text{MUS}}(\theta) = \frac{1}{\mathbf{a}^H(\theta) \mathbf{V}_n \mathbf{V}_n^H \mathbf{a}(\theta)}, \quad (3.31)$$

As in the previous beamformers, the signals impinging on the array have DoAs given by the  $d$  tallest peaks from the spectrum  $P_{\text{MUS}}(\theta)$ .

### 3.3.1.4 ESPRIT

Finally, Estimation of Signal Parameters via Rotation Invariance Techniques (ESPRIT) [16] is based on two identical subarrays in order to apply the shift invariance staggered in time. This method is similar to MUSIC at the point that is a subspace based approach, except to the fact that MUSIC uses the noise subspace and ESPRIT uses the signal subspace.

First, the Singular Value Decomposition (SVD) is applied to the data array  $\mathbf{X}$ . The SVD gives us the matrix  $\mathbf{U} \in \mathbb{C}^{M \times M}$  of the right singular vectors, that are the eigenvectors from covariance matrix. Now the signal subspace  $\mathbf{U}_s$  can be found by taking the first  $d$  eigenvectors, sorted according to eigenvalues, from  $\mathbf{U}$ . In other words, the matrix  $\mathbf{U}$  can be rewritten as  $\mathbf{U} = [\mathbf{U}_s | \mathbf{U}_n]$  with  $\mathbf{U}_s \in \mathbb{C}^{M \times d}$ .

As the steering matrix  $\mathbf{A}$  generate the same subspace of  $\mathbf{U}_s$ , there is a nonsingular matrix  $\mathbf{T} \in \mathbb{C}^{d \times d}$  such that  $\mathbf{A} \approx \mathbf{U}_s \mathbf{T}$ . The shift invariance propriety give us the assumption

$$\mathbf{J}_1 \mathbf{U}_s \mathbf{T} \Phi = \mathbf{J}_2 \mathbf{U}_s \mathbf{T} \Leftrightarrow \mathbf{J}_1 \mathbf{U}_s \Psi = \mathbf{J}_2 \mathbf{U}_s \quad (3.32)$$

where  $\Psi = \mathbf{T} \Phi \mathbf{T}^\dagger \in \mathbb{C}^{d \times d}$  is a non singular matrix signal subspace rotating operator,  $\{\cdot\}^\dagger$  being the pseudo-inverse operator,  $\mathbf{J}_1$  and  $\mathbf{J}_2$  are the selection matrices and  $\Phi = \text{diag}[\phi_1, \dots, \phi_d]$  is the diagonal matrix that has the eigenvalues representing the estimates of phase factors  $e^{j\mu}$  containing the DoA information.

As a result, if the signal subspace  $\mathbf{U}_s$  can be estimated,  $\Psi$  and its eigenvalues containing DoAs information can then be found as follows

$$\Psi = \mathbf{J}_1 \mathbf{U}_s^+ \mathbf{J}_2 \mathbf{U}_s. \quad (3.33)$$

With  $\Psi$  and  $\Phi$  sharing the same eigenvalues, it is possible to apply the eigenvalue decomposition (EVD) on  $\Psi$  and obtain the  $\phi_i$  where  $1 \leq i \leq M$ . Finally the DoA is found computing all the spatial frequencies  $\mu$  that, if done the array remapping, can be mapped to  $\theta$ .

$$\mu_i = \angle(\phi_i), i = 1, \dots, d \quad (3.34)$$

$$\theta_i = \arcsin \left( -\frac{\lambda_i}{2\pi\Delta} \mu_i \right), i = 1, \dots, d \quad (3.35)$$

# Chapter 4

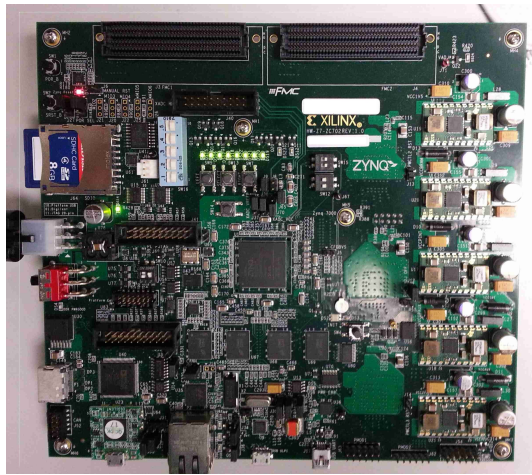
## Low cost antenna array based drone tracking device and Framework

In this Chapter was detailed the proposed low cost antenna array based drone tracking device. In Section 4.1, the steps for the hardware calibration are described. The calibration ensure all the four channels of the SDR are in phase, allowing the DoA estimation. In Section 4.2, it was presented the assembling of the components of the hardware of the proposed drone tracking device. In Section 4.3, a signal processing framework performed for DoA estimation was proposed.

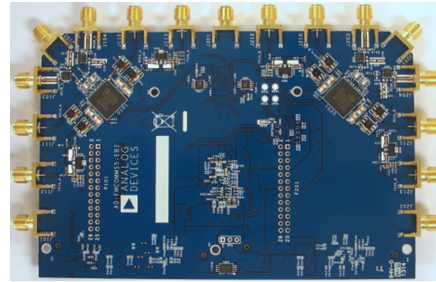
The hardware components needed to build the low cost drone tracking device are described in Table 4.1 and illustrated in the Fig. 4.1.

Table 4.1: List of hardware components used to build the low cost drone tracking device

Item	Description
Software Defined Radios	4x4 MIMO platform ADFMCOMMS5 [30] (Fig. 4.1(b)), with two AD9361 [116] Integrated Circuits (ICs) that contains 2 transmitters and two receivers each, cover 70 MHz to 6.0 GHz and have a channel bandwidth of 200 kHz to 56 MHz.
FPGA motherboard	Zynq Zc702 [31] with FPGA Mezzanine Connectors (FMC) allowing scaling and customization with daughter cards (Fig. 4.1(a)).
4 antennas	Omni-directional, Dual Band 2400–2483.5, 4900–5875 MHz, +3.7 dBi of peak gain and linear polarization. [18] (Fig. 4.1(d) and 4.2).
4 Cables	Cable Assembly SMA 305 mm long [33] (Fig. 4.1(c)).
Power division component	RF Power Splitter, Combiner, Divider with SMA Female 4-Way inputs that covers 2.4 - 6.0 GHz
Personal portable computer	The computer is used to receive all the data from FPGA in order to be processed in the Matlab Software [117]



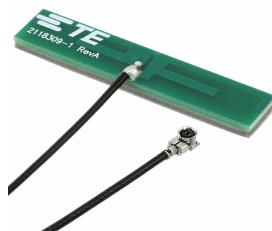
(a) uProc and FPGA motherboard [31]



(b) SDR 4x4 MIMO daughterboard [30]



(c) Cable SMA 305mm [33]



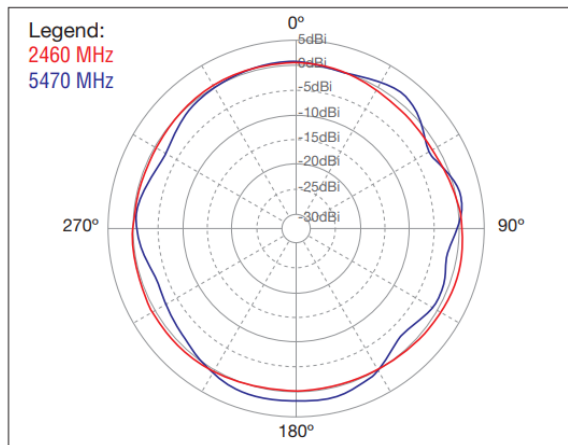
(d) Dual Band 2.4 & 5GHz [18]



(e) 4-Way Splitter 2.4-6GHz [32]

Figure 4.1: Hardware components for building the low cost drone tracking device

### Azimuth



### Elevation

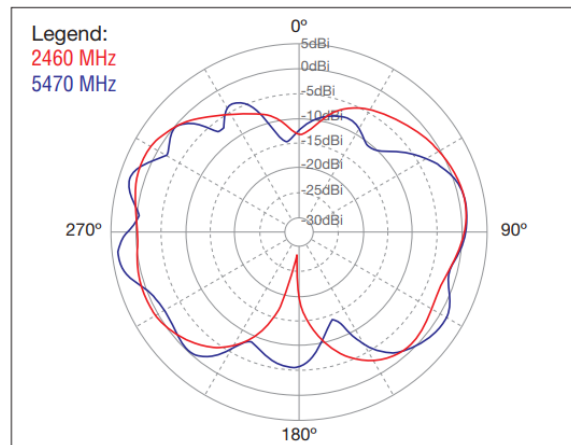


Figure 4.2: Radiation pattern for the antenna from Fig. 4.1(d). Image taken from [118]

## 4.1 Hardware assembling for the calibration

One of the big problems on practical antenna arrays is phase imbalance between the inputs of the SDR. This problem may be caused by hardware imperfection such as different lengths of the cables and tracks, multipath, different time of start on the oscillators or even by simple imperfections on manufacturing. The hardware vendor provides a software [17]

for clock synchronization of the local oscillator. However, this software does not perform phase calibration. This problem can be solved by a filter that multiplies the signal received by an exponential of the negated phase error. This phase error is obtained measuring the difference of phase between the inputs of an arrived signal that is sent from a TX output, coming through a power divider with four output signals with the same power and four cables of equal length. The mathematical approach will be explained in Subsection 4.3.1.

In order to perform the phase calibration, first the hardware components are assembled according to Fig. 4.3. Note that the SDR transmits a signal from one channel and receives it in four channels that should be calibrated, such that all receive channels are in phase.

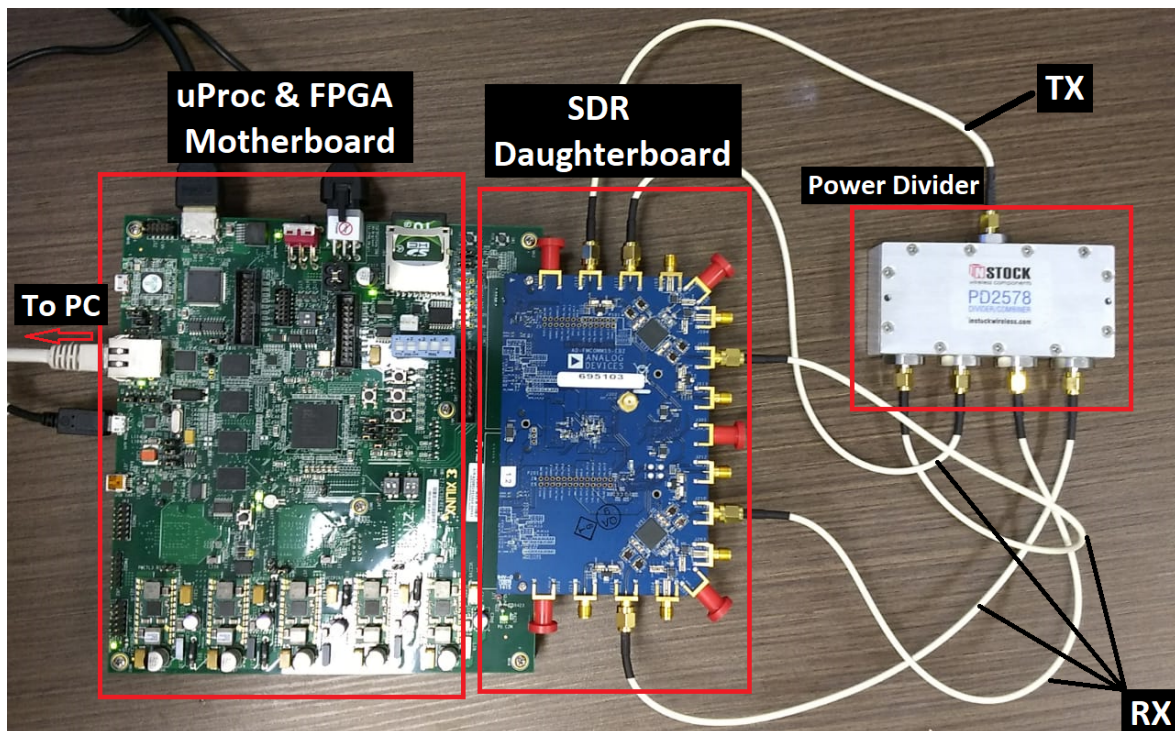


Figure 4.3: Assembled components for the hardware calibration of four receive channels. The components are a microprocessor (uProc) and FPGA motherboard, a SDR, a power divider and cables.

As shown in Fig. 4.3, the SDR [30] with two AD9361 [116] is connected to a microprocessor and FPGA motherboard [31], that configures the SDR and transmit the SDR data to PC through the UTP cable. Note that the cables [33] for calibration should have the same length. Moreover, a power divider component [32] is included in order to lead the signal to the four receive channels at the same time, and to reduce the power of the transmitted signal to avoid damaging.

## 4.2 Hardware assembling for the drone tracking measurement campaign

After the hardware has been calibrated, the next step is to assemble it in order to perform the measurements. The four elements omni-directional antenna array is connected to the calibrated hardware composed by the FPGA motherboard and SDR daughterboard according to Fig. 4.4. Each antenna is dual band (from 2400 MHz to 2483.5 MHz and from 4900 MHz to 5875 MHz) [18] and has linear polarization with 3.7 dBi of gain. The space  $\Delta$  between two consecutive antennas is equal to 59.9 mm.

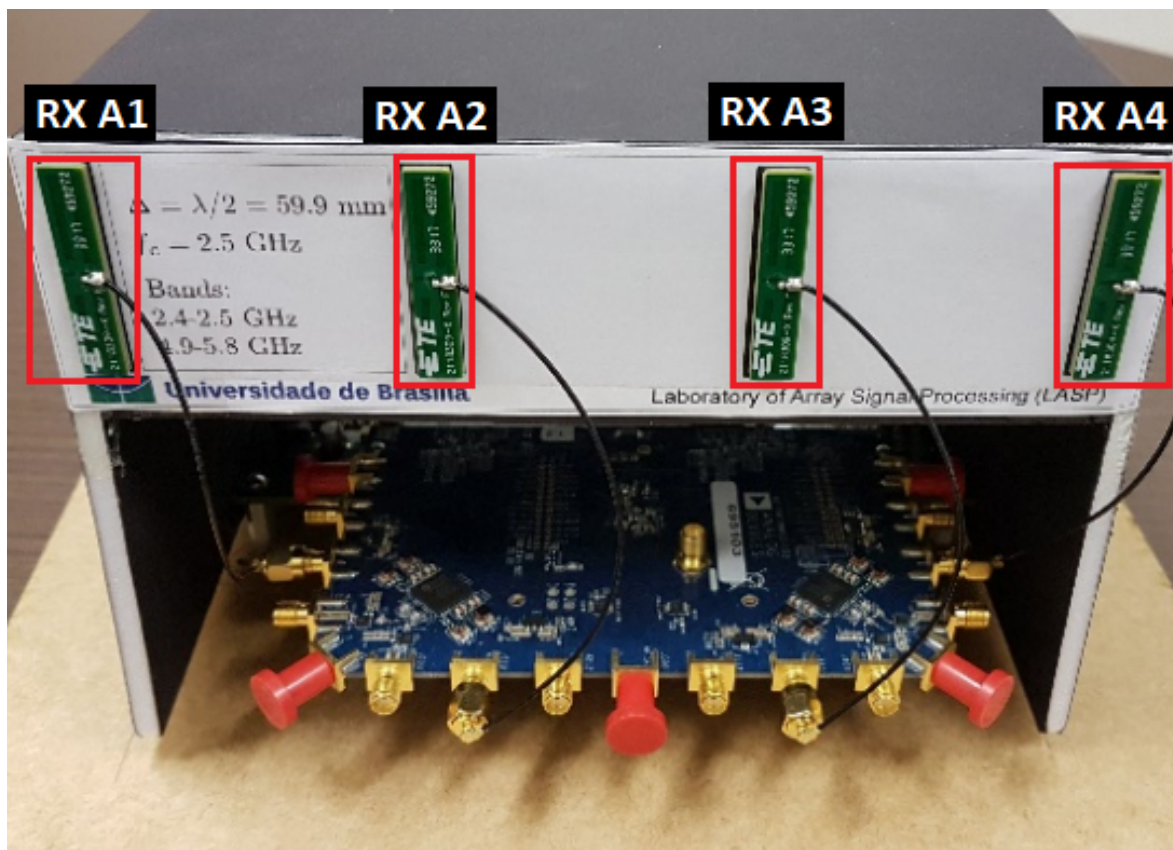


Figure 4.4: Proposed low cost antenna array based drone tracking device with 4 element ULA and a 4 x 4 MIMO SDR

## 4.3 Signal Processing Framework structure

This section is divided in three subsections. Subsection 4.3.1 explains the mathematical approach of the hardware calibration of Section 4.1. Then, Subsection 4.3.2 draws the importance of the filtering. In Subsection 4.3.3 a sample selection approach for DoA estimation by automatic phase deviation detection is proposed, whereas in Subsection 4.3.4 it is presented the DoA estimation framework exploiting pre-processing techniques, model order selection schemes and DoA estimation approaches. Fig. 4.5 depicts the flowchart of proposed signal

processing framework solution for DoA estimation.

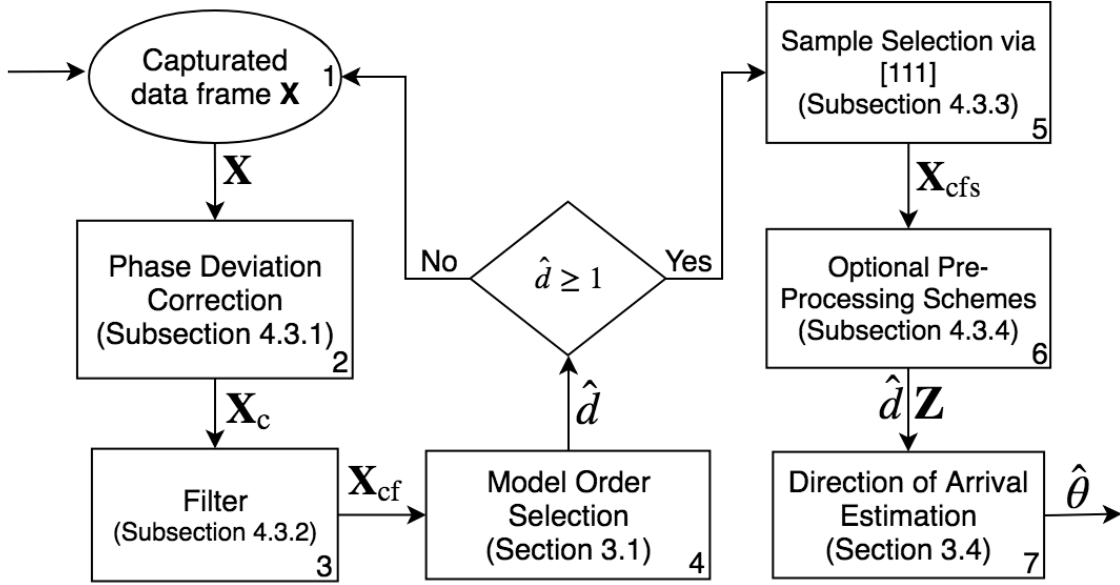


Figure 4.5: Flowchart of proposed framework solution for DoA estimation

As shown in Box 2 of Fig. 4.5, the phase deviation correction proposed on Subsection 4.3.1 returns a matrix  $\mathbf{X}_c$  that is used in the filter box from Subsection 4.3.2, in order to get an improved data. The returned  $\mathbf{X}_{cf}$  is now used in sample selection scheme of Subsection 4.3.3, such as it returns  $\mathbf{X}_{cfs}$  that is used for pre-processing schemes and DoA estimation in Subsection 4.3.4.

### 4.3.1 Phase Deviation Correction

As explained in Section 4.1, several problems may cause phase imbalance. Here it is presented the mathematical approach in order to find the compensation vector such that it corrects the phase shift.

First, the phase of the elements of the matrix  $\mathbf{X}$  is extracted by defining

$$\phi_{i,j} = \angle x(i,j) = \arctan \left( \frac{\text{Im}\{x(i,j)\}}{\text{Re}\{x(i,j)\}} \right), \quad (4.1)$$

where  $x(i,j)$  is the element in position  $i, j$  of the measured matrix  $\mathbf{X}$ . The operators  $\angle$ ,  $\text{Im}\{\cdot\}$  and  $\text{Re}\{\cdot\}$  stand for the phase operator, the imaginary part of a complex number and the real part of a complex number, respectively.

In order to compute the phase shift between two channels, the following expression is applied

$$\omega(m, :) = \Phi(m, :) - \Phi(i, :) \in \mathbb{C}^{1 \times N}, \quad (4.2)$$

where  $\Phi$  stands for the matrix with the phases given by (4.1),  $i$  indicates the reference channel and  $m$  varies from 1 to  $M$ . Since the vector  $\omega(m, :)$  is the  $m$ -th row of matrix  $\Omega$ , in case



$m = i$ , the  $i$ -th row of  $\Omega$  is filled with zeros. Finally, since the phase difference may slightly vary for different samples in the same row of  $\Omega$  due to the thermal noise, the arithmetic mean of the elements of each row of  $\Omega$  is computed, obtaining the vector  $\bar{\omega} \in \mathbb{C}^{M \times 1}$  and its  $m$ -th element is given by

$$\bar{\omega}(m) = \frac{1}{N} \sum_{n=1}^N \Omega(m, n). \quad (4.3)$$

Hence, in order to compensate the phase shift between two different channels, the vector  $\mathbf{c} \in \mathbb{C}^{M \times 1}$  is computed, whose  $m$ -th element is given by

$$c(m) = e^{-j\bar{\omega}(m)}. \quad (4.4)$$

Note that the compensation vector  $\mathbf{c}$  is computed only once for the system initialization. The calibrated outputs of the antenna array are given by the following expression

$$\mathbf{X}_c = \text{diag}\{\mathbf{c}\}\mathbf{X}, \quad (4.5)$$

where the operator  $\text{diag}\{\cdot\}$  transforms its argument vector into the main diagonal of a diagonal matrix.

### 4.3.2 Band-Rejection Filter

In Chapter 2, the noise is assumed to be Complex-Valued Circularly Symmetric Gaussian and identically and independently distributed (i.i.d.). The EFT relies on these properties of the noise. Due to extremely low values of the  $P_{fa}$  presented in Appendix A, the noise behavior is analyzed.

According to Fig. 4.6, the Power Spectrum Density (PSD) is not flat, implying that the noise is time correlated. Note that the hardware inserts a specific noise at 1 MHz. Therefore, and according to third box of Flowchart 4.5 to remove this specific noise a band-rejection filter should be applied at that frequency.

### 4.3.3 Selection of samples and Matrix $\mathbf{X}$

In order to avoid the unnecessary computational load, when there is no signal present the framework starts a new capture without execute the pre-processing and DoA algorithms. This selection is made by checking the Model Order given by the MOS schemes as presented in Fig. 4.5. Before starting the processing by the pre-processing and DoA algorithms, the authenticity of the data must also be checked. Therefore, if exists a signal present, the captured matrix  $\mathbf{X}$  is passed to the sampling selection that is explained in this subsection.

As exemplified  $\Phi$  in Fig. 4.7, it is empirically observed that the hardware causes phase

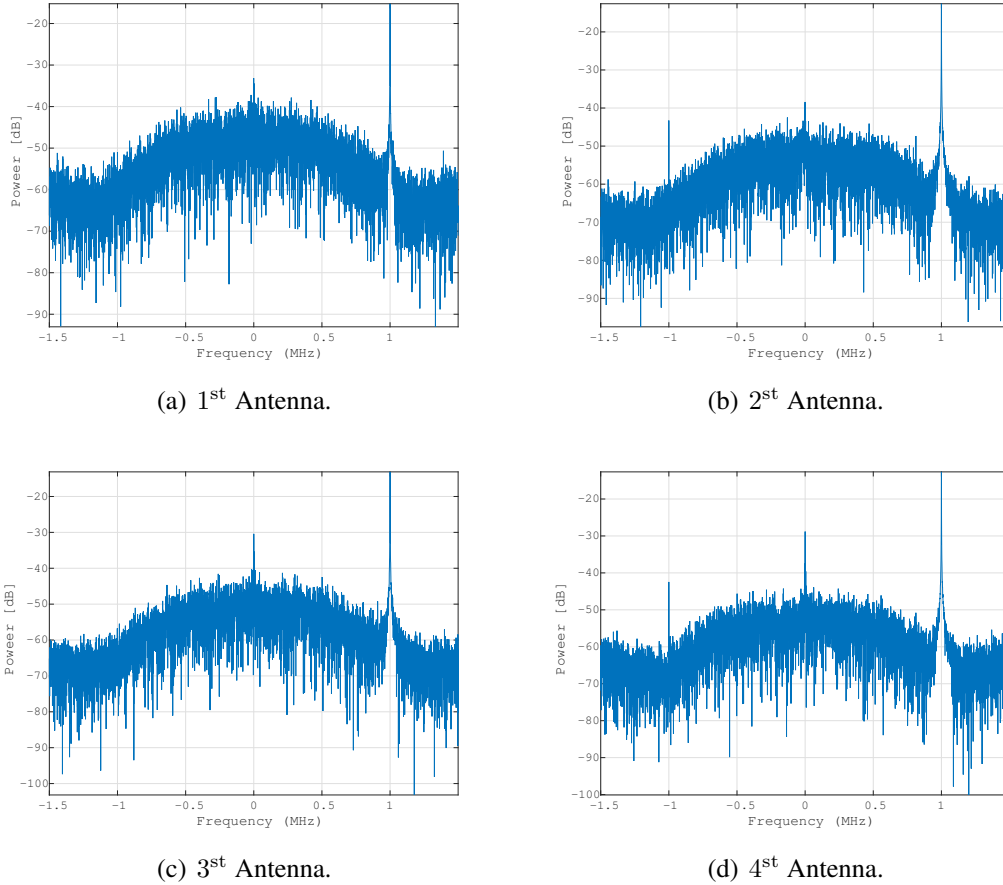


Figure 4.6: Power Density Spectrum of the noise only case for each antenna.

deviations on the samples in random time instants. Therefore, an approach to select the samples with phase deviations for the DoA estimation is proposed.

Note that the phase compensation proposed in Subsection 4.3.1 has been applied on the samples, whose phases are depicted in Fig. 4.7. Furthermore, note that there are significant deviations that can degrade the DoA estimation process. As shown in Fig. 4.8, such ripples can be better visualized by computing the phase difference in the time dimension according to the following expression

$$\gamma(m, i) = (\phi(m, i + 1) - \phi(m, i))^2, \quad (4.6)$$

where  $\gamma(m, i)$  is the value containing the quadratic difference of two consecutive time samples  $i$  and  $i + 1$  of the  $m$ -th channel, and  $\phi(m, i)$  is the element in position  $m, i$  of the matrix  $\Phi$  from (4.1).

By detecting the peaks in Fig. 4.8, it is possible identify which samples should be removed. For this task is used the approach proposed in [19], which returns the value of the threshold. Therefore, the samples whose phase difference are greater than the threshold are

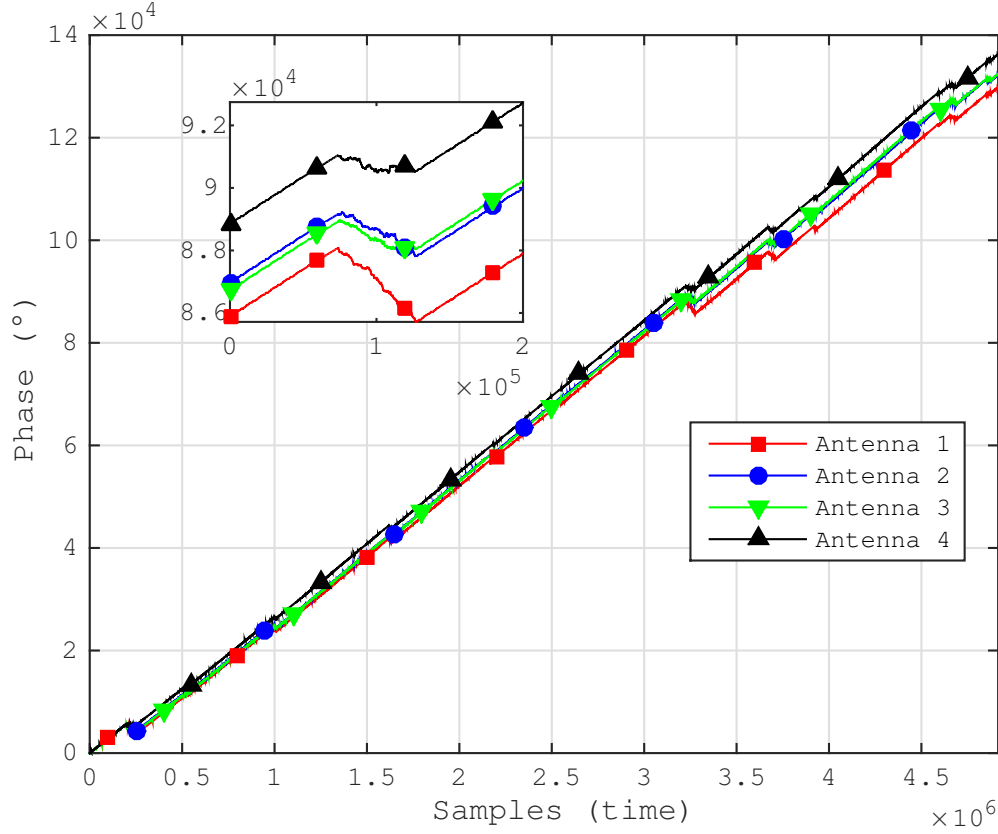


Figure 4.7: Phase of the received data in each antenna. An example of phase deviation region is highlighted in the zoom area.

removed. The result after the samples removed is presented in the following equation

$$\mathbf{X}_{\text{cfs}} = [\mathbf{X}_{\text{cf}}(:, 1 : N_1) | \mathbf{X}_{\text{cf}}(:, N_2 : N_3) | \dots | \mathbf{X}_{\text{cf}}(:, N_{T-1} : N_T)], \quad (4.7)$$

where  $\mathbf{X}_{\text{cfs}}$  is the matrix with the selected samples. Note that  $N_T = N$  and the values of  $N_t$ , for  $t = 1, \dots, T$ , are found by comparing the phase difference values with the threshold in Fig. 4.8.

#### 4.3.4 MOS, Pre-processing and DoA Estimation

According to box 1 Fig. 4.5, the matrix  $\mathbf{X}_{\text{cfs}}$  given in Subsection 4.3.3 is used now to improve the DoA estimation with pre-processing schemes. There are several DoA estimation schemes in the literature as presented in Section 3.3, such as beamforming approaches and subspace based approaches. In this framework, all the DoA methods presented in the Section 3.3 are adopted, since the redundancy brings confidence and after the pre-processing schemes the DoA methods have similar performance, as presented in Section 5.4.

The DoA estimation schemes assume that the model order  $d$  is known. In practice, model order selection techniques should be applied to estimate the model order  $d$  as depicted in Fig.

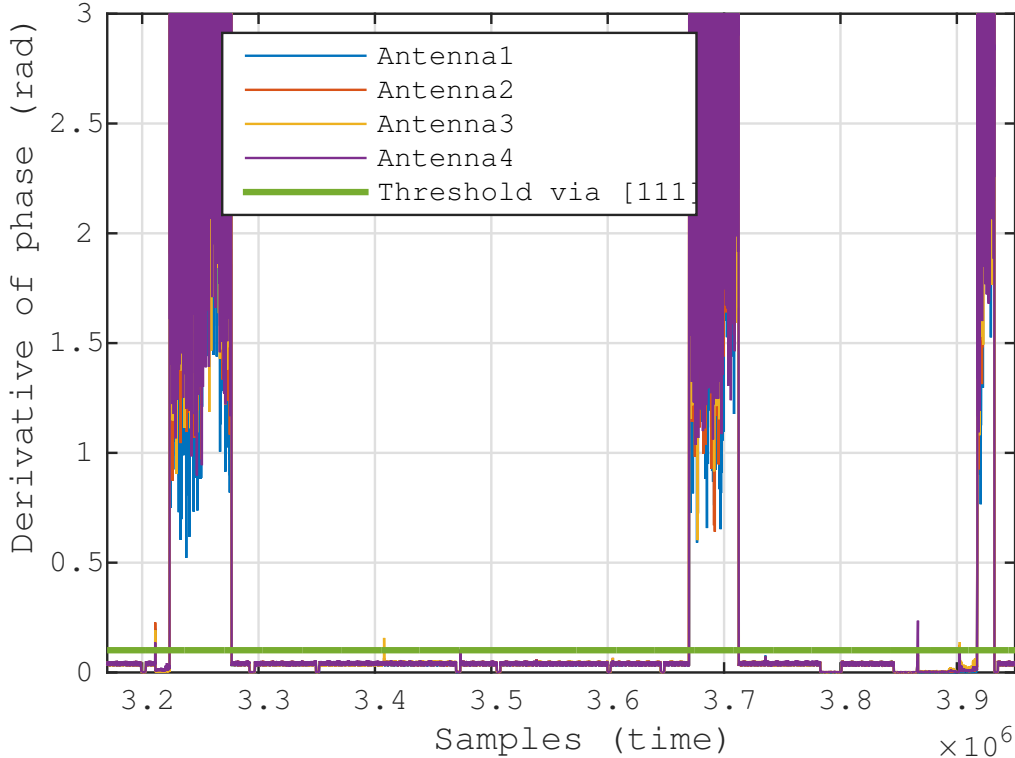


Figure 4.8: Phase difference between consecutive samples from Fig. 4.7.

4.5.

In the box 4 from Fig. 4.5, the Exponential Fitting Test (EFT) [20, 6] was adopted as the model order selection scheme. The EFT has the deflation properties that allows to find suitable thresholds as a function of the Probability of False Alarm ( $P_{fa}$ ). By exploiting the deflation property and by finding suitable thresholds, the EFT has been the only scheme in the literature to estimate  $d = 1$  in the presence of a strong LOS signal and  $d = 0$ , in the noise-only measurements. Several schemes were compared in the literature such as Akaike Information Criterion (AIC) [1], Efficient Detection Criterion (EDC) [3], Minimum Description Length (MDL) [2], Stein's unbiased risk estimate (SURE) [4], RADOI [5], ESTimation ERror (ESTER) [7] and Subspace-based Automatic Model Order Selection (SAMOS) [8]. The M-EFT [20, 6, 21] has been also suitable, but a smaller  $P_{fa}$  was required to find the thresholds. The calculus of the thresholds of the EFT requires an extremely low  $P_{fa}$ . Such calculus is computationally prohibitive. Therefore, in Appendix A it is proposed an extrapolation algorithm to compute such thresholds. Note that our proposed extrapolation algorithm has been applied in [22, 23, 24], although no details are provided in these works. Note that the reason for extremely low  $P_{fa}$  may be related to the colored noise behavior presented in Subsection 4.3.2.

In order to further improve the accuracy of DoA estimation, pre-processing schemes can be applied beforehand. In this work the Spatial Smoothing (SPS) [9, 25], Forward Backward Averaging (FBA) [10, 11] and Vandermode Invariance Technique (VIT) [12] were used as

pre-processing schemes. The box 6 from Fig. 4.5 is now enlarged in Fig. 4.9 in order to best describe the pre-processing step. After that, a matrix  $\mathbf{Z}$  is returned and used by the DoA methods summarized in Section 3.3.

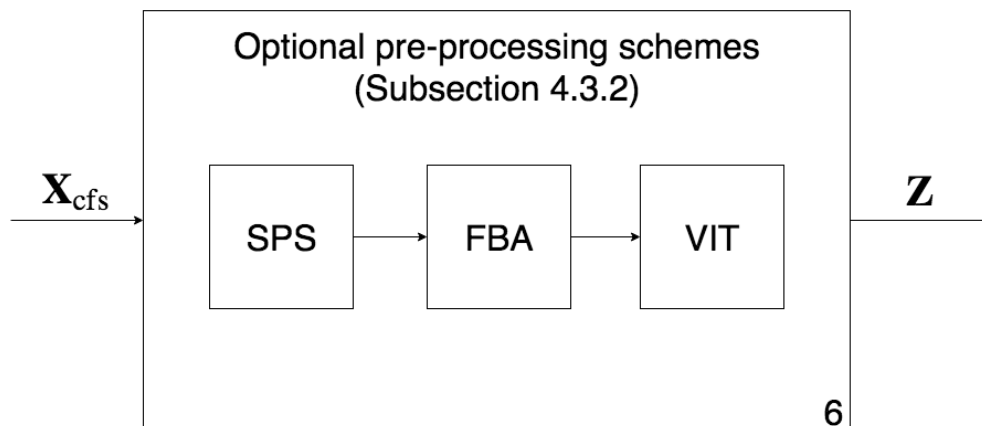


Figure 4.9: Expanded version of box 6 presented in Fig. 4.5

# Chapter 5

## Results

In this Chapter, the proposed drone tracking device with measurement campaigns in an outdoor scenario, is validated. In Section 5.1, the setup for the measurement campaign is described, while, in Section 5.2, 5.3, and 5.4, are presented the results for the filter, MOS and DoA respectively.

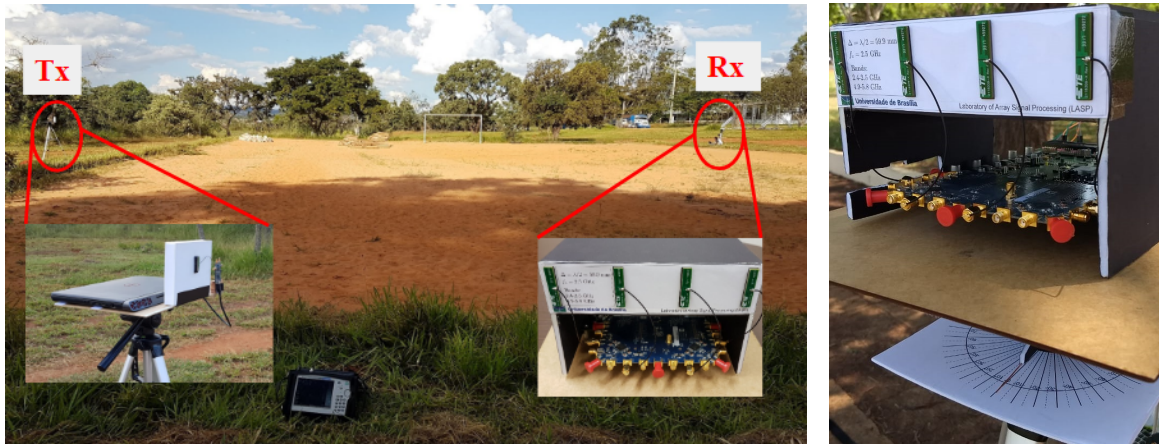
### 5.1 Experimental Setup

In Figure 5.1(a), it is depicted the outdoor scenario used for the measurement campaigns. On the right side, was placed the drone tracking device proposed in Section 4 as the receiver, while, on the left side, the transmitter is placed. The transmitter, that simulates an UAV, is a 2x2 MIMO SDR platform ASPR4 [26], with 50 MHz to 6.0 GHz, a channel bandwidth of 200 kHz to 56 MHz and max power of 10 dBm at each output port. The center frequency of both transmitter and antenna array based receiver was set at 2.48 GHz.

As shown in Figure 5.2, the distance between the transmitter and the receiver is 48 m. Both transmitter and receiver are on tripods 115 cm above the ground. Note that the red “X” in Figure 5.2 is the location from where the photo in Figure 5.1(a) has been taken.

The transmitter was setup using a MSK message signal to verify that the device functions properly. The transmitted symbols are pseudo random sequences with 1024 bits, a header 0xFFFF and a footer 0x0000. The proposed drone tracking device was setup to a 1 MHz of bandwidth, 3 MHz sampling frequency, 2.48 GHz carrier frequency, 500 kbps data rate and 5120 samples.

As shown in Figure 5.2, the transmitter is fixed and the receiver rotates from  $+90^\circ$  to  $-90^\circ$  in steps of  $10^\circ$ . Note that this step is done manually, so the estimated DoA may be biased due to inaccuracies of the operator controlling the rotation, or even printing error in the paper-based protractor presented in Figure 5.1(b).



(a) Positions of the transmitter and antenna array based receiver

(b) Assembled array with paper-based protractor

Figure 5.1: Photos taken during the measurement campaigns of the outdoor scenario.

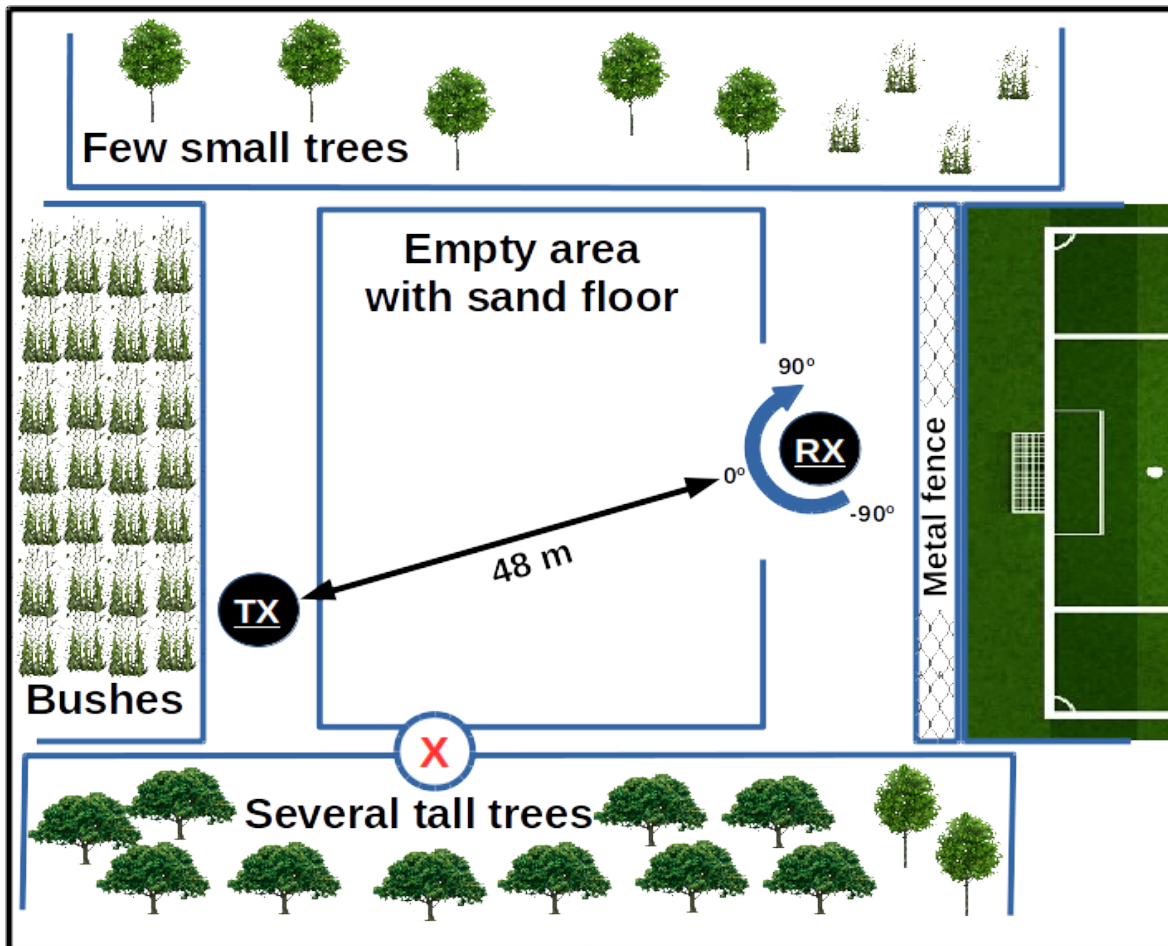
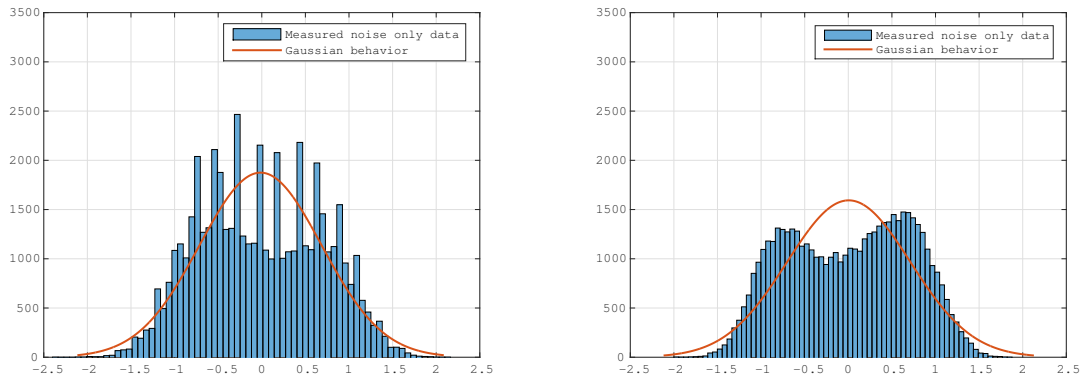


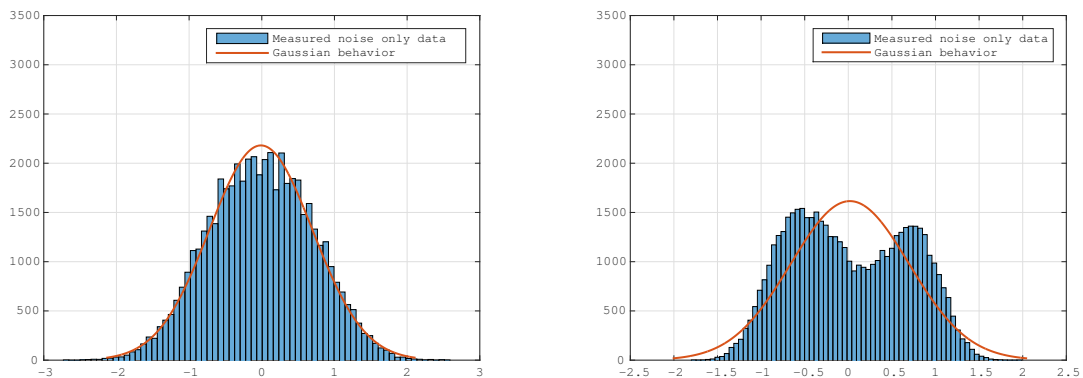
Figure 5.2: Top view of the outdoor scenario for the measurement campaigns including the positions of the transmitter and of the antenna array based receiver

## 5.2 Band-Reject Filter Results

As presented in the Subsection 4.3.2, it is important to filter the received signal in order to obtain a Gaussian behavior. In Figs. 5.3 and 5.4, it is depicted the histogram for antenna 1, 2, 3 and 4, with and without the filtering. The improvement with the filter is noted with the Gaussian behavior presented in Fig. 5.4 with the data after filtering.



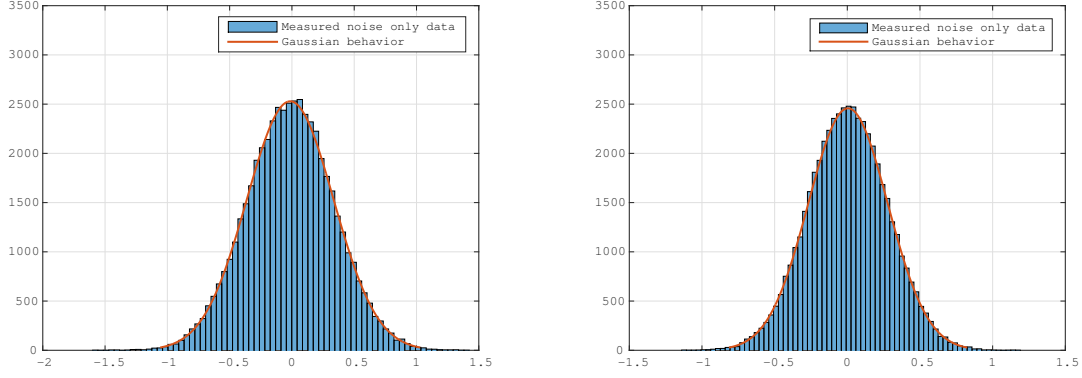
(a) 1<sup>st</sup> Antenna with 70 bins, mean =  $-0.1035$  and Standard deviation =  $0.7018$ .  
(b) 2<sup>st</sup> Antenna with 70 bins, mean =  $-0.0494$  and Standard deviation =  $0.6322$ .



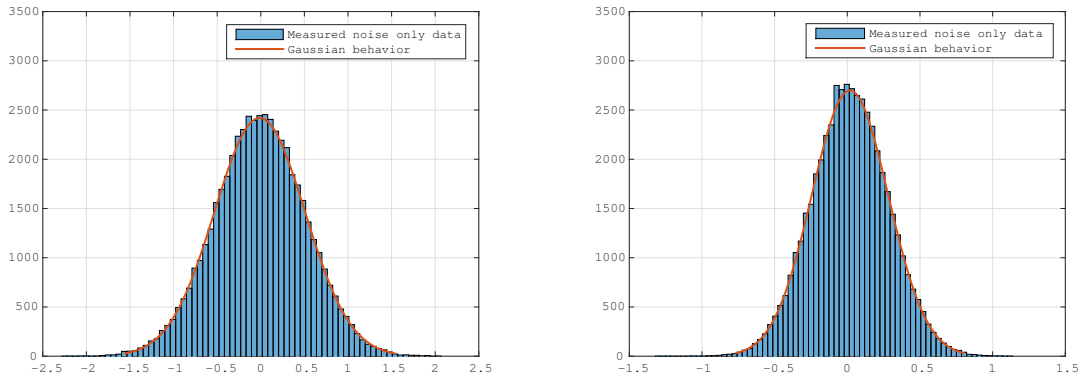
(c) 3<sup>st</sup> Antenna with 70 bins, mean =  $0.1162$  and Standard deviation =  $0.7377$ .  
(d) 4<sup>st</sup> Antenna with 70 bins, mean =  $0.0845$  and Standard deviation =  $0.6836$ .

Figure 5.3: Histogram of the noise only case for each antenna.





(a) 1<sup>st</sup> Antenna with 70 bins, mean =  $-0.1035$  and (b) 2<sup>st</sup> Antenna with 70 bins, mean =  $-0.0494$  and Standard deviation =  $0.7018$ .



(c) 3<sup>st</sup> Antenna with 70 bins, mean =  $0.1162$  and (d) 4<sup>st</sup> Antenna with 70 bins, mean =  $0.0845$  and Standard deviation =  $0.7377$ .

Figure 5.4: Histogram of the filtered noise only case for each antenna.

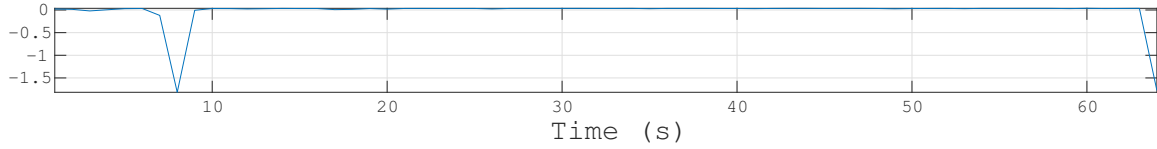
### 5.3 MOS Results

The Model Order Selection (MOS) schemes are very important on High Resolution Signal Processing as well in our proposed device. As explained in Subsection 4.3.3 and 4.3.4 the MOS is used for DoA schemes and to select a data frame that would be processed in order to avoid unnecessary data processing if the signal source is not present. The third block of Flowchart from Fig. 4.5 give the matrix  $\mathbf{X}_{cf}$  which is used by MOS schemes.

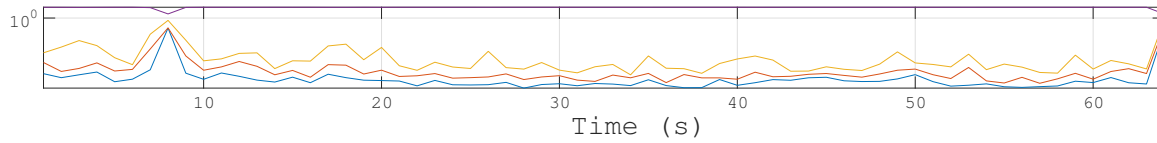
Two experiments to test the MOS schemes were done. The first experiment used a transmitter 2x2 MIMO SDR platform ASPR4 [26] with max power of 10 dBm, which transmit a known signal continuously. In the other hand, the second experiment try to be more realistic and, as presented in Table 1.1, a signal transmitted by an UAV uses WiFi to communicate with the controller and can be simulated by any router, was used [27]. Other advantage of the second experiment is the noise case only, with no sources. These experiments used only one transmitter, so the model order must be always one when a signal is present.

In order to become easier to see, the results is divided into two images for each exper-

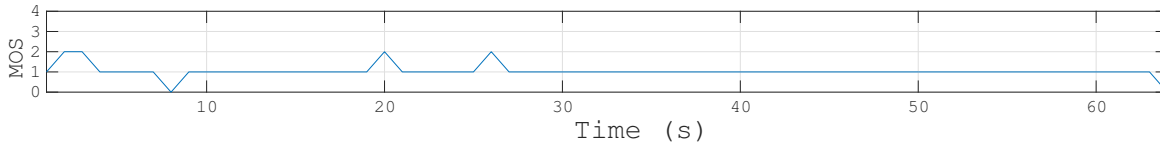
iment, the first experiment campaign is presented in Fig. 5.5 and the second experiment is presented in Fig. 5.6, with the behavior of the methods presented in Section 3.1. Note that the first two figures contain the power and eigenvalues, in addition to the figures with the MOS results. With these two images it is possible to see the behavior over time and compare when a signal is received and when there is only noise.



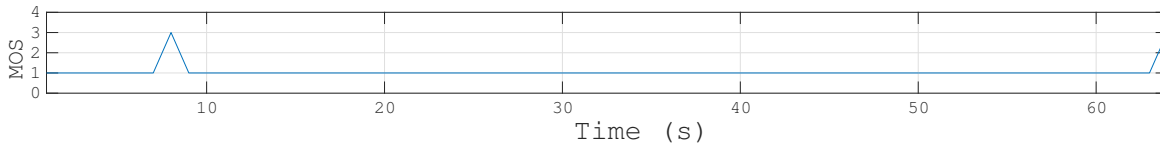
(a) Average normalized power (dB) of the 4 antennas from captured data on outdoor campaign



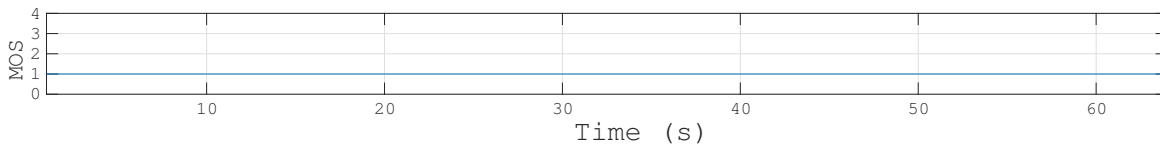
(b) Four Eigen Values (dB) from captured data on outdoor campaign



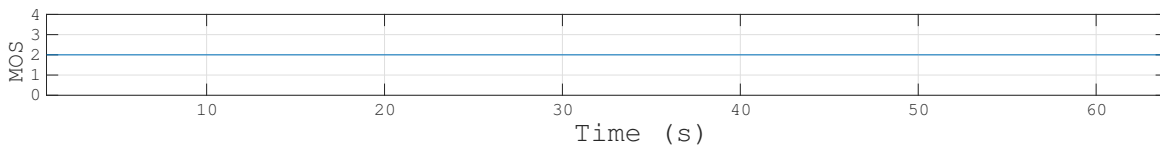
(c) EFT [6] using thresholds from Appendix A



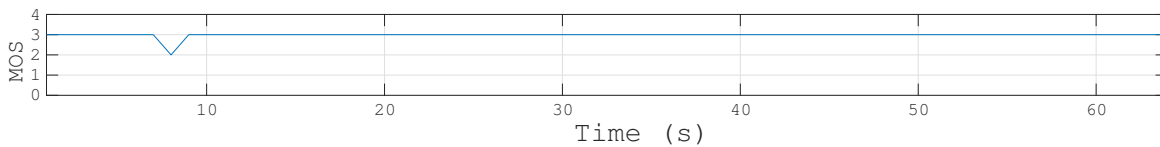
(d) Radoi-EDC



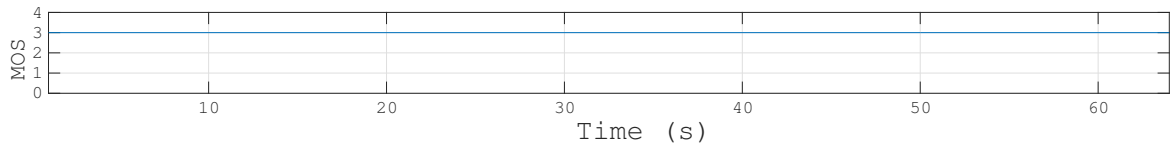
(e) SAMOS [8]



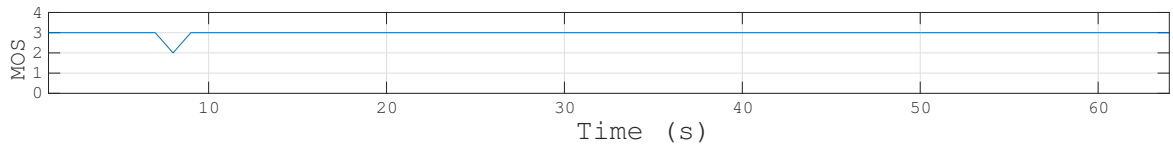
(f) Radoi [5]



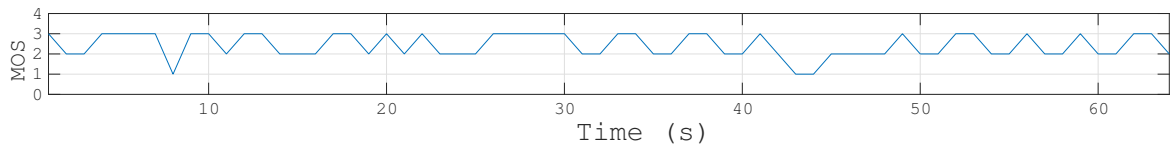
(g) EDC [3]



(h) Akaike [1]

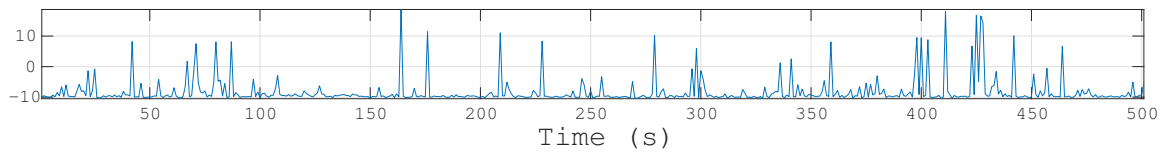


(i) MDL [2]

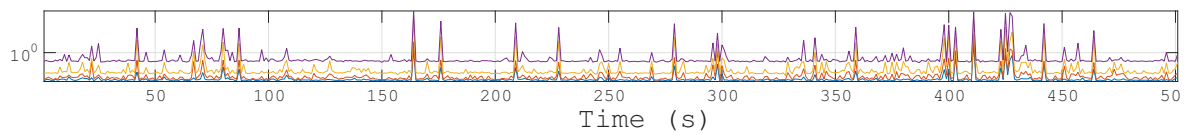


(j) Modified EFT [21]

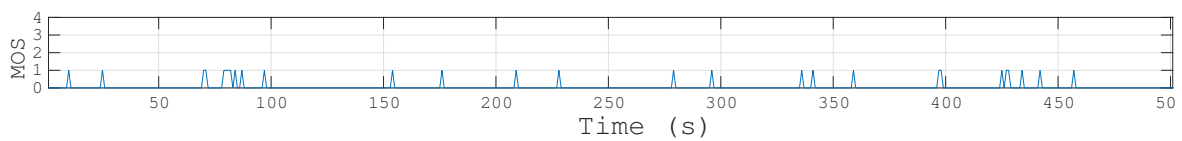
Figure 5.5: First experiment to calculate the MOS by schemes from 3.1 using an ASRP4 [26] as transmitter.



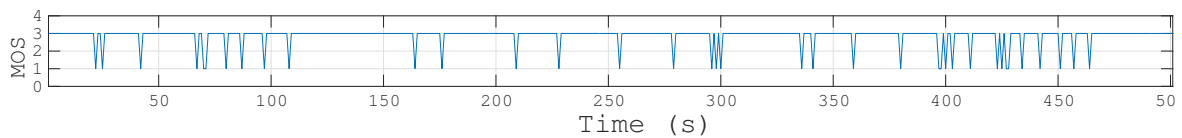
(a) Average normalized power (dB) of the 4 antennas from captured data on outdoor campaigning



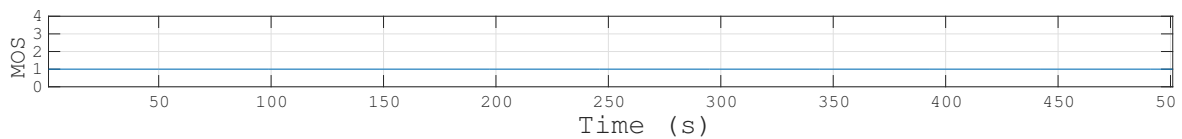
(b) Four eigen values from captured data on outdoor campaigning



(c) EFT [6] using thresholds from Appendix A



(d) Radoi-EDC



(e) SAMOS [8]

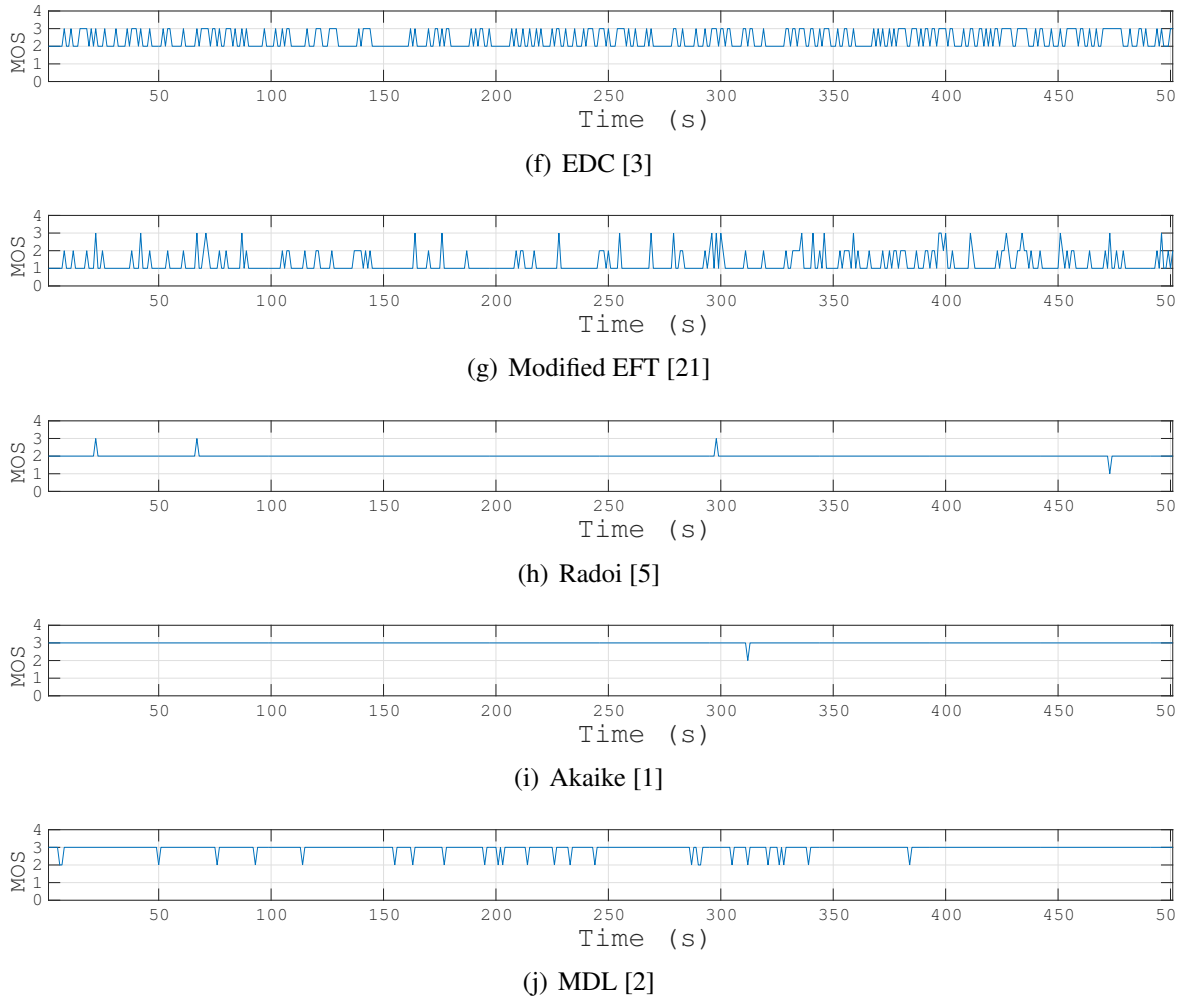


Figure 5.6: Second experiment to calculate the MOS by schemes from 3.1 using a router [27] as transmitter.

Except for SAMOS [8] and ESTER [7], the  $\mathbf{X}_{cf}$  has 5120 samples. The computational processing of Singular Value Decomposition (SVD) is very prohibitive for large matrices, therefore was used a matrix  $\mathbf{X}_{cf} \in \mathbb{C}^{4 \times 1000}$  matrix for SAMOS and ESTER.

Despite some minor errors, the EFT using the proposed thresholds from Appendix A has the best performance based on the fact that the recognized number of sources was one. The Radoi with discriminant approach also stands out at the point where in presence of a signal it recognized the best amount of frames. However, as presented in the Fig. 5.6(d) of the second experiment, in the noisy case only it detects the wrong number of sources.

## 5.4 DoA Results

This Section shows the performance of the DoA schemes shown in Section 3.3 using the ASRP4 [26] as transmitter. During the measurement campaign, the achieved Bit Error Rate (BER) was  $10^{-4}$ .

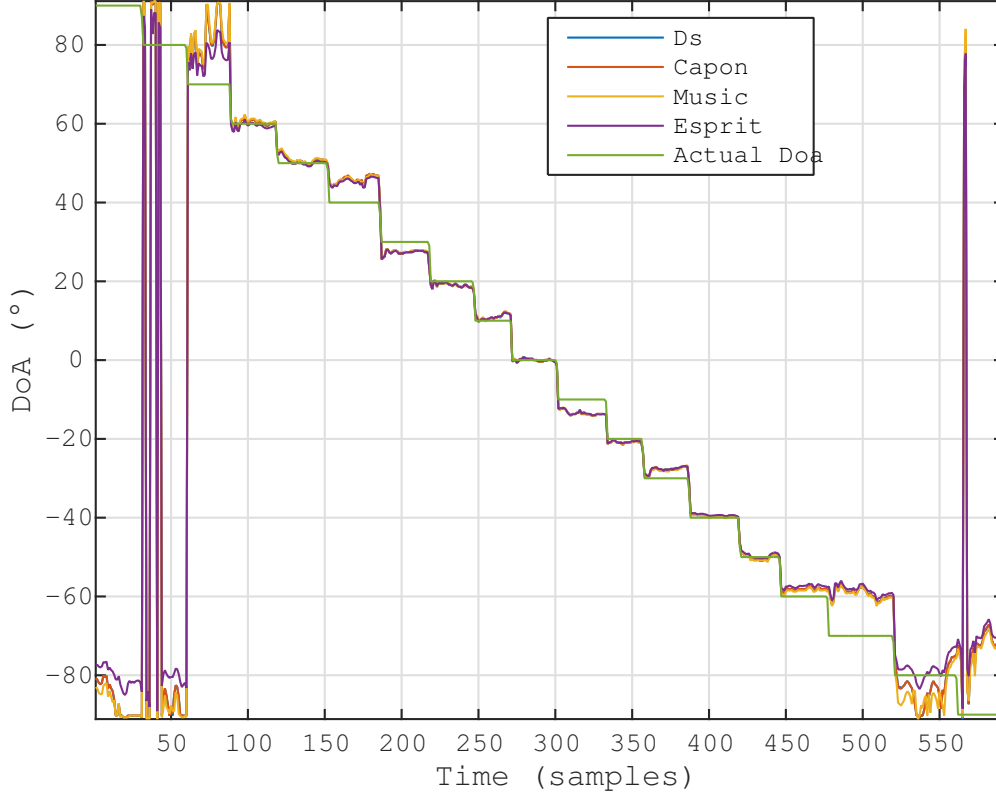


Figure 5.7: Comparison between the DoA estimation schemes by varying the DoA from  $+90^\circ$  to  $-90^\circ$  with steps of  $10^\circ$ .

Fig. 5.7 shows the DoA calculated by rotating the base array over the time. Note that our proposed device works properly for a DoA ranging from  $-60^\circ$  to  $60^\circ$ . The RMSE, given by Eq. 5.1, of DoA methods combined with pre-processing schemes is shown in Fig. 5.8. The worst algorithm DoA error was about  $6^\circ$  on this range of  $-60^\circ$  to  $+60^\circ$ . The equation for RMSE is given by

$$\text{RMSE}(\theta_1) = \sqrt{\frac{1}{Q} \sum_{q=1}^Q (\theta_1^{(q)} - \hat{\theta}_1^{(q)})^2} \quad (5.1)$$

where  $q$  stands for one of a total of  $Q$  realizations for each  $10^\circ$  step of the measurement campaign. In each  $10^\circ$  step, many frames of  $N = 5120$  snapshots are acquired for each channel, giving us the matrix  $\mathbf{X} \in \mathbb{C}^{4 \times 5120}$ .

The evolution of the results from the range of  $-60^\circ$  to  $+60^\circ$  is presented into Tables 5.1, 5.2, 5.3, 5.4, 5.5 and 5.6, which present the results increasing with the use of the pre-processing schemes.

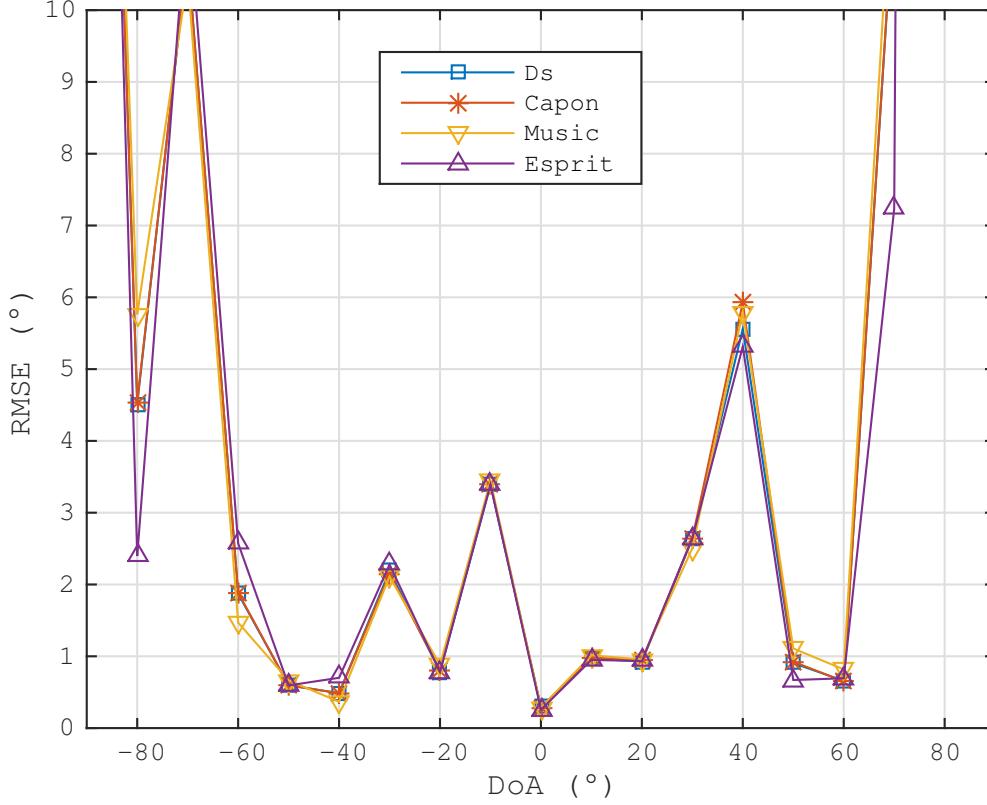


Figure 5.8: RMSE comparison between the Expected DoA and the DoA estimation combined with pre-processing schemes by varying the angle from  $+90^\circ$  to  $-90^\circ$  with steps of  $10^\circ$ .

Table 5.1: RMSE for the schemes in Section 3.2 without the pre-processing schemes, using the measurements from Fig. 5.7

Algorithm	DS	CAPON	MUSIC	ESPRIT
RMSE	2.3388°	1.6696°	3.9923°	2.8080°
Variance of the RMSE	4.2826°	1.0706°	11.5493°	4.0692°

Table 5.2: RMSE for the schemes in Section 3.2 with VIT [12] pre-processing scheme, using the measurements from Fig. 5.7

Algorithm	DS	CAPON	MUSIC	ESPRIT
RMSE	2.3388°	2.0242°	2.8352°	2.9575°
Variance of the RMSE	4.2861°	1.8770°	4.8320°	5.2364°

Table 5.3: RMSE for the schemes in Section 3.2 with FBA [10, 11] pre-processing scheme, using the measurements from Fig. 5.7

Algorithm	DS	CAPON	MUSIC	ESPRIT
RMSE	2.1205°	1.6833°	4.0570°	2.4022°
Variance of the RMSE	3.7932°	1.0795°	16.7736°	3.6046°

Table 5.4: RMSE for the schemes in Section 3.2 with SPS [9, 25] pre-processing scheme, using the measurements from Fig. 5.7

Algorithm	DS	CAPON	MUSIC	ESPRIT
RMSE	1.6484°	2.4197°	1.9689°	1.8716°
Variance of the RMSE	2.3307°	2.4003°	3.6663°	1.8416°

Table 5.5: RMSE for the schemes in Section 3.2 with FBA and SPS pre-processing schemes, using the measurements from Fig. 5.7

Algorithm	DS	CAPON	MUSIC	ESPRIT
RMSE	1.6548°	1.6745°	1.6813°	1.8776°
Variance of the RMSE	2.3628°	2.5452°	2.4180°	1.8904°

Table 5.6: RMSE for the schemes in Section 3.2 with FBA, SPS and VIT pre-processing schemes, using the measurements from Fig. 5.7

Algorithm	DS	CAPON	MUSIC	ESPRIT
RMSE	1.6361°	1.6676°	1.6475°	1.6757°
Variance of the RMSE	2.2671°	2.5168°	2.3600°	2.1913°

Finally, the performance evolution result RMSE presented in tables 5.1, 5.2, 5.3, 5.4, 5.5 and 5.6 is now drawn in Fig. 5.9. These results show the importance of preprocessing schemes, which proves that it is better to use all of them in combination.

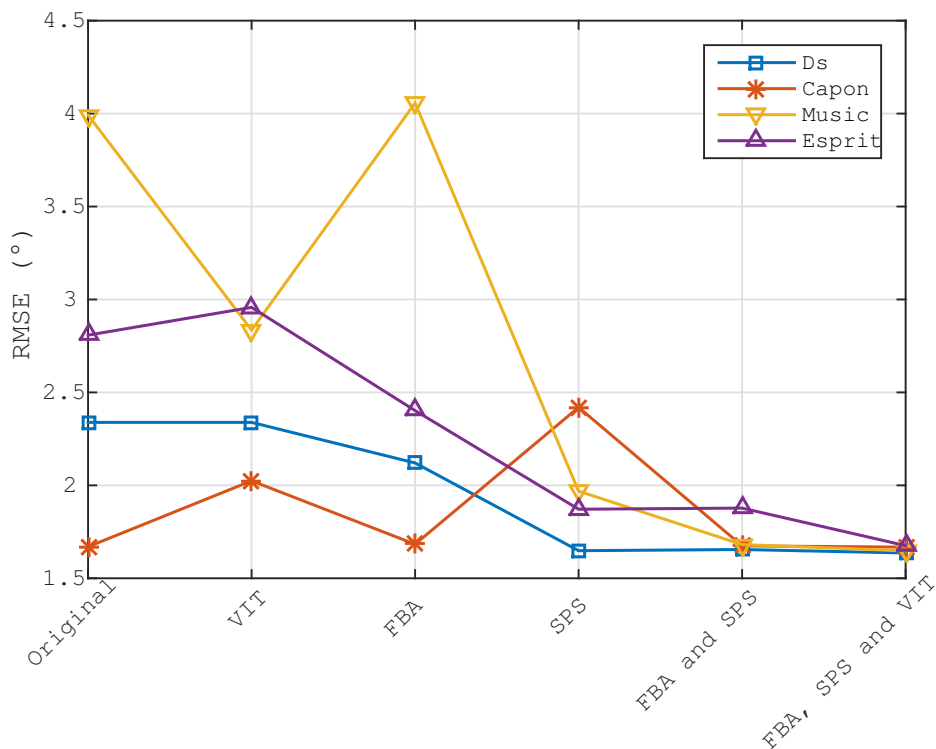


Figure 5.9: Comparison of performance between the RMSE results presented in tables 5.1, 5.2, 5.3, 5.4, 5.5, 5.6

As shown in Table 5.7, the total cost of the proposed drone tracking solution is US\$ 2.222, while the solutions in [28] and [29] cost US\$ 226.000 and US\$ 120.000, respectively. Therefore, our proposed off-the-shelf solution costs less than 2 % of the commercial solutions in [28] and [29].

Table 5.7: Price Table for the Hardware of the Proposed Drone Tracker Device

Hardware	Cost (US\$)
AD-FMCOMMS5-EBZ-ND [30]	1080
4 × Dual-Band Antenna 2.4 & 5GHz [18]	11
ZYNQ 7000 Zc702 [31]	999
Power Divider 2.4-6GHz 30Watts RoHS IP67 [32]	109
5 × cable 305mm HPP100 SMA [33]	23
<b>Total</b>	<b>2222</b>



# Chapter 6

## Conclusion

Over the last years, Unmanned Aerial Vehicles (UAVs) have been a major concern of airspace control bodies and military due to possible terrorist attacks and illegal activities. Therefore, recently police forces and security companies have drawn their attention to drone tracking devices in order to provide the safeness of citizens and clients. Consequently, applications of direction of arrival (DoA) techniques have dramatically increased in various areas. In this sense, the development of low cost devices for drone tracking is fundamental to fit such demands.

In this thesis, was proposed a low cost antenna array based drone tracking device for outdoor environments. The proposed solution is divided into hardware and software parts. The hardware of the proposed device is based on off-the-shelf components such as an omnidirectional antenna array, a power division component, four SMA cables, a 4 channel SDR platform with 70 MHz to 6.0 GHz, a FPGA motherboard and a laptop. The software part includes state-of-the-art algorithms for model order selection (MOS), pre-processing and DoA estimation. The performance of the proposed low cost solution was evaluated in outdoor scenarios. According to our measurement campaigns, it is shown that, when the transmitter is in the front fire position, i.e. with a DoA ranging from  $-60^\circ$  to  $60^\circ$ , the maximum and the average DoA errors are  $6^\circ$  and  $1,6^\circ$ , respectively. Our proposed off-the-shelf solution costs less than 2 % of commercial solutions in [28] and [29].

This work also makes a comparative approach between several state-of-the-art MOS algorithms in order to choose the method with best performance, which is used in the proposed device. Despite some minor errors, the state-of-the-art EFT [6] algorithm, using the proposed thresholds from Appendix A, had the best performance and was used for MOS. Additionally, presents individual results of improvement brought by each pre-processing algorithm and its influence on the accuracy of the DoA estimation. It was proved that the DoA methods have a better accuracy with all the pre-processing schemes such as FBA [10, 11], SPS [9] and VIT [12], used in combination with each other.

One of the big problems on practical antenna arrays is phase imbalance between the in-

puts of the SDR. The presented calibration process aims to solve this problem. Due to minor random errors caused by the hardware, was also included others specific pre-processing steps in order to remove the data disturbed, the colored noise and consequently increase the DoA accuracy.

The DoA estimation used the Delay and Sum [13], CAPON [14], MUSIC [15] and ESPRIT [16] algorithms, and their accuracy was measured. The DoA methods basically had similar performance, however, ESPRIT spends more computational load. Without pre-processing, MUSIC was the one with the highest variance and the worst measured error.

It was also proved that, it is highly possible to detect the direction of an UAV with an array of antennas built with low cost hardware and without concern about complex issues such as mutual coupling or calibration in environments with optimal conditions. It is clear that some improvements can be made, such as to use a more realistic noise model given the low  $Pf_a$ , and to use some electronic instrument to allow bias reduction, as shown in Section 5.1. However, for our motivation, UAVs can be detected with good accuracy in the range of -60 to +60 degrees.

# Bibliography

- [1] H. Akaike, “Information Theory as an Extension of the Maximum Likelihood,” in *Proc. 2nd Int. Symp. on Information Theory*. Proceeding of International Symposium on Information Theory, 1973, pp. 267–281.
- [2] J. Rissanen, “Modeling by shortest data description,” *Automatica*, vol. 14, no. 5, pp. 465–471, 1978.
- [3] L. C. Zhao, P. R. Krishnaiah, and Z. Bai, “On detection of the number of signals in presence of white noise,” *Journal of multivariate analysis*, vol. 20, no. 1, pp. 1–25, 1986.
- [4] M. O. Ulfarsson and V. Solo, “Rank selection in noisy PCA with SURE and random matrix theory,” in *International Conference on Acoustics, Speech and Signal Processing (ICASSP)*. IEEE, 2008, pp. 3317–3320.
- [5] E. Radoi and A. Quinquis, “A new method for estimating the number of harmonic components in noise with application in high resolution radar,” *EURASIP Journal on Applied Signal Processing*, vol. 2004, pp. 1177–1188, 2004.
- [6] J. Grouffaud, P. Larzabal, and H. Clergeot, “Some properties of ordered eigenvalues of a Wishart matrix: application in detection test and model order selection,” in *International Conference on Acoustics, Speech, and Signal Processing (ICASSP)*., vol. 5. IEEE, 1996, pp. 2463–2466.
- [7] R. Badeau, B. David, and G. Richard, “Selecting the modeling order for the ESPRIT high resolution method: an alternative approach,” in *International Conference on Acoustics, Speech, and Signal Processing*, vol. 2. IEEE, 2004, pp. ii–1025.
- [8] J.-M. Papy, L. De Lathauwer, and S. Van Huffel, “A shift invariance-based order-selection technique for exponential data modelling,” *IEEE signal processing letters*, vol. 14, no. 7, pp. 473–476, 2007.
- [9] J. E. Evans, J. R. Johnson, and D. F. Sun, *Application of advanced signal processing techniques to angle of arrival estimation in ATC navigation and surveillance systems*, ser. Technical report (Lincoln Laboratory). Massachusetts

- Institute of Technology, Lincoln Laboratory, 1982. [Online]. Available: <https://books.google.com.br/books?id=IOIjSwAACAAJ>
- [10] D. A. Linebarger, R. D. DeGroat, and E. M. Dowling, "Efficient direction-finding methods employing forward/backward averaging," *IEEE Transactions on Signal Processing*, vol. 42, no. 8, pp. 2136–2145, 1994.
- [11] S. U. Pillai and B. H. Kwon, "Forward/backward spatial smoothing techniques for coherent signal identification," *IEEE Transactions on Acoustics, Speech, and Signal Processing*, vol. 37, no. 1, pp. 8–15, 1989.
- [12] T. R. Kurpjuhn, M. T. Ivrlac, and J. A. Nossek, "Vandermonde Invariance Transformation," in *International Conference on Acoustics, Speech, and Signal Processing (ICASSP)*, vol. 5. IEEE, 2001, pp. 2929–2932.
- [13] B. D. Van Veen and K. M. Buckley, "Beamforming: A versatile approach to spatial filtering," *IEEE ASSP magazine*, vol. 5, no. 2, pp. 4–24, 1988.
- [14] J. Capon, "High-resolution frequency-wavenumber spectrum analysis," *Proceedings of the IEEE*, vol. 57, no. 8, pp. 1408–1418, 1969.
- [15] R. Schmidt, "Multiple emitter location and signal parameter estimation," *Transactions on Antennas and Propagation*, vol. 34, no. 3, pp. 276–280, 1986.
- [16] R. Roy and T. Kailath, "ESPRIT-estimation of signal parameters via rotational invariance techniques," *Transactions on Acoustics, speech, and signal processing*, vol. 37, no. 7, pp. 984–995, 1989.
- [17] A. Devices. (2016) FMComms5 Plugin Description. [Online]. Available: [https://wiki.analog.com/resources/tools-software/linux-software/fmcomms5\\_plugin](https://wiki.analog.com/resources/tools-software/linux-software/fmcomms5_plugin)
- [18] "Dual band WiFi, 2.4 & 5GHz, PCB." [Online]. Available: <http://www.te.com/usa-en/product-2118309-1.html>
- [19] P. F. C. Lima, R. K. Miranda, J. P. C. L. da Costa, R. Zelenovsky, Y. Yuan, and G. Del Galdo, "Low complexity blind separation technique to solve the permutation ambiguity of convolutive speech mixtures," in *10th International Conference on Signal Processing and Communication Systems (ICSPCS)*. IEEE, 2016, pp. 1–10.
- [20] A. Quinlan, J.-P. Barbot, P. Larzabal, and M. Haardt, "Model order selection for short data: An exponential fitting test (EFT)," *EURASIP Journal on Applied Signal Processing*, vol. 2007, no. 1, pp. 201–201, 2007.
- [21] J. P. C. L. da Costa, M. Haardt, F. Romer and G. Del Galdo, "Enhanced model order estimation using higher-order arrays," in *Conference Record of the Forty-First Asilomar Conference on Signals, Systems and Computers (ACSSC)*. IEEE, 2007, pp. 412–416.

- [22] J. P. C. L. da Costa, M. Haardt, F. Romer, and G. Del Galdo, "Enhanced model order estimation using higher-order arrays," in *2007 IEEE Conference Record of the Forty-First Asilomar Conference on Signals, Systems and Computers (ACSSC)*. IEEE, 2007, pp. 412–416.
- [23] J. P. C. L. da Costa, F. Roemer, M. Haardt, and R. T. de Sousa, "Multi-dimensional model order selection," *EURASIP Journal on Advances in Signal Processing*, vol. 2011, no. 1, p. 26, 2011.
- [24] J. P. C. L. da Costa, M. Haardt, and F. Romer, "Robust methods based on the HOSVD for estimating the model order in PARAFAC models," in *5th IEEE Sensor Array and Multichannel Signal Processing Workshop (SAM)*. IEEE, 2008, pp. 510–514.
- [25] T.-J. Shan, M. Wax, and T. Kailath, "On spatial smoothing for direction-of-arrival estimation of coherent signals," *IEEE Transactions on Acoustics, Speech, and Signal Processing*, vol. 33, no. 4, pp. 806–811, 1985.
- [26] "SDR Starter Kit 2x2 MIMO 50 MHz to 6 GHz PC based." [Online]. Available: <http://akashkosgi.wixsite.com/agile-solutions/sdr-starter-kit-c1a59>
- [27] "Elecom WRC-300FEBK IEEE 802.11n/g/b 300Mbps." [Online]. Available: <http://www2.elecom.co.jp.e.gj.hp.transer.com/products/WRC-300FEBK.html?>
- [28] "Robin Radar Systems BV, Elvira® Drone Detection Radar." [Online]. Available: <https://www.robinradar.com/markets/drone-detection/>
- [29] "Real-Time RF Drone/UAV and Radar Detection System." [Online]. Available: <http://www.aaronia.com/products/solutions/Aaronia-Drone-Detection-System/>
- [30] "Eval board software Defined Radio ADFMCOMMS5-EBZ-ND." [Online]. Available: <http://www.analog.com/en/design-center/evaluation-hardware-and-software/evaluation-boards-kits/eval-ad-fmcomms5-ebz.html>
- [31] "ZYNQ-7000 ZC702 Eval KIT." [Online]. Available: <https://www.xilinx.com/products/boards-and-kits/ek-z7-zc702-g.html>
- [32] "RF Power Splitter, combiner, divider - IP67, 4 Way, SMA Female, 2.4 - 6.0 GHz." [Online]. Available: [https://www.instockwireless.com/rf\\_power\\_splitter\\_combiner\\_divider\\_pd2578.htm](https://www.instockwireless.com/rf_power_splitter_combiner_divider_pd2578.htm)
- [33] "Cable assembly SMA long 305 mm." [Online]. Available: <https://www.instockwireless.com/>
- [34] R. K. Miranda, J. P. C. L. da Costa, and F. Antreich, "High accuracy and low complexity adaptive generalized Sidelobe Cancelers for colored noise scenarios," *Digital Signal Processing*, vol. 34, pp. 48–55, 2014.

- [35] R. K. Miranda, J. P. C. L. da Costa, F. Roemer, L. R. A. X. Menezes, G. Del Galdo, and A. L. F. de Almeida, “Low complexity performance assessment of a sensor array via unscented transformation,” *Digital Signal Processing*, vol. 63, pp. 190–198, 2017.
- [36] D. Neudert-Schulz, “A contribution to efficient direction finding using antenna arrays,” Ph.D. dissertation, Technische Universität Ilmenau, 2017.
- [37] M. A. M. Marinho, F. Antreich, and J. P. C. L. da Costa, “Improved array interpolation for reduced bias in DOA estimation for GNSS,” *Proc. of Institute of Navigation (ION) GNSS+*, 2014.
- [38] D. V. de Lima, J. P. C. L. da Costa, F. Antreich, R. K. Miranda, and G. Del Galdo, “High resolution Time-delay estimation via direction of arrival estimation and Khatri-Rao factorization for multipath mitigation,” in *21st International ITG Workshop on Smart Antennas (WSA 2017), Berlin, Germany*, 2017, pp. 388–395.
- [39] D. V. de Lima, J. P. C. L. da Costa, J. P. A. Maranhão, and R. T. de Sousa, “Time-delay estimation via procrustes estimation and Khatri-Rao factorization for GNSS multipath mitigation,” in *2017 11th International Conference on Signal Processing and Communication Systems (ICSPCS)*. IEEE, 2017, pp. 1–7.
- [40] D. V. de Lima, J. P. C. L. da Costa, F. Antreich, R. K. Miranda, and G. Del Galdo, “Time-Delay estimation via CPD-GEVD applied to tensor-based GNSS arrays with errors,” in *7th International Workshop on Computational Advances in Multi-Sensor Adaptive Processing (CAMSAP)*. IEEE, 2017, pp. 1–5.
- [41] F. Karimi. (2015) Hundreds of drones fly dangerously close to manned aircraft. [Online]. Available: <https://edition.cnn.com/2015/12/12/us/drone-aircraft-close-calls/>
- [42] K. Rawlinson. (2016) Drone hits plane at Heathrow airport, says pilot. [Online]. Available: <https://www.theguardian.com/uk-news/2016/apr/17/drone-plane-heathrow-airport-british-airways>
- [43] Z. Alkhalisi. (2016) Dubai deploys a 'drone hunter' to keep its airport open. [Online]. Available: <http://money.cnn.com/2016/11/04/technology/dubai-airport-drone-hunter/index.html?iid=EL>
- [44] J. Goglia. (2017) A small drone hits a commercial airliner ... and nothing happens. [Online]. Available: <https://www.forbes.com/sites/johngoglia/2017/10/19/a-small-drone-hits-a-commercial-airliner-and-nothing-happens/#78ad9a249ea1>
- [45] G. SP. (2017) Drone sobre Congonhas pode causar prejuízo de mais de R\$ 1 milhão, estima associação de empresas aéreas. [Online]. Available: <https://g1.globo.com/sao-paulo/noticia/drone-sobre-congonhas-causou-prejuizo-de-mais-de-r-1-milhao-estima-associacao.ghhtml>

- [46] BBC. (2018) Gatwick airport: Drones ground flights. [Online]. Available: <https://www.bbc.com/news/uk-england-sussex-46623754>
- [47] D. Lisboa. (2015) Drone invade arena do Corinthians. é ilegal em estádios e tem riscos. [Online]. Available: <https://esporte.uol.com.br/futebol/ultimas-noticias/2015/05/20/drone.htm?cmpid=copiaecola>
- [48] GloboEsporte.com. (2016) Torcedores colorados depredam casa após drone da “b” sobrevoar Beira-Rio. [Online]. Available: <http://globoesporte.globo.com/rs/futebol/noticia/2016/11/torcedores-colorados-depredam-casa-apos-drone-da-b-sobrevoar-beira-rio.html>
- [49] “Dronelabs LLC, DD610AR Stationary Drone Detector.” [Online]. Available: <http://dronedetector.com/stationary-unit/>
- [50] “Detect, Inc., Drone Watcher.” [Online]. Available: [www.dronewatcher.com/](http://www.dronewatcher.com/)
- [51] M.-C. Hua, C.-H. Hsu, W.-J. Liao, C.-C. Yao, T.-H. Yeh, and H.-C. Liu, “Direction-of-arrival estimator using array switching on software defined radio platform,” in *International Symposium on Antennas and Propagation (APSURSI)*. IEEE, 2011, pp. 2821–2824.
- [52] L. Kulas, “RSS-based DoA estimation using ESPAR antennas and interpolated radiation patterns,” *Antennas and Wireless Propagation Letters*, vol. 17, no. 1, pp. 25–28, 2018.
- [53] A. B. Delai and V. Y. Vu, “Digital solution for inter-vehicle localization system by means of direction-of-arrival,” in *International Symposium on Intelligent Signal Processing and Communications (ISPACS)*. IEEE, 2006, pp. 875–878.
- [54] S. Bjorklund and A. Heydarkhan, “High resolution direction of arrival estimation methods applied to measurements from a digital array antenna,” in *Proceedings of the Sensor Array and Multichannel Signal Processing Workshop*. IEEE, 2000, pp. 464–468.
- [55] H. Krim and M. Viberg, “Two decades of array signal processing research: the parametric approach,” *Signal Processing Magazine*, vol. 13, no. 4, pp. 67–94, 1996.
- [56] A. J. Braga, X. Begaud, B. Huyart and V. Y. Vu, “Direction of arrival and time of arrival measurements using five-port reflectometers and quasi-Yagi antennas,” in *11th International Symposium on Antenna Technology and Applied Electromagnetics [ANTEM 2005]*. IEEE, 2005, pp. 1–4.
- [57] D. A. Ando, *Direction of Arrival estimation using Off-the-Shelf directional antennas array*, 2018. [Online]. Available: [https://lasp.unb.br/wp-content/uploads/files/research/Daniel\\_Akira\\_relatorio\\_final.pdf](https://lasp.unb.br/wp-content/uploads/files/research/Daniel_Akira_relatorio_final.pdf)

- [58] L. Meier, P. Tanskanen, L. Heng, G. H. Lee, F. Fraundorfer, and M. Pollefeys, “Pixhawk: A micro aerial vehicle design for autonomous flight using onboard computer vision,” *Autonomous Robots*, vol. 33, no. 1-2, pp. 21–39, 2012.
- [59] L. Meier, D. Honegger, and M. Pollefeys, “Px4: A node-based multithreaded open source robotics framework for deeply embedded platforms,” in *Robotics and Automation (ICRA), 2015 IEEE International Conference on*. IEEE, 2015, pp. 6235–6240.
- [60] 3DR. (2015) SOLO User Manual. [Online]. Available: [http://3dr.com/wp-content/uploads/2017/03/v9\\_02\\_25\\_16.pdf](http://3dr.com/wp-content/uploads/2017/03/v9_02_25_16.pdf)
- [61] 3DR. (2014) X8+ Operation Manual. [Online]. Available: <http://3dr.com/wp-content/uploads/2017/03/X8-Operation-Manual-vA.pdf>
- [62] 3DR. (2014) IRIS Operation Manual. [Online]. Available: <http://3dr.com/wp-content/uploads/2017/03/IRIS-Operation-Manual-v6.pdf>
- [63] AeroVironment. (2017) Quantix User Manual. [Online]. Available: <https://www.avdroneanalytics.com/Upload/MediaCenter/636675046702100584.pdf>
- [64] Autel Robotics. (2017) EVO page. [Online]. Available: <https://www.autelrobotics.com/evo/>
- [65] Autel Robotics. (2017) X-Star Premium Manual. [Online]. Available: <https://3yn7uf15sq4l1ivh8t2tfir5-wpengine.netdna-ssl.com/wp-content/uploads/2016/09/x-star-premium-manual.pdf>
- [66] Blade. (2016) Blade Conspiracy Instruction Manual. [Online]. Available: <http://www.bladehelis.com/ProdInfo/Files/BLH02000-Manual-EN.pdf>
- [67] Blade. (2017) Theory XL Instruction Manual. [Online]. Available: <http://www.bladehelis.com/ProdInfo/Files/BLH02150-Manual-EN.pdf>
- [68] Blade. (2017) Torrent 110 FPV PNP. [Online]. Available: <http://www.bladehelis.com/ProdInfo/Files/BLH04050-Manual-EN.pdf>
- [69] DJI. (2018) Mavic 2 User Manual. [Online]. Available: [https://dl.djicdn.com/downloads/Mavic\\_2/20180920/Mavic+2+Pro+Zoom+User+Manual\\_v1.2.pdf](https://dl.djicdn.com/downloads/Mavic_2/20180920/Mavic+2+Pro+Zoom+User+Manual_v1.2.pdf)
- [70] DJI. (2017) Phantom 4 User Manual. [Online]. Available: [https://dl.djicdn.com/downloads/phantom\\_4\\_pro/20171017/Phantom\\_4\\_Pro\\_Pro\\_Plus\\_User\\_Manual\\_EN.pdf](https://dl.djicdn.com/downloads/phantom_4_pro/20171017/Phantom_4_Pro_Pro_Plus_User_Manual_EN.pdf)
- [71] DJI. (2018) Matrice 2000 User Manual. [Online]. Available: [https://dl.djicdn.com/downloads/M200/20180910/Matrice\\_210\\_210\\_RTK\\_User\\_Manual\\_EN.pdf](https://dl.djicdn.com/downloads/M200/20180910/Matrice_210_210_RTK_User_Manual_EN.pdf)
- [72] EHang. (2018) GhostDrone page. [Online]. Available: <http://www.ehang.com/param.html>



- [73] EHang. (2018) Falcon page. [Online]. Available: <http://www.ehang.com/bat/>
- [74] FlyAbility. (2018) ELIOS Inspect and Explore. [Online]. Available: <https://drive.google.com/file/d/1IVuUpzUAz3RtH1HCTxbI4dAgq9H2TCyQ/view>
- [75] GoPro. Karma Let's Get Started. [Online]. Available: [https://d3rd8mpr9gp2n3.cloudfront.net/content/dam/post-purchase/karma/pdfs/Karma\\_MainSKUQSG\\_HERO5\\_Default\\_LR\\_REVA.pdf](https://d3rd8mpr9gp2n3.cloudfront.net/content/dam/post-purchase/karma/pdfs/Karma_MainSKUQSG_HERO5_Default_LR_REVA.pdf)
- [76] GoPro. (2018) Karma Tech Specs. [Online]. Available: <https://images-eu.ssl-images-amazon.com/images/I/817tGGpn0KS.pdf>
- [77] Ubsan. X4 Air User Manual. [Online]. Available: <https://www.hubsan.com/support/files/products/H501A/um/manual-en.pdf>
- [78] Ubsan. X4 Plus User Manual. [Online]. Available: <https://www.hubsan.com/support/files/products/H107P/um/manual-en.pdf>
- [79] Ubsan. X4 Pro User Manual. [Online]. Available: <https://www.hubsan.com/support/files/products/H109SS/um/manual-en.pdf>
- [80] Ideafly. (2015) Storm page. [Online]. Available: <http://www.idea-fly.com/En/parameter.asp?id=6>
- [81] Ideafly. (2015) Grasshopper page. [Online]. Available: <http://www.idea-fly.com/En/productshow.asp?id=23>
- [82] Ideafly. (2015) Poseidon page. [Online]. Available: <http://www.idea-fly.com/En/productshow.asp?id=21>
- [83] Parrot. (2018) Anafi page. [Online]. Available: <https://www.parrot.com/us/drones/anafi#technicals>
- [84] Parrot. (2018) Bebop User Guide. [Online]. Available: [https://www.parrot.com/files/s3fs-public/firmware/bebop-2\\_user-guide\\_uk\\_2\\_0.pdf](https://www.parrot.com/files/s3fs-public/firmware/bebop-2_user-guide_uk_2_0.pdf)
- [85] Parrot. (2018) Disco page. [Online]. Available: <https://www.parrot.com/us/drones/parrot-disco-fpv#technicals>
- [86] PowerVision. (2018) PowerEgg page. [Online]. Available: <https://www.powervision.me/uk/product/poweregg>
- [87] PowerVision. (2018) PowerEye page. [Online]. Available: <https://www.powervision.me/uk/product/powereye/specs>
- [88] Redcat racing. (2017) Carbon 210 Race Drone Manual. [Online]. Available: <http://www.redcatracing.com/manuals/CARBON210MANUAL.pdf>

- [89] SkyDrones. (2018) Zangão Characteristics. [Online]. Available: [https://skydrones.com.br/wp-content/uploads/2017/07/SkyDrones\\_Zangao.pdf](https://skydrones.com.br/wp-content/uploads/2017/07/SkyDrones_Zangao.pdf)
- [90] (2018) Response e-mail. [Online]. Available: [https://drive.google.com/file/d/140ScdddqtOSy45Kso1P\\_rWWv-YxfdsB-/view](https://drive.google.com/file/d/140ScdddqtOSy45Kso1P_rWWv-YxfdsB-/view)
- [91] SkyDrones. (2018) Pelicano Characteristics. [Online]. Available: [https://skydrones.com.br/wp-content/uploads/2017/08/SkyDrones\\_Pelicano.pdf](https://skydrones.com.br/wp-content/uploads/2017/08/SkyDrones_Pelicano.pdf)
- [92] SkyDrones. (2018) Strix AG Characteristics. [Online]. Available: [https://skydrones.com.br/wp-content/uploads/2017/07/SkyDrones\\_Strix-AG.pdf](https://skydrones.com.br/wp-content/uploads/2017/07/SkyDrones_Strix-AG.pdf)
- [93] Syma. (2016) X5SW User Manual. [Online]. Available: <http://www.symatoys.com/upload/201609/13/201609131500596655.pdf>
- [94] Syma. (2018) X8Pro User Manual. [Online]. Available: <http://www.symatoys.com/goodshow/x8-pro-syma-x8-pro-subvert-your-visual-enjoy-the-f.html>
- [95] Syma. (2018) Z1 User Manual. [Online]. Available: <http://www.symatoys.com/goodshow/z1-syma-z1-enjoy-the-convenience-and-intelligence.html>
- [96] Traxxas. (2018) Aton page. [Online]. Available: <https://traxxas.com/products/landing/Aton/>
- [97] Traxxas. (2018) QR-1 site. [Online]. Available: <https://traxxas.com/products/models/heli/6208qr1>
- [98] Traxxas Latrax. Latrax Alias page. [Online]. Available: <https://latrax.com/products/alias?t=specs>
- [99] UdiR/C. (2017) Discovery2 U818A page. [Online]. Available: <http://www.udirc.com/products/discovery2-u818a-plus>
- [100] UdiR/C. (2016) Peregrine U28W Guide. [Online]. Available: <http://www.udirc.com/wp-content/uploads/2016/12/U28W-guide.pdf>
- [101] UdiR/C. (2017) Predator page. [Online]. Available: <http://www.udirc.com/products/u842wifi>
- [102] Walkera. (2017) Furious 215 page. [Online]. Available: <https://www.walkera.com/index.php/Goods/canshu/id/45.html>
- [103] Walkera. (2017) Voyager page. [Online]. Available: <http://www.walkera.com/v4/#v42>
- [104] Walkera. (2017) VITUS Quick Start Guide. [Online]. Available: <https://www.walkera.com/downloads/vitus/VITUS%20Quick%20Start%20Guide-EN-V1.3.pdf>
- [105] WlToys. Q696-A page. [Online]. Available: [https://wltoys.eu/wl\\_en/catalog/product/view/id/2353/s/wltoys-q696-a/category/63](https://wltoys.eu/wl_en/catalog/product/view/id/2353/s/wltoys-q696-a/category/63)

- [106] WIToys. V383 page. [Online]. Available: [https://wltoys.eu/wl\\_en/catalog/product/view/id/2359/s/wltoys-v383/category/63](https://wltoys.eu/wl_en/catalog/product/view/id/2359/s/wltoys-v383/category/63)
- [107] WIToys. Q696-D page. [Online]. Available: [https://wltoys.eu/wl\\_en/catalog/product/view/id/2352/category/63](https://wltoys.eu/wl_en/catalog/product/view/id/2352/category/63)
- [108] Yunnec. Typhoon 4K page. [Online]. Available: <http://us.yunec.com/typhoon-4k-specs>
- [109] Yunnec. Tornado User Manual. [Online]. Available: [http://us.yunec.com/files/downloads/h920/h920\\_user\\_manual\\_A5\\_\(st12\)\\_v1.0.pdf](http://us.yunec.com/files/downloads/h920/h920_user_manual_A5_(st12)_v1.0.pdf)
- [110] Yunnec. H520 Owners Guide. [Online]. Available: [http://commercial.yunec.com/files/downloads/H520/Yunec%20H520%20Manual+Datapilot%20Operations%20Guide\\_EN.pdf](http://commercial.yunec.com/files/downloads/H520/Yunec%20H520%20Manual+Datapilot%20Operations%20Guide_EN.pdf)
- [111] M. Wax and T. Kailath, "Detection of signals by information theoretic criteria," *IEEE Transactions on Acoustics, Speech, and Signal Processing*, vol. 33, no. 2, pp. 387–392, 1985.
- [112] J. P. C. L. da Costa, *Parameter Estimation Techniques for Multi-Dimensional Array Signal Processing*. Shaker Verlag, 2010.
- [113] Z. Chen, G. Gokeda, and Y. Yu, *Introduction to Direction-of-Arrival estimation*. Artech House, 2010.
- [114] M. A. M. Marinho, F. Antreich, J. P. C. L. da Costa, and J. A. Nossek, "Reduced rank TLS array interpolation for DOA estimation," in *18th International ITG Workshop on Smart Antennas (WSA)*. VDE, 2014, pp. 1–5.
- [115] M. A. Marinho, F. Antreich, J. P. C. L. da Costa, and J. A. Nossek, "A signal adaptive array interpolation approach with reduced transformation bias for DOA estimation of highly correlated signals," in *International Conference on Acoustics, Speech and Signal Processing (ICASSP)*. IEEE, 2014, pp. 2272–2276.
- [116] A. DEVICES. (2017) AD9361 datasheet. [Online]. Available: <http://www.analog.com/media/en/technical-documentation/data-sheets/AD9361.pdf>
- [117] MATLAB, *version 8.5.0.197613 (R2015a)*. Natick, Massachusetts: The MathWorks Inc., 2015.
- [118] "Data Sheet dual band antenna, 2.4 & 5GHz, PCB." [Online]. Available: [https://www.te.com/commerce/DocumentDelivery/DDEController?Action=showdoc&DocId=Data+Sheet%7F2118309-1%7FA%7Fpdf%7FEnglish%7FENG\\_DS\\_2118309-1\\_A\\_2118309-1.pdf%7F2118309-1](https://www.te.com/commerce/DocumentDelivery/DDEController?Action=showdoc&DocId=Data+Sheet%7F2118309-1%7FA%7Fpdf%7FEnglish%7FENG_DS_2118309-1_A_2118309-1.pdf%7F2118309-1)

# Appendix A

## Proposed Extrapolation Algorithm to find the EFT thresholds for extremely low Probability of False Alarm

In this Appendix it is proposed an extrapolation algorithm to estimate the thresholds of the EFT algorithm in cases that the Probability of False Alarm ( $P_{fa}$ ) is extremely low.

Depending on the noise behavior and the parameters of the scenario [REF1, REF2], the thresholds can be extremely low. Therefore, the computational complexity of (3.16) can be prohibitive. In order to overcome such limitation, an extrapolation approach to compute the thresholds for extremely low values of  $P_{fa}$  is proposed.

Since it is desired to estimate values outside the known limits, an extrapolation method to estimate these values can be used. It is approximated the descending side of the curve as a decreasing exponential. In order to simplify the approximation, the logarithmic scale as exemplified in Fig. A.1 is applied .

Given the two known points in Fig. A.1 obtained by Monte Carlo simulations and given the linear extrapolation in (A.1), it is possible to compute the two unknown constants  $a$  and  $b$ .

$$P_{fa} = a \cdot \eta_P + b. \quad (\text{A.1})$$

The constants  $a$  and  $b$  are given by (A.2) and (A.3) by using the two known points  $(\log_{10}(P_{fa1}), \eta_1)$  and  $(\log_{10}(P_{fa2}), \eta_2)$ .

$$a = \frac{\log_{10} \left( \frac{P_{fa2}}{P_{fa1}} \right)}{(\eta_2 - \eta_1)} \quad (\text{A.2})$$

$$b = \log_{10} (P_{fa2}) - \eta_2 \cdot \left( \frac{\log_{10} \left( \frac{P_{fa2}}{P_{fa1}} \right)}{(\eta_2 - \eta_1)} \right) \quad (\text{A.3})$$

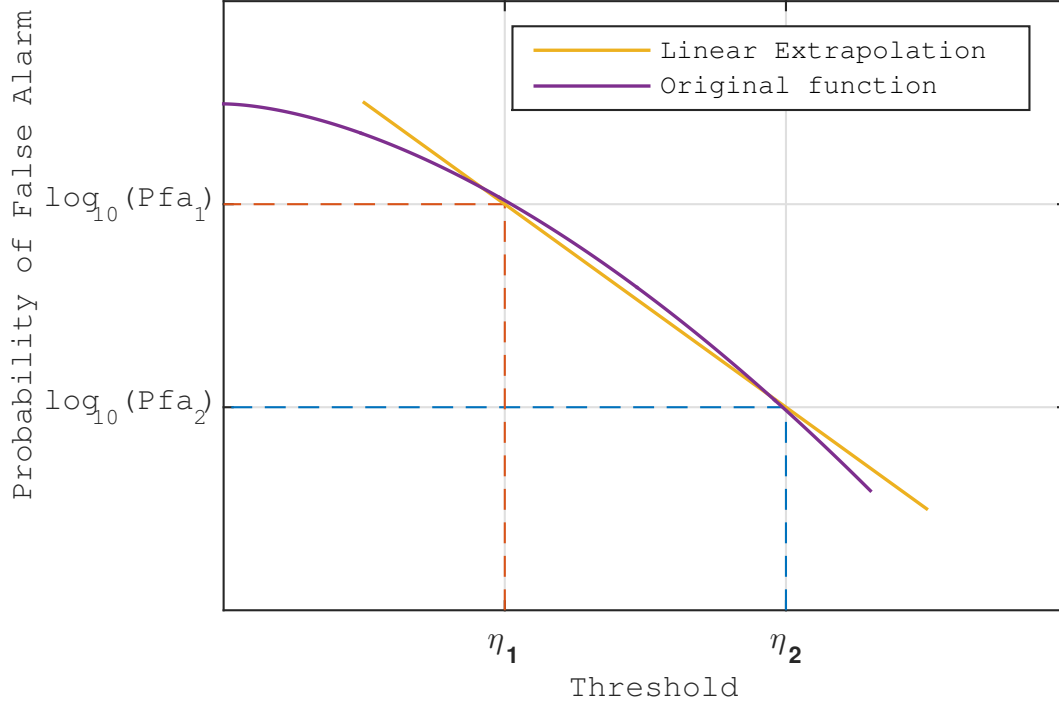


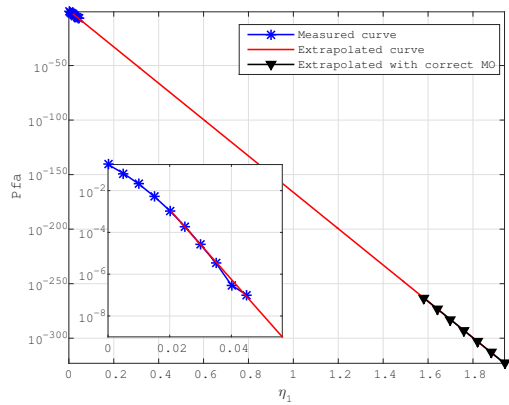
Figure A.1: Log linear extrapolation based on two points given by  $P_{fa}$ s and Thresholds  $\eta_P$ .

By replacing  $a$  and  $b$  in (A.1), it is obtained the expression for the  $\hat{\eta}_P$  in (A.4).

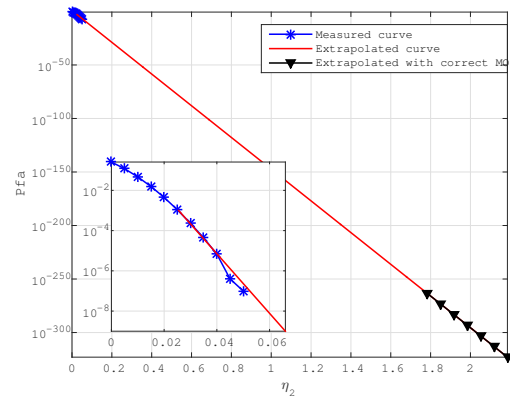
$$\hat{\eta}_P = \frac{\log_{10}(P_{fa}) - \left( \log_{10}(P_{fa2}) - \frac{\eta_2}{(\eta_2 - \eta_1)} \cdot \log_{10}\left(\frac{P_{fa2}}{P_{fa1}}\right) \right)}{\log_{10}\left(\frac{P_{fa2}}{P_{fa1}}\right)} \cdot (\eta_2 - \eta_1). \quad (\text{A.4})$$

In our Framework in Fig. 4.5, the EFT with a  $P_{fa} = 10^{-263}$  is set up. For this  $P_{fa}$ , it is obtained the following values for the thresholds  $\eta_1 = 1.5810$ ,  $\eta_2 = 1.7810$ , and  $\eta_3 = 2.1840$ .

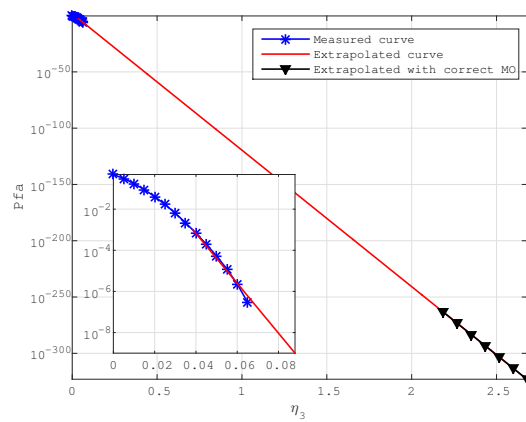
Note that there are only three thresholds, since the smallest eigenvalue is assumed as a noise eigenvalue in the EFT approach. In Figs. A.2(a), A.2(b) and A.2(c), it is depicted the extrapolation curves for the thresholds  $\eta_1$ ,  $\eta_2$  and  $\eta_3$ , respectively.



(a)



(b)



(c)

Figure A.2: Thresholds for extrapolated data using computation with  $M=4$  and  $N=41$ .

# ATTACHMENT

In the following attachment we describe configurations of the autopilot hardware controller PixHawk [58, 59]. In an easy way, it helps the new researchers to put some VANT to fly.

# ATTACHMENT A

## PixHawk Controller Setup

To perform these steps you must have installed the Mission Planner [REF5] software and connect the PixHawk controller to the computer via USB (recommended) or telemetry.

After you open the Mission Planner software and the controller is already connected to the computer, you must select the port on the computer that is used for communication in the upper right corner. The figure A.1 present this step.

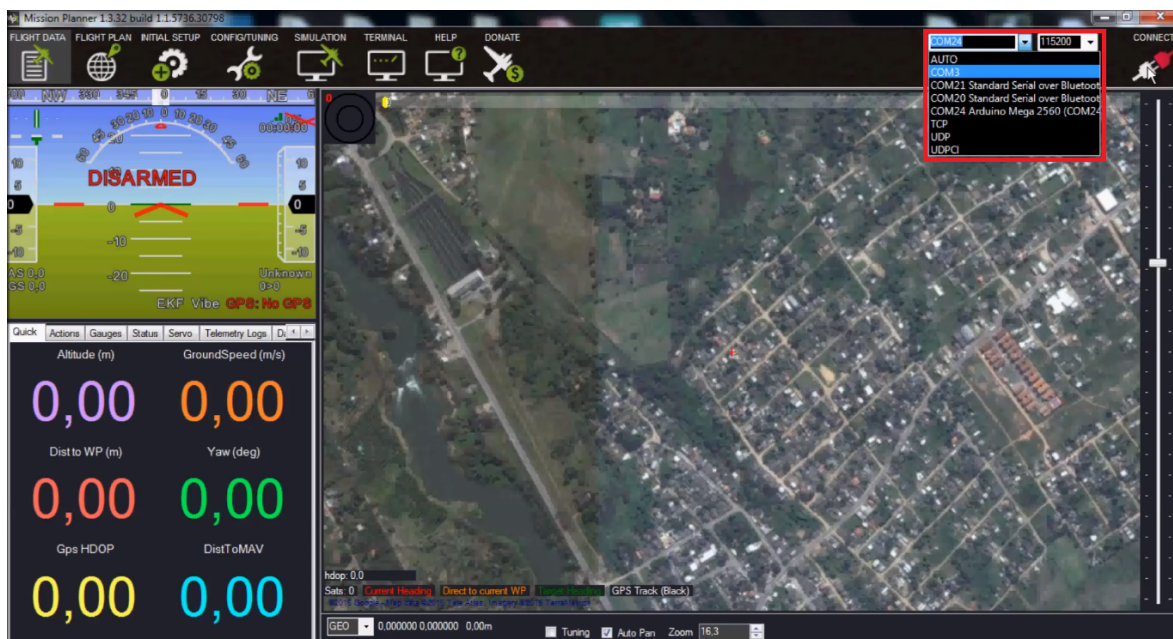


Figure A.1: Selection of the port on Mission Planner software.

Now we can use Wizard to make the initial settings, and it will guide us through the process. So, click on "Initial Setup" and then in "Wizard". The first question is about which frame layout are you using. Select your frame and click on "Next".

Note: If the VANT is connected with USB cable to the PC, take care that the cable does not swing very much and may disconnect during the processes below. Otherwise the whole process should be redone from the beginning.



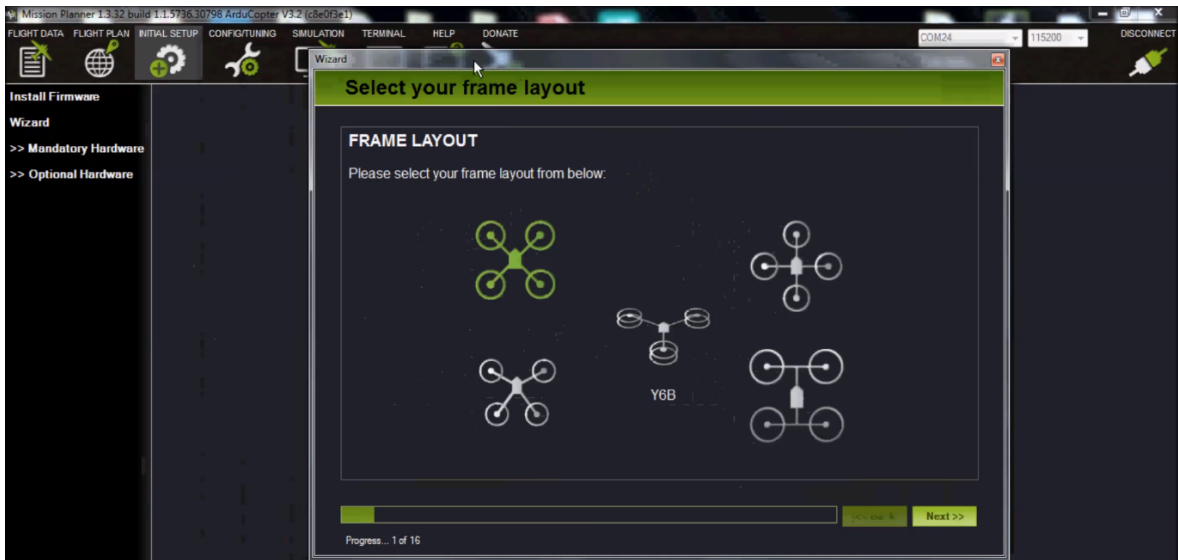


Figure A.2: Selection of the frame layout on Mission Planner software.

## A.1 Accelerometer Calibration

One of the most important step is the calibration of the accelerometer. This step allows Pixhawk to know the correct sides and how it is placed in the frame. The Figure A.3 shows this step. After placing the VANT on a selected position click on "Start" and do what the software asks for by looking out for the correct positions. Then, click in next when the process ends.

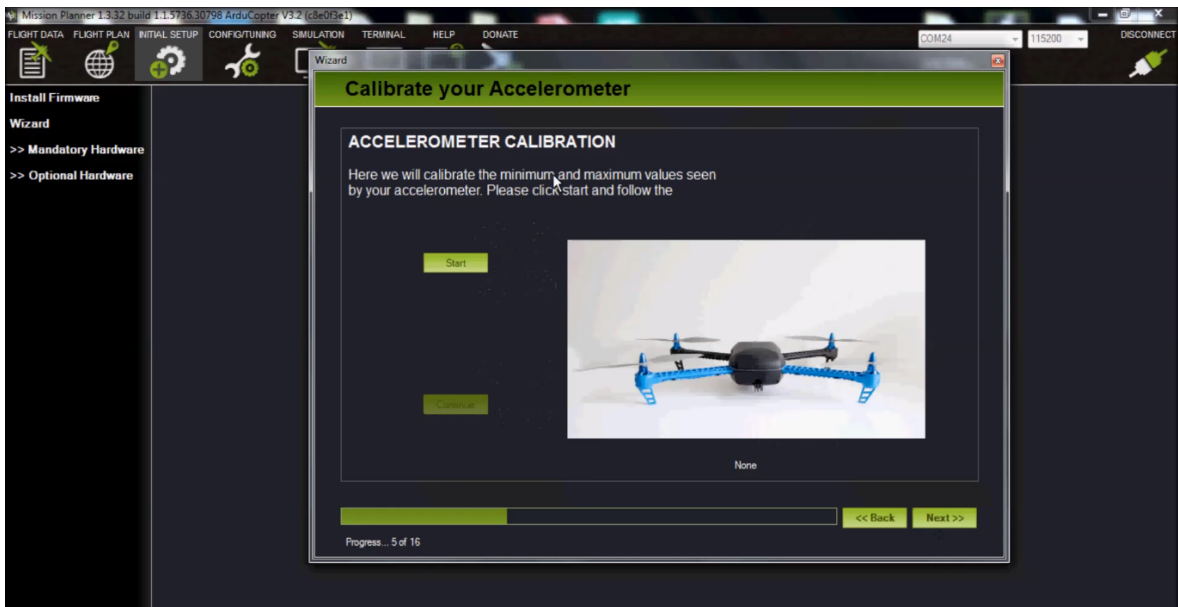


Figure A.3: Accelerometer Calibration on Mission Planner software.

## A.2 Compass Calibration

Now it is necessary to calibrate the compass, this is done on all sides similarly as shown in Section A.1, except that now we need to rotate the UAV 360° on each measured axis. To guide us in this process, the white dots of the Figure A.4 must be untouched by the red dot while the UAV is rotated around the axes. When the PixHawk acquire enough samples the process finishes automatically.

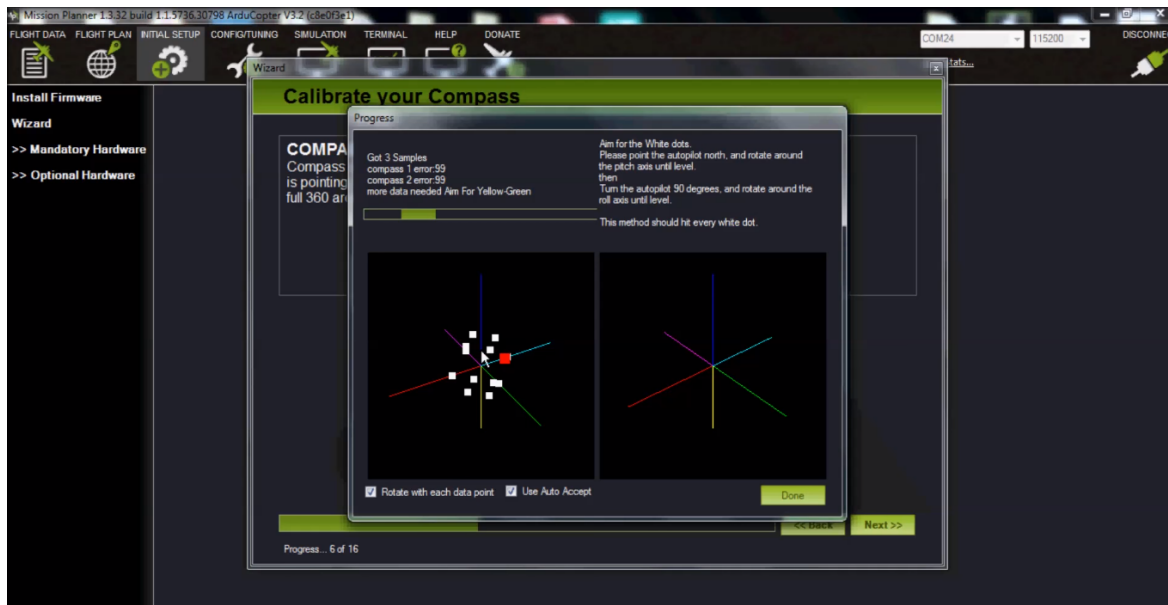


Figure A.4: Compass Calibration on Mission Planner software.

## A.3 Battery Monitor

PixHawk needs to measure the amount of charge present and delivered by the battery throughout the flight experience. This allows better control and avoid accidents due to lack of battery. Therefore, select the best option according to the hardware present in your UAV and enter the correct amount of battery capacity.

## A.4 Sonar

With the sonar, the controller can control the approach of obstacles. This is an important item to prevent collisions or uncontrolled landings from occurring. Then, check the box stating that you have a sonar installed and select which model is present in your UAV, otherwise leave the box unchecked and click on next.

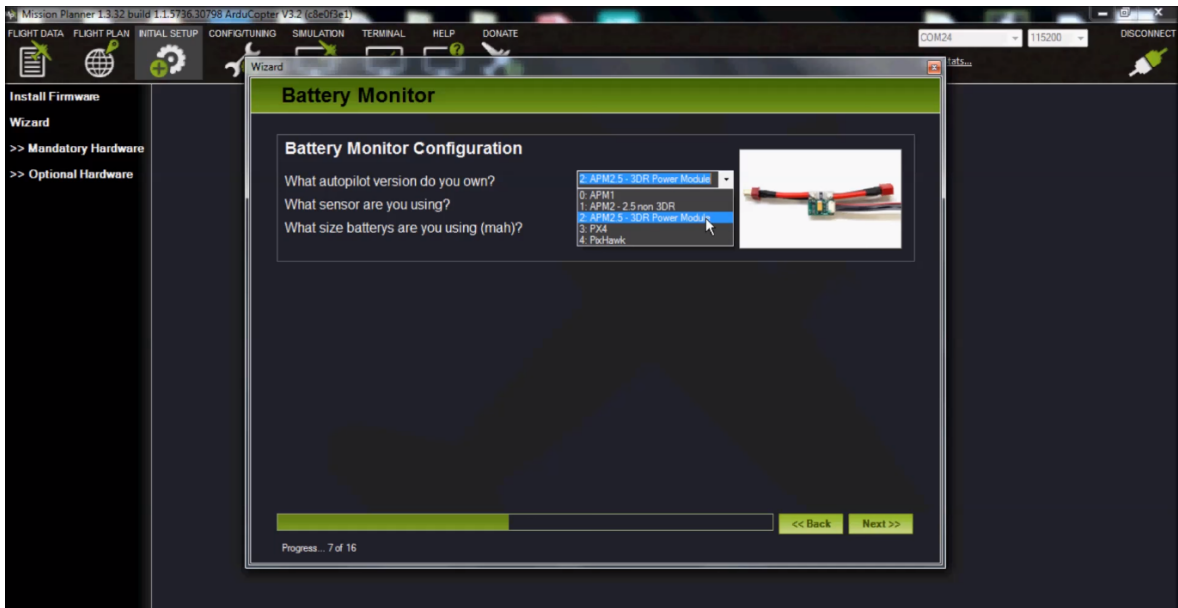


Figure A.5: Battery selection on Mission Planner software.

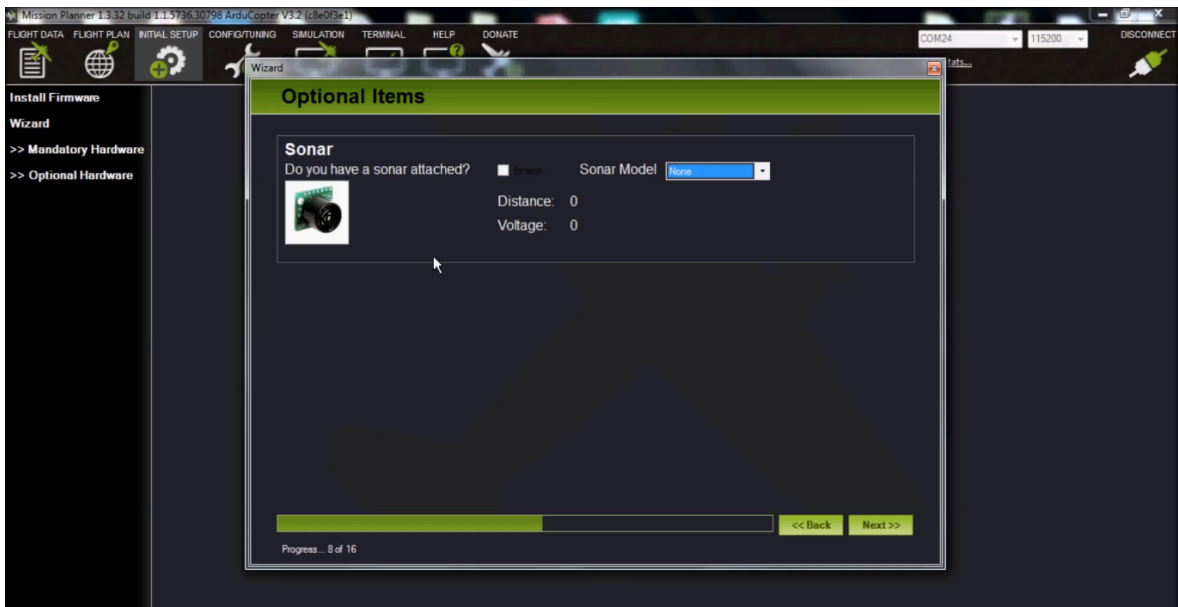


Figure A.6: Sonar selection on Mission Planner software.

## A.5 Radio Calibration

On remotely piloted flights, the commands are sent to the controller via a Radio Control (RC). This RC must to be calibrated in order to allow the controller to know what are the values of the limits of the controller. This step is very simple, and what you need to do is move all the sticks and switches to their limits so the controller can record these values. Therefore, make sure the radio is turned on and remove the propellers when you are done with this setting. Click on "Calibrate Radio" to start and, when finished, click on "Click when done". The boundaries are marked by the red bars in Figure A.7.



Figure A.7: Radio calibration on Mission Planner software.

## A.6 Fly modes

This chapter is one of the most important in this work. In addition to providing an overview of the configuration of the controller, this work aims to explain the different flight modes for when to make your first flights. Knowing which flight mode is most recommended, whether a beginning, intermediate or advanced pilot.

The Table A.1 presents the flight modes and its descriptions. This table was built with the modified informations taken from Escola de Drones [REF6] webpage.

Table A.1: Table of flight modes present on PixHawk.

<b>Flight mode</b>	<b>Description</b>
Stabilize	The stabilize mode does not have automatic altitude control or positioning (GPS), it is one of the most difficult modes, since you have to regulate the accelerator constantly, it is a very active piloting and not recommended for beginners, however, after learning to fly in modes with altitude and positioning controlled automatically it is highly recommended that you practice Stabilize mode, because in situations that the autopilot fails you must know how to safely drive your drone to the ground in manual mode.
Alt Hold	In Alt Hold mode the acceleration is controlled automatically to maintain the drone at the same altitude, it is an easy mode of piloting, considering that you will worry more about the right control, leaving the left stick in the middle the drone will hover at the current altitude detected by the inertial sensors, when you increase the acceleration the drone rises, then you return the stick to the middle and it maintains the new altitude. In this mode when you land you need to wait a few seconds to disarm, this is normal, a necessary check to prevent disarmament in the air.
Loiter	The Loiter mode is the GPS mode, the VANT will try to maintain its current position, a good GPS signal is essential for a quiet flight, if there are GPS system failures and the drone starts to move away one must quickly change to the Alt Hold or Stabilize (depending on your ability) to regain control, some people with less experience turn on failsafe, it is also an option, but if the home position was recorded with error due to lack of satellites or some problem and the drone start pulling away, you should get back in control immediately by turning off the fail safe.
Return To Launch (RTL)	The RTL mode is operated in conjunction with GPS as well (and depends on a good signal) and has the function of bringing the drone to the recorded home point, ie the takeoff position. When using this flight mode it is very important to consider the parameter "RTL_ALT", which is the height the drone will set for the return mission home, by default the parameter is set to 15M if you want the drone to return at the same height that it is currently this parameter must be set to 0.

Drift	In this mode the Roll is automatically controlled and the other controls are available to the pilot, one-handed control is possible in most of the time, the YAW is not used and you will only use the left control when you want to change altitude, it is similar to the control of a joystick.
Guided	The guided mode is like dynamic missions, instead of using a control, you command the flight via waypoints directly from the ground station (computer / tablet).
Circle	In this mode the drone will be flying in circles, the radius must be defined in the "CIRCLE_RADIUS" parameter. If the parameter is set to 0 the drone will rotate slowly on the axis itself, good for panning.
Land	Land mode is rarely used, it is used to land. For beginners it is recommended if you lose control. But in general, it does not pay to spend a key position of the radio with him.
Follow Me	The Follow Me mode makes the drone follow you, for this you must use a ground station that has GPS (can be an USB GPS or Bluetooth).
Simple and Super Simple	The Simple and Super Simple modes are combined with other flight modes, which serve to make the control always working from the pilot's point of view. The simple uses the compass and the super uses the GPS, having as reference the Home Point.
Auto	The auto mode is used when you have previously programmed a waypoint and reached the point at which you want to execute it. It is essential a good functioning GPS and inertial sensors to perform a mission, it is recommended a small flight in Loiter mode to test the drone before starting the auto mode, but you can also start the mission on the ground (accelerator at 0, configured key in "auto", go gradually accelerating, when you get in the middle the drone will start the mission).
Acro	Acro Mode, as the name suggests, is intended for stunts and should only be used by experienced pilots.

Now, with the concepts of the Table A.1, you can select six best flight modes, described in Figure A.8 which best describe your experience. When finished click "Save modes", for the controller to save the chosen settings.

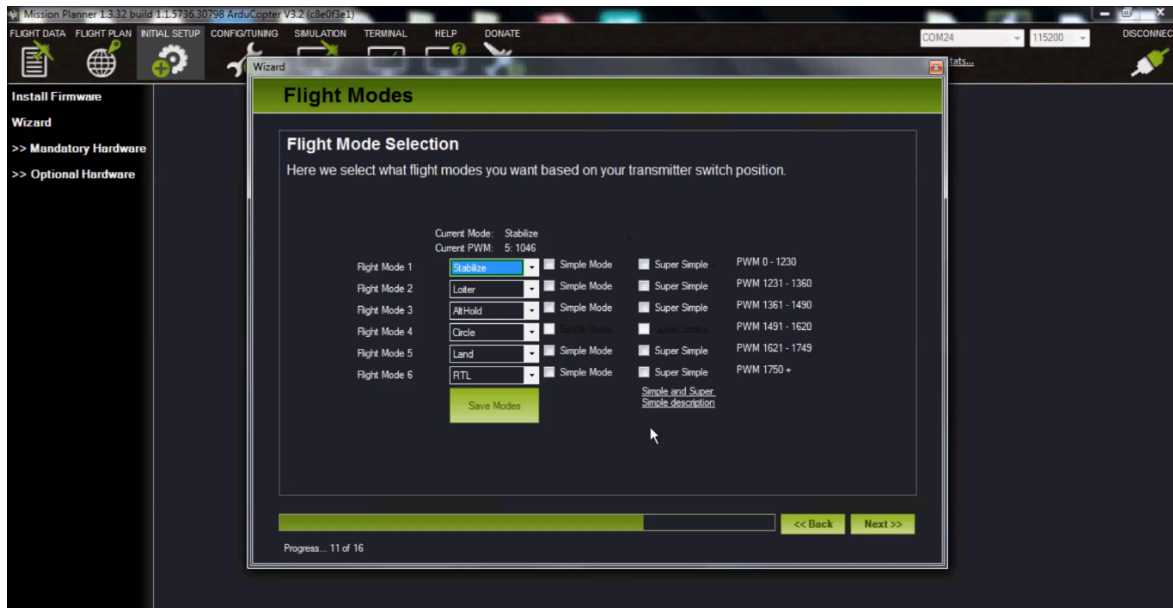


Figure A.8: Flight modes configuration on Mission Planner software.

## A.7 Failsafe

This step configures what happens when one of the three following fails is triggered.

- Battery failsafe: When the battery is finished and the VANT is still on flight.
- Ground Station failsafe: When the VANT lost the telemetry communication.
- Throttle failsafe: When the VANT lost communication with the RC.

Select the options that best describe your needs and then click on "Next"

## A.8 GeoFence Settings

This settings configures the radius, altitude and the action for Geofence, that is a virtual fence, based on home position, that the PixHawk will not fly outside of.

## A.9 Possible Errors

Now the settings of the VANT are fully completed. It is ready to fly, however it is important to know possible problems presented by the Mission Planner [REF5] at the take

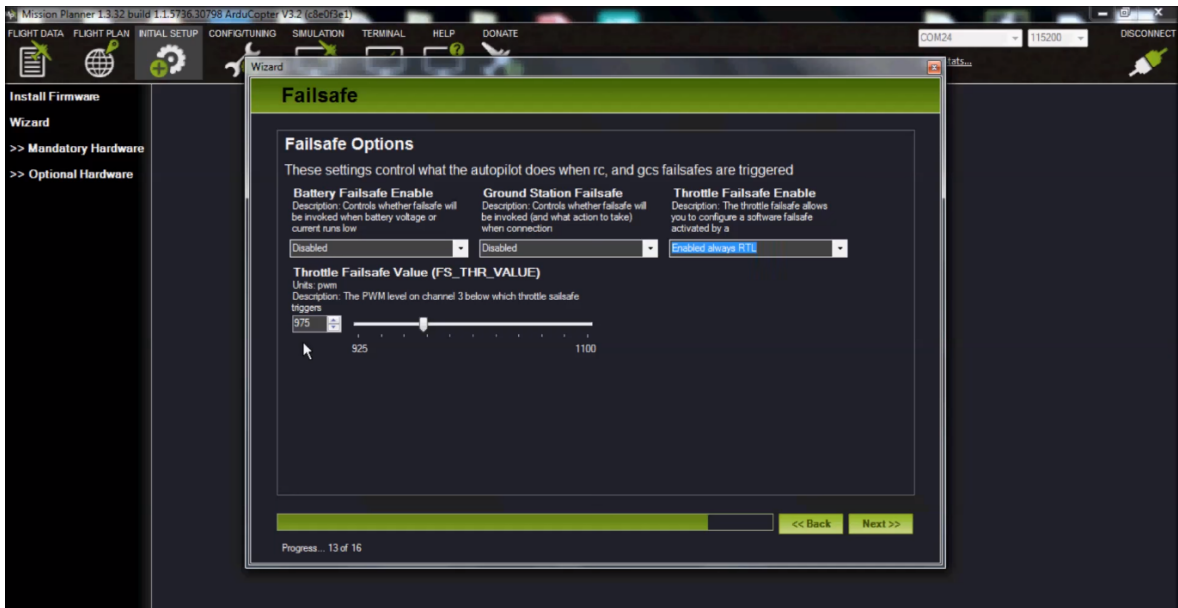


Figure A.9: Failsafe configuration on Mission Planner software.

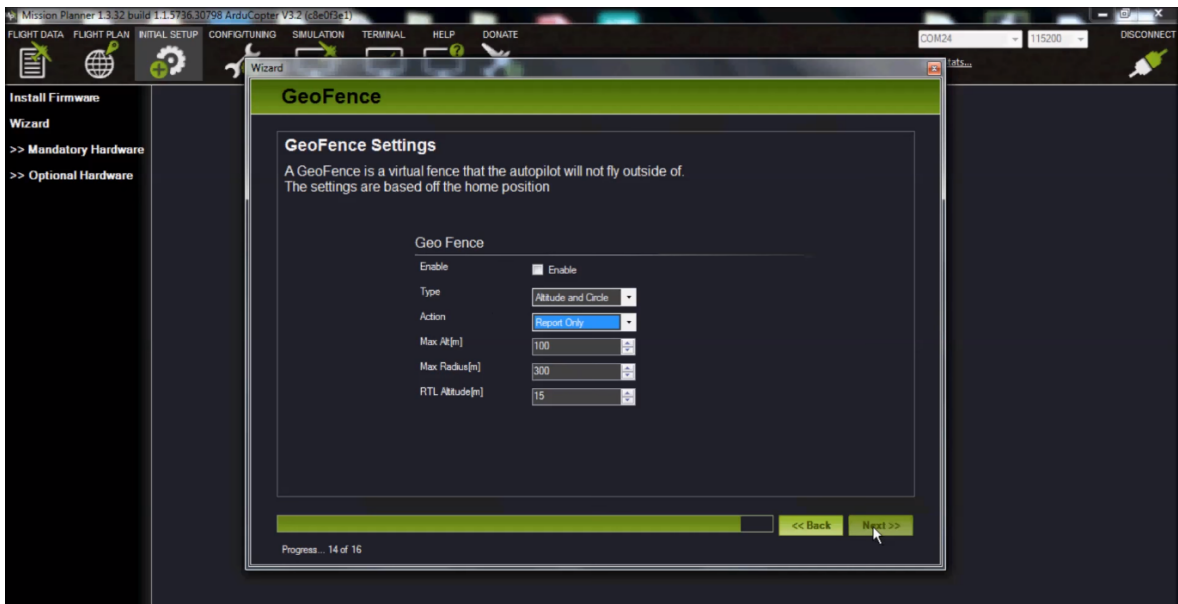


Figure A.10: GeoFence configuration on Mission Planner software.

off time. The Table A.2 presents the most common errors and was built with the modified informations taken from Ardupilot [REF7] webpage.



Table A.2: Table of most common errors displayed on Mission Planner software.

<b>Errors</b>	<b>Description</b>
RC not calibrated	The radio calibration has not been performed. RC3_MIN and RC3_MAX must have been changed from their default values (1100 and 1900), and for channels 1 to 4, MIN value must be 1300 or less, and MAX value 1700 or more.
Compass not calibrated	The compass(es) has not been calibrated. the COMPASS_OFS_X, Y, Z parameters are zero or the number or type of compasses connected has been changed since the last compass calibration was performed.
Need 3D Fix	The GPS does not have a 3D fix (four satellites) and the vehicle is in a flight mode that requires the GPS and/or the circular fence is enabled.
Bad Velocity	The vehicle's velocity (according to inertial navigation system) is above 50cm/s. Issues that could lead to this include the vehicle actually moving or being dropped, bad accelerometer calibration, GPS updating at below the expected 5hz.
High GPS HDOP	The GPS's HDOP value (a measure of the position accuracy) is above 2.0 and the vehicle is in a flight mode that requires GPS and/or the circular fence is enabled. This may be resolved by simply waiting a few minutes, moving to a location with a better view of the sky or checking sources of GPS interference (i.e. FPV equipment) are moved further from the GPS. Alternatively the check can be relaxed by increasing the GPS_HDOP_GOOD parameter to 2.2 or 2.5. Worst case, the pilot may disable the fence and take-off in a mode that does not require the GPS (i.e. Stabilize, AltHold) and switch into Loiter after arming but this is not recommended.
Alt disparity	The barometer altitude disagrees with the inertial navigation (i.e. Baro + Accelerometer) altitude estimated by more than 2 meters. This message is normally short-lived and can occur when the flight controller is first plugged in or if it receives a hard jolt (i.e. dropped suddenly). If it does not clear, the accelerometers may need to be calibrated or there may be a barometer hardware issue.

# References

- [REF1] J. P. C. L. da Costa, *Parameter Estimation Techniques for Multi-Dimensional Array Signal Processing*. Shaker Verlag, 2010.
- [REF2] J. P. C. L. da Costa, F. Roemer, M. Haardt, and R. T. de Sousa, “Multi-dimensional model order selection,” *EURASIP Journal on Advances in Signal Processing*, vol. 2011, no. 1, p. 26, 2011.
- [REF3] L. Meier, P. Tanskanen, L. Heng, G. H. Lee, F. Fraundorfer, and M. Pollefeys, “Pixhawk: A micro aerial vehicle design for autonomous flight using onboard computer vision,” *Autonomous Robots*, vol. 33, no. 1-2, pp. 21–39, 2012.
- [REF4] L. Meier, D. Honegger, and M. Pollefeys, “Px4: A node-based multithreaded open source robotics framework for deeply embedded platforms,” in *Robotics and Automation (ICRA), 2015 IEEE International Conference on*. IEEE, 2015, pp. 6235–6240.
- [REF5] Ardupilot. (2016) Software Mission Planner. [Online]. Available: <http://ardupilot.org/planner/>
- [REF6] Escola de Drones. (2015) MODOS DE VOO APM E PIXHAWK. [Online]. Available: <http://www.escoladedrones.com.br/modos-de-voos-apm-e-pixhawk/>
- [REF7] Ardupilot. (2016) Failure messages. [Online]. Available: [http://ardupilot.org/copter/docs/prearm\\_safety\\_check.html#failure-messages](http://ardupilot.org/copter/docs/prearm_safety_check.html#failure-messages)